Modeling 3D radiative-transfer on earth-like (exo)planets with Phoenix 3DRT and PUMA

Dissertation

zur Erlangung des Doktorgrades

des Department Physik

der Universität Hamburg

vorgelegt von

Alexander Clausius

aus Herdecke

Hamburg

2023

Contents

Contents

List of Figures

List of Tables

Zusammenfassung

Die vorliegende Arbeit ist aus der Intention entstanden, die Möglichkeiten des Strahlungstransport-Frameworks `PHOENIX 3DRT` auf die Spektrumssynthese extrasolarer Planeten anzuwenden. Wie fast immer im Kontext astronomischer Untersuchungen ist Licht der dominierende Informationslieferant und insofern ist es naheliegend, die Fingerabdrücke der Atmosphären von Planeten im Spektrum ihrer Wirtssterne zu untersuchen.

Während der Entwicklung der Arbeit hat sich jedoch ebenfalls gezeigt, dass die reine Strahlungstransport-Theorie, wie sie seit langer Zeit bei der Untersuchung von Sternatmosphären Anwendung findet, bei der Untersuchung von Exoplaneten an ihre Grenzen stößt. Hydrodynamische Prozesse in den Atmosphären, die bei der Spektrumssynthese von Sternen häufig als nachgelagerter Einflussfaktor ignoriert oder eingeschränkt behandelt werden, können im Zusammenhang mit der Modellierung von Planeten-Spektren nicht ausgeklammert werden. Dies ist nicht verwunderlich, da die Spektren vor allem thermodynamische Eigenschaften wiedergeben, die in den Atmosphären der Planeten in großem Maße von hydrodynamischen Prozessen bestimmt werden. Diese Tatsache ist lange bekannt und gut verstanden: Sie sind die Grundlage aller meteorologischer Modelle und kein Wetterbericht würde ohne ihre detaillierte Berücksichtigung sinnvolle Voraussagen treffen können.

In diesem Sinne versteht der Autor diese Arbeit vor allem als eine Brücke zwischen den zwei Disziplinen Astrophysik und Meteorologie und entsprechend liegt das Hauptaugenmerk darauf, die zugrundeliegenden theoretischen Grundlagen zu harmonisieren und miteinander kompatibel zu machen, sodass ein kombiniertes numerisches Modell entsteht, das beide Welten verbindet.

Im Ergebnis dieser Arbeit wird ein kombiniertes Modell aus 3D-Strahlungstransport und hydrodynamischem Atmosphärenberechnungen präsentiert. Beide Modelle werden auf ihre theoretischen Grundlagen hin untersucht um festzustellen, welche impliziten Annahmen in den jeweiligen Modellen enthalten sind und welche Beschränkungen in Bezug auf ihre Allgemeingültigkeit sich hieraus ergeben.

Da das Atmosphärenmodell bereits über einen sehr einfachen Strahlungstransport-Mechanismus verfügt wird dieser Teil durch den sehr viel mächtigeren Strahlungstransport aus dem `PHOENIX 3DRT`-Modell ersetzt. Um den Umfang der Arbeit zu begrenzen und den Fokus auf die grundsätzliche Frage der Kombinierbarkeit beider Modelle zu legen, werden die Berechnungen iterativ durchgeführt und die jeweiligen Ergebnisse manuell zwischen beiden Modellen ausgetauscht.

Es kann dabei am Beispiel von Mars gezeigt werden, dass die Kombination beider Modelle die be-

obachtbaren Eigenschaften wie atmosphärische Temperaturverteilungen in Anbetracht der beschriebenen Limitierungen des Atmosphärenmodells mit einer erstaunlichen Genauigkeit reproduzieren kann.

Abstract

The present work arose from the intention to apply the possibilities of the radiative transfer framework `PHOENIX 3DRT` to the spectrum synthesis of extrasolar planets. As almost always in the context of astronomical investigations, light is the dominant source of information and in this respect it makes sense to examine the fingerprints of the atmospheres of planets in the spectrum of their host stars.

During the development of the work, however, it has also become apparent that the pure radiative transfer theory, which has long been used in the study of stellar atmospheres, reaches its limits when studying exoplanets. Hydrodynamic processes in the atmosphere, which are often ignored or limited as a downstream influencing factor in the spectrum synthesis of stars, cannot be excluded in connection with the modeling of planetary spectra. This is not surprising since the spectra primarily reflect thermodynamic properties that are largely determined by hydrodynamic processes in the planetary atmospheres. This fact has long been known and well understood: they are the basis of all meteorological models and no weather report would be able to make meaningful predictions without taking them into account in detail.

In this sense, the author sees this work primarily as a bridge between the two disciplines of astrophysics and meteorology, and accordingly the main focus is on harmonizing the underlying theoretical principles and making them compatible with each other, so that a combined numerical model is created that connects both worlds .

As a result of this work, a combined model of 3D radiative transport and hydrodynamic atmospheric calculations is presented. Both models are examined for their theoretical foundations in order to determine which implicit assumptions are contained in the respective models and which limitations arise in relation to their general validity.

Since the atmosphere model already has a very simple radiative transport mechanism, this part is replaced by the much more powerful radiative transport from the `PHOENIX 3DRT`-model. In order to limit the scope of the work and to focus on the fundamental question of whether both models can be combined, the calculations are carried out iteratively and the respective results are exchanged manually between the two models.

Using the example of Mars, it can be shown that the combination of both models can reproduce the observable properties such as atmospheric temperature distributions with astonishing accuracy in view of the described limitations of the atmospheric model.

1. Introduction

"If we knew what it was we were doing,
it wouldn't be called 'research', would it..?"
— ALBERT EINSTEIN

In the last few decades, the technological progress of modern astronomical observation facilities has enabled us to investigate issues that seemed to be completely out of reach just a few years ago. In the context of space-based observation missions such as the Hubble Space Telescope (HST), the Kepler space observatory or James Webb Space Telescope (JWST), launched in December 2021, as well as ground-based telescopes with primary mirrors' diameters of or even beyond the magical number of ten meters as for instance the Keck I/II observatories or the European Extremely Large Telescope (E-ELT), currently at the construction stage, already have changed our own idea of the cosmos forever. For the first time in history, we have the possibility to not only study the bright shining stars which have attracted peoples attention since ancient times but also their companions in other solar systems, so-called exoplanets, revealing new planetary configurations, completely different from everything we knew so far but also—and thus not less exciting—planets which might be similar to our Earth in may aspects. Though people all over the world have been fascinated by stars ever since, recent astrophysical publications have attracted public attention in much larger degrees. This is not surprising: although the analysis of extrasolar planetary systems has an extraordinary meaning for the understanding of star-planet-formation mechanisms as well as other astrophysically relevant issues, the current discourse on exoplanets is not just another field of research to be examined, it concerns the basic question of our own role in universe. Hence, the relatively young field of exoplanet research has developed very rapidly during the last few decades and led to a number of 5250 exoplanet candidates (effective: February 20, 2023) (Brennan, 2022).

In the early days, the discovery of exoplanets was limited to so called *hot Jupiters*, planets whose mass equal or exceed the mass of Jupiter orbiting between approximately $0.015\,\text{AU}$[1] and $0.5\,\text{AU}$. Those close-in planets have a much greater chance of transiting their star as seen from a further outlying point than planets of the same mass in larger orbits. The most notable of these are HD209458b, the first transiting hot Jupiter found (Fortney et al., 2005), HD189733b, first mapped in 2007 by the Spitzer Space Telescope (Grillmair et al., 2007), as well as HAT-P-7b which was recently observed by the Kepler mission (Pál et al., 2008). Later, planets with masses below the solar system's gas gi-

---

[1]One *astronomical unit* (AU) is defined as the mean distance between Earth and sun, $1\,\text{AU} \approx 149.6 \times 10^6\,\text{km}$

ants could be detected which are referred to as *super-Earths*. The first super-Earths were discovered around the pulsar PSR B1257+12 in 1992 (Wolszczan and Frail, 1992). Since the two outer planets of the system have masses approximately four times of Earth, they are too small to be gas giants. The first super-Earth around a main sequence star was discovered in 2005. It orbits Gliese 876 and received the designation Gliese 876 d (two Jupiter-sized gas giants had previously been discovered in that system). It has an estimated mass of $7.5\,M_\oplus{}^2$ and a very short orbital period of just about two days. Due to the proximity of Gliese 876 d to its host star (a red dwarf), it may have a surface temperature of $430\,K - 650\,K$ and may support liquid water (Marcy et al., 2008). On December 21, 2011 a new study, published in Nature, reported the detection of two Earth-sized planets, Kepler-20 e and Kepler-20 f, orbiting the Sun-like star Kepler-20, bringing us closer to the ultimate goal – the discovery of a true Earth analogue suitable for life (Fressin et al., 2011).

Nearly all information we can gather about exoplanets is transported by radiation and encoded in the planets transmission and reflectance spectra, respectively. While passing through a planetary atmosphere, the individual atmospheric properties such as temperature, density or chemical composition are imprinted on the radiation and thus, all of the planet's properties are right there, packaged in the observed spectra. So why do we need computer models of radiative transfer processes in planetary atmospheres? Because of the complexity of the physical processes that finally led to the spectral composition we can observe it is not possible to simply "decode" the information packed in the spectra. This means that the spectrum can be thought of as some kind of fingerprint of the planet's atmosphere. Just like fingerprints, this correlation describes a mapping from a mathematical point of view, correlating each point of our parameter space of atmospheres to a spectrum that is unique but again, as well as fingerprints, the corresponding mapping cannot be inverted in terms of reading the atmospheric properties out of it's fingerprint easily. Hence, if we want to learn about planetary atmospheres we need a way to create synthetic, computer generated fingerprints that may be compared to observations. But even if we do not have observed spectra of adequate quality right now, the analysis of synthetic spectra can help us in many other scientific applications like design of future observational instruments: only if we know about the important spectral features that should be observable we can optimize our instrumental designs accordingly. Using the state-of-the-art radiative transfer code `PHOENIX` a first one-dimensional planetary atmosphere model approach was performed by M. Wagner in her PhD-thesis (Wagner, 2011). While one-dimensional spherical symmetrical models may act as a good approximation for a wide range of stellar models, the corresponding planetary atmospheric models are much more limited in various aspects of their applications: because of the symmetry breaking due to the direction of incident irradiation we need to model these problems using full three-dimensional radiative transfer theory to achieve more realistic results. Therefore, the `PHOENIX` three-dimensional radiative transfer framework (`PHOENIX 3DRT`) has been used for the radiative transfer calculations throughout this thesis, extended by a generic *bidirectional reflectance distribution function* (BRDF) model which may easily be adjusted to a wide range of surface textures and accounts for the important

---

[2]Quantities index by $\oplus$ refer to Earth properties.

reflection at the solid surface due to the optically thin atmospheres in earth-like exoplanets.

Moreover, planetary models cannot give realistic spectra as long as only radiative transfer through the atmosphere is considered: The incident irradiation drives the atmospheric dynamics that transport energy all around the planet and thus, are responsible for the temperature structure of the atmosphere to a high degree which affects the radiative transfer in return. Hence, radiative transfer and atmospheric dynamics are coupled, which is routine business in all kinds of climate and meteorological forecast models but thereby primarily specialized to earth conditions, of course. As a consequence, the *Portable University Model of the Atmosphere* (PUMA) as a highly flexible general circulation model has been coupled to the PHOENIX 3DRT model to consider the atmospheric dynamics feedback on the radiative transfer and vice versa. Therefore, a closed model framework at the border between astrophysics and meteorology has been created for the purpose of this thesis extending the degree of realism with respect to exoplanet modeling far beyond simple radiative transfer models.

First, this thesis gives a short introduction into the radiative transfer theory (ch. 2). The chapter is intended to describe the basic theory of radiative transfer as the basis for the PHOENIX modeling code this thesis uses for radiative transfer calculations. The description of the theoretical connections is substantial for the understanding of what can be achieved in terms of modeling reflection and transmission spectra, how to consider reflection at the planetary surface in earth-like planetary atmospheres and where to expect limitations. On the other hand, it is neither feasible nor sensible to describe all the theory at full length in the context of a PhD thesis as there are enough books on the subject out there and this would definitely go beyond the scope of this thesis. Thus the presentation of the theoretical background in this thesis does neither claim completeness nor strict formal correctness for itself but just intends to compile the parts of the theory important for the understanding of the further thesis as well as for reference purposes with respect to nomenclature issues.

In chapter 3, the details of the surface reflection model are presented including details on the implementation as well as model tests for various surface textures. Since the implementation of the reflection model represents one of the main tasks in order to model exoplanet atmospheres, both the theoretical derivation as well as the actual implementation are described in detail.

The basic theoretical introduction is continued in chapter 4 which deals with the fundamental concepts of climate dynamics simulations and the methods used to solve corresponding modeling setups. The governing equations describing the physical principles in the context of fluid dynamics are the Navier-Stokes equations. As these equations are badly suited for numerical modeling methods (Adcroft et al., 2004), they are transformed into the so-called *primitive equations*, classically used in nearly all modeling frameworks on climate dynamics as in the PUMA code (Lunkeit et al., 2011). This derivation induces some assumptions on the model setup and thus, the primitive equations are less general with respect to the atmospheric conditions. The limitations in the flexibility of the modeling code, given by these adaptions of the Navier-Stokes equations are discussed and followed by a description of the PUMA code used for atmospheric dynamics modeling throughout this thesis.

In chapter 5, the capabilities of the developed model are tested using the example of Mars as a well-known planet with lots of measured data to act as reference for the model results. Mars is well-suited

for testing the developed model, as it is not only our direct neighbor but also the most earth-like planet in the solar system, except for our own earth of course but nevertheless shows many specifics which are quite different from Earth conditions.

Finally, conclusions are summarized in chapter 6. The chapter is finished with a short outlook on the future works as well as potential improvements of the developed model.

2. Radiative Transfer Theory

This chapter deals with the basic concepts of radiative transfer that are described in detail e.g. in the book on stellar atmospheres by Hubeny and Mihalas (2014) or in the lecture notes on radiative transfer in stellar atmospheres by Rutten (2003). The theory of modeling radiative transfer in three-dimensional setups can be found in the *3D radiative transfer framework* by P. H. Hauschildt and E. Baron e.g. Hauschildt and Baron (2006, 2007, 2008, 2009a,b) as well as Hauschildt and Baron (2011); Jack et al. (2012); Baron et al. (2012); Hauschildt and Baron (2014) and Hauschildt and Baron (2021). If not denoted otherwise the further description of the theoretical background is guided by the aforementioned resources.

This chapter is organized as follows: A primer for radiative transfer is given in chapter 2 which includes some very basic definitions for reference and nomenclature issues (2.1), followed by some basic radiative transfer theory to compile the theoretical tools that are needed for the further discussion (2.2) and continued with a short presentation of the numerical method used to solve the classical model atmospheres' problem (2.3). The section ends with a paragraph on the 3D radiative transfer module `PHOENIX 3DRT` that is used for model calculation throughout this thesis (2.4).

2.1 Basic Definitions

The basic quantity that is used to describe radiative transfer processes is the *specific intensity I_ν* which is defined as the amount of energy $\mathrm{d}E$ in the frequency interval $[\nu, \nu + \mathrm{d}\nu]$ passing a surface element of cross-section $\mathrm{d}\sigma$ which is orientated in the direction $\boldsymbol{n}$ in the time $\mathrm{d}t$ in the direction $\boldsymbol{r}$ into the solid angle $\mathrm{d}\Omega$. If we define θ to be the angle between the orientation of the surface element $\mathrm{d}\sigma$ the radiation passes through and the direction $\boldsymbol{r}$ of the radiation itself $\theta \equiv \angle(\boldsymbol{r}, \boldsymbol{n})$, we get the following defining equation of the specific intensity

$$\mathrm{d}E = I_\nu(\boldsymbol{r})\cos(\theta)\,\mathrm{d}\nu\,\mathrm{d}\sigma\,\mathrm{d}t\,\mathrm{d}\Omega \tag{2.1}$$

which results in the dimension of the specific Intensity to be in the CGS-System of Units[1]

$$[I_\nu] = \mathrm{ergs\,cm}^{-2}\,\mathrm{s}^{-1}\,\mathrm{Hz}^{-1}\,\mathrm{sr}^{-1}. \tag{2.2}$$

---

[1]It is convention to describe radiative transfer processes in the CGS-System of Units and as this thesis has been developed from this field of research this convention is preserved throughout the whole thesis even though is is more common to use SI units in meteorology.

For most applications it is more sensible to consider the *mean intensity* J_ν as the specific intensity's average over all solid angles as well as the flux $\mathscr{F}_\nu$ as the net rate of energy flow across a unit area in the atmosphere

$$
\begin{aligned}
J_\nu(\boldsymbol{r}) &= \tfrac{1}{4\pi} \oint_{4\pi} I_\nu(\boldsymbol{r}, \Omega) \, \mathrm{d}\Omega \\
&= \tfrac{1}{4\pi} \int_0^{2\pi} \mathrm{d}\varphi \int_{-1}^1 I_\nu(\boldsymbol{r}, \mu, \varphi) \, \mathrm{d}\mu,
\end{aligned}
\tag{2.3}
$$

where μ has been defined to be $\mu \equiv \cos\theta$. The mean intensity J is the averaged intensity over all solid angles and used if the overall amount of photons is of interest, irrespective of the photon origin e.g., when excitation and ionization rates have to be considered.

To calculate the net rate of energy flow $\mathscr{F}_\nu$ at a given point $\boldsymbol{r}$ we have to integrate the specific intensity $\boldsymbol{I}_\nu(\boldsymbol{r}) \equiv I_\nu(\boldsymbol{r}, \boldsymbol{n}) \cdot \hat{\boldsymbol{n}}$ over all solid angles

$$
\begin{aligned}
\mathscr{F}_\nu &= \oint_{4\pi} \boldsymbol{I}_\nu(\boldsymbol{r}) \, \mathrm{d}\Omega \\
&= \int_0^{2\pi} \mathrm{d}\varphi \int_{-1}^1 I_\nu(\boldsymbol{r}, \mu, \varphi) \mu \, \mathrm{d}\mu.
\end{aligned}
\tag{2.4}
$$

This quantity describes the energetics of radiation transfer when passing through a stellar or planetary atmosphere.

2.2 Radiative Transfer Equation

While passing along a characteristic[2] through the atmosphere, the radiation's intensity may be increased or decreased due to various processes which shall phenomenologically be divided into two categories, according to whether there is a prominent coupling between the radiation energy and the thermal energy of the atoms and molecules constituting the atmosphere or the radiation can penetrate the atmosphere without significant interaction. This distinction is important, because if we want to probe the properties of the atmospheric matter such as temperature, pressure etc. by virtue of the received radiation, we have to possess profound knowledge of the coupling conditions that imprint the properties of the atmospheric matter on the radiation field.

Scattering denotes all the processes without strong coupling between radiative energy and atmospheric thermal energy pool, e.g. bound-bound transitions, where a photon interacts with an

---

[2] A characteristic is the path on which an undisturbed photon would travel and is basically represented by a straight line in the absence of relativistic effects. More precisely, it is the mathematical description of the geodesic, a photon, characterized by some specific momentum, moves along.

atom and excites a bound electron from a lower energy level a to a higher energy level b, directly followed by a deexcitation of the electron, returning the excitation energy to the radiation field by emitting a photon of the same (or slightly different) frequency. The specific intensity along a characteristic is altered by scattering processes because they may change the photon's frequency $\mathcal{S} : \nu \to \nu'$, so that the photon contributes to the specific intensity $I_{\nu'}$ rather than to I_ν or/and the photon's direction $\mathcal{S} : \boldsymbol{n} \to \boldsymbol{n}'$, so that a photon may be scattered into or out of the characteristic. These processes may mathematically be described by the so-called *redistribution function* $R = R(\nu, \boldsymbol{n}, \nu', \boldsymbol{n}')$, that gives the probability density of a photon with frequency ν along a characteristic in the direction $\boldsymbol{n}$ to be converted into a photon with frequency ν', traveling along a characteristic in the direction $\boldsymbol{n}'$. As this probability distribution must apparently be normalized, the integral over all initial and final frequencies as well as over all initial and final characteristic's orientations equals one

$$\left(\tfrac{1}{4\pi}\right)^2 \oint_{4\pi} \mathrm{d}\Omega \oint_{4\pi} \mathrm{d}\Omega' \int_0^\infty \mathrm{d}\nu \int_0^\infty \mathrm{d}\nu'\, R(\nu, \boldsymbol{n} \,;\, \nu', \boldsymbol{n}') = 1. \tag{2.5}$$

The redistribution function may be used to define scattering $\varphi(\nu)$ and emission profiles $\psi(\nu')$, describing the probability density of a photon in the frequency domain $[\nu, \nu + \mathrm{d}\nu]$ actually to be scattered without contributing to the specific intensity $\boldsymbol{I}_\nu$ along the characteristic under consideration any longer and of a photon in the frequency domain $[\nu', \nu' + \mathrm{d}\nu]$ and/or characteristic $\boldsymbol{n}$ to be scattered so that it now contributes to $\boldsymbol{I}_\nu$ respectively.

$$\varphi(\nu)\, \mathrm{d}\nu = \left(\tfrac{1}{4\pi}\right)^2 \mathrm{d}\nu \oint_{4\pi} \oint_{4\pi} \int_0^\infty R(\nu, \boldsymbol{n} \,;\, \nu', \boldsymbol{n}')\, \mathrm{d}\nu'\, \mathrm{d}\Omega\, \mathrm{d}\Omega' \tag{2.6}$$

$$\psi(\nu')\, \mathrm{d}\nu' = \left(\tfrac{1}{4\pi}\right)^2 \mathrm{d}\nu' \oint_{4\pi} \oint_{4\pi} \int_0^\infty R(\nu, \boldsymbol{n} \,;\, \nu', \boldsymbol{n}')\, \mathrm{d}\nu\, \mathrm{d}\Omega\, \mathrm{d}\Omega' \tag{2.7}$$

Again, both the scattering and emission profiles are normalized as the redistribution function is normalized itself

$$\int_0^\infty \varphi(\nu)\, \mathrm{d}\nu = \int_0^\infty \psi(\nu')\, \mathrm{d}\nu' = 1. \tag{2.8}$$

True Absorption/Emission characterizes processes where strong coupling between radiation field and thermal energy pool is evident, e.g. photo-ionization processes (bound-free absorption) where the photon's energy is (at least) partly converted into kinetic energy of the ionized electron and, as such, adds to the thermal energy of the atmospheric matter or the emission of bremsstrahlung by an electron, moving in the field of an ion where thermal energy is payed

over to the radiation field. All these processes are characterized by an energy transfer between radiation field and thermal energy pool of the atmosphere under consideration. This energy transfer imprints the physical characteristics of the atmosphere such as temperature, pressure or density at the location of interaction on the radiation field, which enables us to probe the atmospheric properties by virtue of the emitted radiation.

Keeping the aforementioned in mind, the change in intensity of a radiation beam penetrating a volume element of density ρ along the geometrical depth z can be written as

$$\frac{\mu}{\rho} \frac{\mathrm{d}I_\nu}{\mathrm{d}z} = j_\nu - k_\nu I_\nu \tag{2.9}$$

where the specific total extinction k_ν and emission coefficient j_ν have been defined. Both the absorption and extinction coefficient are composed of a scattering and a true emission/absorption part reflecting the aforementioned processes. Thus, the total extinction coefficient k_ν represents the processes decreasing the specific intensity along the characteristic under consideration while the emission coefficient j_ν accordingly describes the processes leading to an increase. If we furthermore define the *optical depth* τ to be the geometrical depth, weighted by the matter's absorption capacity along the way

$$\mathrm{d}\tau_\nu \equiv -\rho k_\nu \, \mathrm{d}z \tag{2.10}$$

as well as the so-called *source function S* as the ratio the volume element's emission and absorption characteristics

$$S_\nu \equiv \frac{j_\nu}{k_\nu} \tag{2.11}$$

equation 2.9 can be simplified to the well-known radiative transfer equation

$$\mu \frac{\mathrm{d}I_\nu}{\mathrm{d}\tau_\nu} = I_\nu - S_\nu. \tag{2.12}$$

From a mathematical point of view, the radiative transfer equation is an inhomogeneous linear differential equation of first order with the formal solution

$$I_\nu(\tau, \mu) = \frac{1}{\mu} \int_\tau^\infty S_\nu(t) e^{-(t-\tau)/\mu} \, \mathrm{d}t, \qquad (0 \leq \mu \leq 1) \tag{2.13}$$

$$I_\nu(\tau, \mu) = -\frac{1}{\mu} \int_0^\tau S_\nu(t) e^{(\tau-t)/\mu} \, \mathrm{d}t, \qquad (-1 \leq \mu \leq 0). \tag{2.14}$$

Using the formal solution of the radiative transfer equation to calculate the mean intensity J_ν (Eq. 2.3), we get

$$J_\nu(\tau_\nu) = \tfrac{1}{2} \int_0^\infty S_\nu(t_\nu) E_1(|t - \tau|)\, \mathrm{d}t \tag{2.15}$$

$$\equiv \Lambda_\tau[S] \tag{2.16}$$

where E_1 denotes the first exponential integral. Equation 2.16 introduces the lambda operator Λ to have an abbreviating notation for the integral expression in equation 2.15.

If we had knowledge about the run of the source function along the characteristics through the atmosphere of interest, equation 2.15 could easily be solved by (numerical) integration but this case usually never occurs, as explained below.

2.3 Numerical Radiative Transfer

In (nearly) all astrophysically relevant situations, the source function S itself depends on the run of the mean intensity and the integral expression of Eq. 2.15 cannot easily be solved. Even though the source function as the ratio of emission and absorption properties of the atmospheric material at the location under consideration may be thought of as a material property, it depends on the excitation and ionization rates of the corresponding material and thus, on the radiation field penetrating the matter. Hence, the properties of the atmospheric matter, describing the emission and absorption characteristics and the radiation field itself are strongly coupled. As the radiation field may propagate information of the matter due to scattering processes from one location to another, spatially divided points are connected to each other. This connection is stronger and couples spatially further away points within the atmosphere, the more prominent the scattering processes are as compared to the true absorption and emission processes. Actually this dependence on the radiation field itself, that from a physical point of view describes the radiative scattering, is responsible for the global communication of the boundary conditions over the atmosphere (Hauschildt and Baron, 2006). Even in the simple case of *local thermodynamic equilibrium* (LTE) thermal emission and coherent isotropic scattering, the source function must be written as

$$S_\nu = \frac{\kappa_\nu}{\kappa_\nu + \sigma_\nu} B_\nu + \frac{\sigma_\nu}{\kappa_\nu + \sigma_\nu} J_\nu \tag{2.17}$$

$$= (1 - \epsilon_\nu) B_\nu + \epsilon_\nu J_\nu \tag{2.18}$$

where κ and σ denote the pure absorption and scattering coefficient respectively, ϵ the thermal coupling parameter and B is the well-known Planck function which describes the photon distribution in

the case of strict thermodynamic equilibrium. Hence, we obtain Eq. 2.16 to be[3]

$$J = \Lambda[(1 - \epsilon)J + \epsilon B].$$ (2.19)

This equation can be solved numerically by iteration methods where the Λ-Operator is used to define a recursive sequence J_n, $n \in \mathbb{N}$ that converges to the desired mean intensity

$$J_{n+1} = \Lambda[(1 - \epsilon)J_n + \epsilon B].$$ (2.20)

This sequence fails to converge in an appropriate number of iterations in the case of large optical depths and small ϵ (Hauschildt and Baron, 2006) since the largest eigenvalue of the amplification matrix is approximately

$$\lambda_{\max} \approx (1 - \epsilon)\left(1 - T^{-1}\right),$$ (2.21)

where T is the optical thickness of the medium. For small ϵ and large T the largest eigenvalue $\lambda_{\max}$ is close to unity which leads to an extremely slow convergence rate. Because of this, various iteration acceleration methods have been applied which are intended to increase the convergence speed. The *operator splitting* (OS) technique as used in PHOENIX 3DRT makes use of an Λ-operator splitting method to reduce the eigenvalues of the amplification matrix in the iteration scheme by introducing an *approximate Λ-operator* (ALO) $\Lambda^\star$ and splitting Λ according to Cannon (1973)

$$\Lambda = \Lambda^\star + \left(\Lambda - \Lambda^\star\right).$$ (2.22)

By virtue of this splitting of the Λ-operator Eq. 2.20 can be rewritten as

$$\left[1 - \Lambda^\star(1 - \epsilon)\right]J_{n+1} = J_{\mathrm{fs}} - \Lambda^\star(1 - \epsilon)J_n,$$ (2.23)

where $J_{\mathrm{fs}} = \Lambda[S_n]$ is the formal solution with respect to the current estimate of the source function and J_n the corresponding mean intensity.

2.4 3D Radiative Transport

While one-dimensional radiative transfer simulations where plane parallel atmospheric structures are assumed perform as a good approximation for a wide range of stellar atmosphere calculations, these simplifications do not hold as soon as planetary atmospheres are considered: It is not just that the incident irradiation of the host star causes an obvious symmetry breaking by inducing a day- and night-side hemisphere respectively, at least in the case of terrestrial (rocky) planets every reasonable realistic model has to take the inhomogeneous surface coverage into account. The different *surface*

---

[3]Frequency subscript ν will be suppressed for clarity reasons from now on.
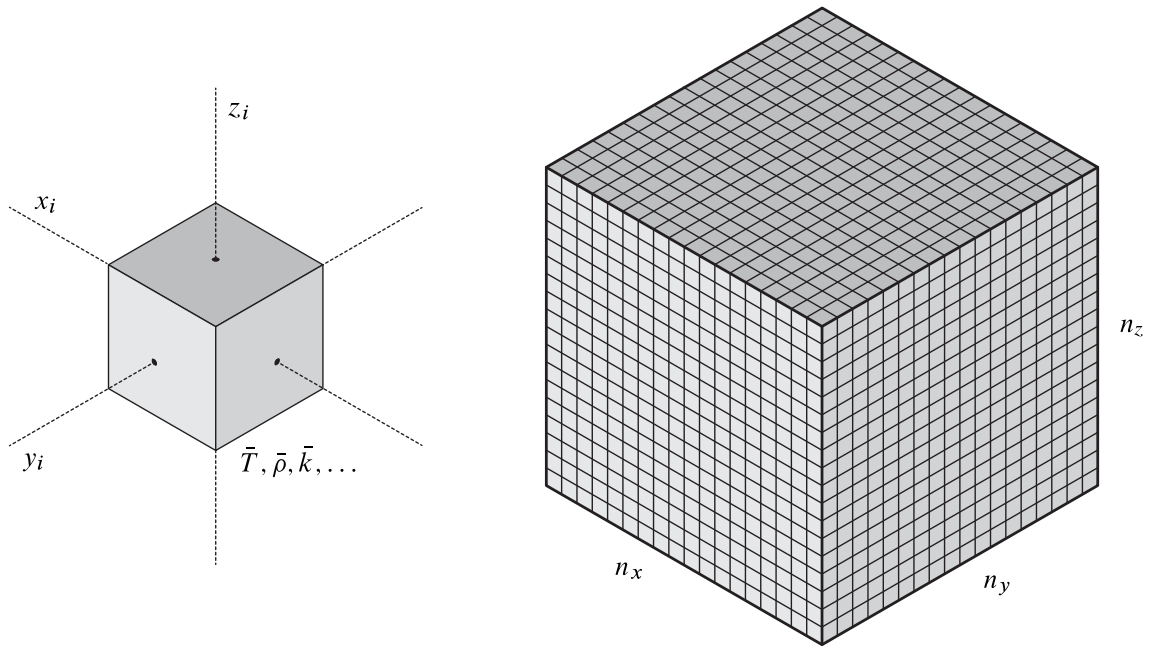
Figure 2.1. Radiative transfer processes are solved on voxel (volume element)-grids where each voxel represents the relevant physical quantities as an average over the volume element. Typical grids consist of about 32 voxels along each positive axis in Cartesian coordinates $n_x = n_y = n_z = 32$ resulting in a total of $(2 \cdot 32 + 1)^3 = 274625$ voxels.

textures like glacier ice, water (oceans) or sand/rocks (deserts) interact with the incident irradiation in completely different ways which has to be reflected in different boundary conditions for the model setup and hence to influence the radiative transfer calculations. The three-dimensional constellation of the star-planet-observer-system defines the spectra to be observed which may easily be seen in our own solar system where the relative fraction of transmission, reflection and emission spectra causes varying spectra of planets like Mars if observed at different dates.

Throughout this thesis, the model calculations have been performed with an extended (see ch. 3) version of the PHOENIX 3D radiative transfer framework (PHOENIX 3DRT) which accounts for the reflection of the host star's irradiation at the solid planetary surface. PHOENIX is a general-purpose state-of-the-art stellar and planetary atmosphere code, developed within the theory group of the Hamburg Observatory at the University of Hamburg. In PHOENIX 3DRT radiative transfer processes are solved on voxel (volume element)-grids where each voxel represents the relevant physical quantities such as temperature, density, opacities and mean intensities of the corresponding physical space as an average over the volume element (cf. fig. 2.1) and thus, the voxel grid also fixes the physical resolution of the atmospheric properties. To map a given model setup onto the voxel-grid, appropriate scaling factors have to be applied, depending on the problem to be modeled. A typical voxel-grid in the Cartesian coordinate system that is manageable by current maximum performance computation facilities like the *Höchstleistungsrechenzentrum Nord* (HLRN) or the *National Energy Research Scientific Computing Center* (NERSC) consist of about 32 voxels along each positive axis

in Cartesian coordinates $n_x = n_y = n_z = 32$ which specifies a voxel grid from voxel coordinates $(-32, -32, -32)$ to $(32, 32, 32)$, resulting in a total of $(2 \cdot 32 + 1)^3 = 274,625$ voxels, 65 along each axis (Hauschildt and Baron, 2006). In general, PHOENIX 3DRT is able to calculate models in different coordinate systems such as Cartesian coordinates, spherical coordinates or cylindrical coordinates. In a full three-dimensional model setup, the basic radiative transfer equation may be written as

$$\hat{\boldsymbol{n}} \cdot \nabla I_\nu(\boldsymbol{r}, \boldsymbol{n}) = j_\nu(\boldsymbol{r}) - k_\nu(\boldsymbol{r}) I_\nu(\boldsymbol{r}, \boldsymbol{n}). \tag{2.24}$$

The formal solution can be performed if we assume characteristics that pass continuously through the atmosphere's voxel grid representation and use the distances between different voxels along the various characteristics to compute optical depths. The formal solution is then derived using piece-wise parabolic (PPM) or piece-wise linear (PLM) interpolation and integration of the source function where PHOENIX 3DRT automatically restricts itself to piece-wise linear interpolation. If either the piece-wise parabolic interpolation along the three points is larger than a prescribed threshold (typically factors of 100) or the optical depth along the characteristic is very small (typically less the 10^{-3}) (Hauschildt and Baron, 2006) the high-order interpolations may cause problems in these cases (Auer, 2003). Along a characteristic the transfer equation again simplifies to[4]

$$\frac{\mathrm{d}I}{\mathrm{d}\tau} = I - S \tag{2.25}$$

(cf. Eq. 2.12). If τ_i denotes the optical depths along the characteristics through the atmosphere with $\tau_1 \equiv 0$; $t_{i-1} \leq \tau_i$, the formal solution of the transfer equation can be written as

$$I(\tau_i) = I(\tau_{i-1}) \exp(\tau_{i-1} - \tau_i) + \int_{\tau_{i-1}}^{\tau_i} S(\tau) \exp(\tau - \tau_i) \, \mathrm{d}\tau$$

$$= I_{i-1} \exp(-\Delta\tau_{i-1}) + \Delta I_i \tag{2.26}$$

where i labels the points along the characteristic and $\Delta\tau_i$ is calculated using piece-wise linear interpolation of k along the characteristic (Hauschildt and Baron, 2006)

$$\Delta\tau_{i-1} = \tfrac{1}{2}(k_{i-1} + k_i)|s_{i-1} - s_i|. \tag{2.27}$$

As mentioned above, the source function $S(\tau)$ is calculated using piece-wise parabolic or piece-wise linear interpolation. Hence, the specific intensity results in

$$\Delta I_i = \alpha_i S_{i-1} + \beta_i S_i + \gamma_i S_{i+1} \tag{2.28}$$

---

[4]For the sake of clarity, again, the frequency subscript ν is suppressed from now on.

where the interpolation coefficients α_i, β_1 and γ_i are defined as

$$\alpha_i = \frac{e_{0i} + [e_{2i} - (\Delta\tau_i + 2\Delta\tau_{i-1})e_{1i}]}{\Delta\tau_{i-1}(\Delta\tau_i + \Delta\tau_{i-1})} \tag{2.29}$$

$$\beta_i = \frac{(\Delta\tau_i + \Delta\tau_{i-1})e_{1i} - e_{2i}}{\Delta\tau_i \Delta\tau_{i-1}} \tag{2.30}$$

$$\gamma_i = \frac{e_{2i} - \tau_{i-1}e_{1i}}{\Delta\tau_i(\Delta\tau_i + \Delta\tau_{i-1})} \tag{2.31}$$

for the case of parabolic interpolation and

$$\alpha_i = e_{01} - \frac{e_{1i}}{\Delta\tau_{i-1}} \tag{2.32}$$

$$\beta_i = \frac{e_{1i}}{\Delta\tau_{i-1}} \tag{2.33}$$

$$\gamma_i = 0 \tag{2.34}$$

for the case of linear interpolation respectively. The auxiliary functions e_{1i}, e_{2i} and e_{3i} are given by

$$e_{0i} = 1 - \exp(-\Delta\tau_{i-1}) \tag{2.35}$$

$$e_{1i} = \Delta\tau_{i-1} - e_{0i} \tag{2.36}$$

$$e_{2i} = \Delta\tau_{i-1}^2 - 2e_{1i} \tag{2.37}$$

(cf. Olson and Kunasz, 1987). The linear interpolation coefficients have to be used at the last integration step along each characteristic and may also be used within the integration path along a given characteristic to improve numeric stability (Hauschildt and Baron, 2006).

As demonstrated in the latter section the mean intensity J_i is needed at every point of the corresponding grid to compute the full solution of the radiative transfer problem. Hence, the integral of the specific intensity over all solid angles is numerically performed, using Monte-Carlo integration methods

$$J_i = \tfrac{1}{2\pi^2} \sum_{(\theta,\varphi)} I_i(\theta,\varphi)\sin\theta \tag{2.38}$$

where the summation is done over all pairs of θ and φ, specifying the characteristics passing through of voxel under consideration. The total number of pairs, sampling the characteristics' phase space is $n_{\text{tot}} = n_\theta n_\varphi$ where the directions are evenly distributed.

3. Planetary Albedo

To model planetary transmission and reflection spectra it is crucial to get the individual intrinsic spectra right, on the one hand of the irradiating host star and on the other hand of the planet's thermal emission itself. Furthermore, the reflected intensities of the host star's irradiation at the planetary surface have to be taken into account. Because of the linearity of the radiative transfer equation, the different radiation fields may be treated as individual from each other from a mathematical point of view. But as the host star is the dominant energy source in the planetary system—thermal energy from planetary geological activities such as intrinsic planetary heat from the inner core, radioactive decays as well as tidal heating or accretional heating, can typically be neglected after some point in the planet's evolution—this has to be reflected in the corresponding model setup. Of course, the planet's intrinsic thermal spectra is not independent from the host star's radiation field, because the star's irradiation feeds the planet's thermal energy pool and thus, determines the planet's radiation field, the thermal emission as well as the reflected light.

The amount of energy from the incident irradiation which is deposited in the planet's thermal energy pool is generally described in terms of *surface albedos*. In its most basic form, albedo describes the diffuse, i.e. Lambertian, reflectivity of a planet's surface and is defined as the ratio of reflected radiation leaving the surface under consideration to the total irradiation to the surface. This basic description of surface reflectivity may be thought of as some kind of energy budget treatment where neither the directions of incoming and outgoing intensities nor the intensity's wavelength distribution are considered. Hence, valid albedo values range from zero, which mean no reflected radiation at all and thus total absorption, to one which describes a perfect white reflector that does not absorb any of the incident irradiation. Of course, albedo is generally both wavelength and angular dependent and during a reflection event the direction as well as the wavelength may be altered. These dependencies can be expressed by the *bidirectional reflectance distribution function* (BRDF) f_r that characterizes surface reflectance for all combinations of incident and reflected angles and may be integrated over source and detector solid angles to get measurable optical properties, such as biconical reflectance, as defined in Nicodemus' National Bureau of Standards monograph (Nicodemus et al., 1977)

$$f_{r,\nu}\left(\theta_\downarrow,\varphi_\downarrow\,;\,\theta_\uparrow,\varphi_\uparrow\right) = \frac{I_{\nu,\uparrow}\left(\theta_\uparrow,\varphi_\uparrow\right)}{I_{\nu,\downarrow}\left(\theta_\downarrow,\varphi_\downarrow\right)\cos\theta_\downarrow\,\mathrm{d}\Omega_\downarrow}, \tag{3.1}$$

where θ and φ denote the polar and azimuthal angle, respectively of the corresponding directional vector and quantities indexed by $\downarrow$ and $\uparrow$ refer to the downward (irradiated) and upward (reflected)

intensities, respectively. For the sake of simplicity, the frequency subscript ν will be suppressed from now on.

From an astrophysical point of view the BRDF describes a redistribution function in a specialized case (lower boundary) where the characteristics necessarily have to be reflected at a solid surface. The incident irradiation is either reflected in some direction within the half sphere above the surface or absorbed by the planet. This is where the boundary condition of an earth-like planet with a solid surface crust finds its representation in the corresponding model setup: all the incident irradiation has either to be stored and contribute to the planet's thermal energy pool or to be reflected where the BRDF works as a specialized redistribution function.

In some situations—as in meteorological model setups for the sun-earth configuration—it might be reasonable to consider the basic albedo description which accounts for the energy budget only and thus neglects the wavelength and angular dependencies of the surface reflection. This usually implies a simplified treatment of the incident and emitted radiation onto/from the planet's surface, where the planet's long wavelength radiation field is considered as independent from the host star's short wavelength irradiation if the corresponding Planck functions peak at very different wavelengths[1]. This is a common simplification in many meteorological model codes as with the PUMA and Plasim model code, where the whole spectrum is described by two extremely broad spectral bands (short and long wavelength radiation). In the case of the PUMA/Plasim model, short and long wavelength domains are defined as $\mathcal{D}_< = [0\,\text{nm}, 750\,\text{nm}]$ and $\mathcal{D}_> = [750\,\text{nm}, \infty\,\text{nm}]$ respectively and averaged opacities are calculated by parameterized transmissivity functions for ozone (affecting short wave domain), water vapor and CO_2 (long wave domain) and H_2O-clouds (short wave domain: Rayleigh scattering, long wave domain: Rayleigh scattering and absorption). With this description only the total energy budget is taken into account and albedo is treated as independent of angle and evaluated at the peak wavelength of the host star's irradiation. This concept holds as long as only energy budgets are of interest and naturally fails if spectral energy distributions are to be calculated. Nevertheless this approach has proven itself valuable in the circulation models and hence, the model code developed for this thesis makes use of an energy budget based circulation model as well to calculate surface and atmospheric temperature profiles.

Treated in more detail as for astrophysical radiative transfer modeling purposes, the concept of BRDFs is highly complex because of the vast parameter-space if the model setup should be realistic to some extent and must be approached with advanced numerical models in nearly all applications[2]. The basic question in this context is the desired scale of details to be modeled: On the one hand, the generalized concept of wavelength and angular independent albedo—which can be understood as extremely low scale of model detail—is inappropriate for the aim of extending the PHOENIX 3DRT model code to simulate planetary reflection and transmission spectra where the spectral composition

---

[1]In the sun-earth system the Planck functions have their maxima at about $\lambda_{\max}^{\odot} = 500\,\text{nm}$ ($T_{\text{eff}}^{\odot} = 5778\,\text{K}$) for the sun and at $\lambda_{\max}^{\oplus} = 11.36\,\mu\text{m}$ ($T_{\text{eff}}^{\oplus} = 255\,\text{K}$) for our own earth, respectively.

[2]Again, this is the reason why fully resolved radiative transfer calculations cannot be used to achieve self-consistent temperature corrections in a 3D radiative transfer setup.

of the radiation itself is of basic interest rather than just the planetary energy budget that is used in most meteorological model applications. On the other hand it is not sensible to model each and every little detail of a complex structured surface because this would not increase the accuracy of the modeled spectra but expand the model parameter-space beyond any manageable limit.

Because of the presented arguments, albedo is treated in a two-pronged way in the model used for this thesis: The simplified albedo description that is used by the `PUMA/Plasim` framework is still used for energy budget calculation and hence for all effects concerning the atmospheric circulation calculations. In particular this includes the surface temperature as well as atmospheric temperature profile. The corresponding albedo map, describing the albedo values for the latitude/longitude grid of the planet may be prescribed if needed but is calculated by default, using the diffuse, Lambertian part of the detailed wavelength and angular dependent BRDF model which is derived in this chapter. Having a valid temperature structure, the full BRDF model is used for all radiative transfer purposes.

3.1 BRDF Formalism in Astrophysical Applications

Nicodemus et al. (1977) give an adequate definition of the average BRDF that is appropriate for structured surfaces where the BRDF is extended to the *Bidirectional Surface Scattering Reflectance Distribution Function* (BSSRDF) $\mathcal{S}_r$ and defined at an horizontal reference plane above all surface structure. The BSSRDF is a generalization of the BRDF where the incident irradiation hits a horizontal reference plane above the structured surface at an infinitesimal surface element $\mathrm{d}\sigma_\downarrow$ rather than the structured surface itself, may scatter internally and exit at another location. If a surface element $\mathrm{d}\sigma_\downarrow$, centered at $(x_\downarrow, y_\downarrow)$ on the horizontal reference plane, is irradiated by the incident intensity $I_\downarrow$ from an angle $(\varphi_\downarrow, \theta_\downarrow)$, the radiation will be reflected (at least partly) and leave the reference plane as $I_\uparrow$ at $(x_\uparrow, y_\uparrow)$ in the direction $(\varphi_\uparrow, \theta_\uparrow)$ (cf. fig. 3.1). The BSSRDF is defined as

$$\mathcal{S}_r(\theta_\downarrow, \varphi_\downarrow \,;\, \theta_\uparrow, \varphi_\uparrow \,;\, \sigma_\downarrow, \sigma_\uparrow) = \frac{I_\uparrow(\theta_\uparrow, \varphi_\uparrow \,;\, \sigma_\uparrow)}{I_\downarrow(\theta_\downarrow, \varphi_\downarrow \,;\, \sigma_\downarrow) \cos\theta_\downarrow \,\mathrm{d}\Omega_\downarrow}. \tag{3.2}$$

Using this definition the average BRDF for structured surfaces is then defined by the integral of the BSSRDF over an appropriate averaging area. Of course, this area depends on the scale of the material structure and is simply large enough so that the resulting average BRDF is independent of the point of observation. Here, the integral is over the neighborhood B of the incident position $\sigma_\downarrow$ for a fixed observation point (C. Snyder and Wan, 1998)

$$\mathit{f}_r(\Omega_\downarrow, \Omega_\uparrow, \nu_\downarrow, \nu_\uparrow) = \int\limits_{B(\sigma_\downarrow)} \mathcal{S}_r(\Omega_\downarrow, \Omega_\uparrow, \sigma_\downarrow, \sigma_\uparrow, \nu_\downarrow, \nu_\uparrow) \,\mathrm{d}\sigma_\downarrow. \tag{3.3}$$
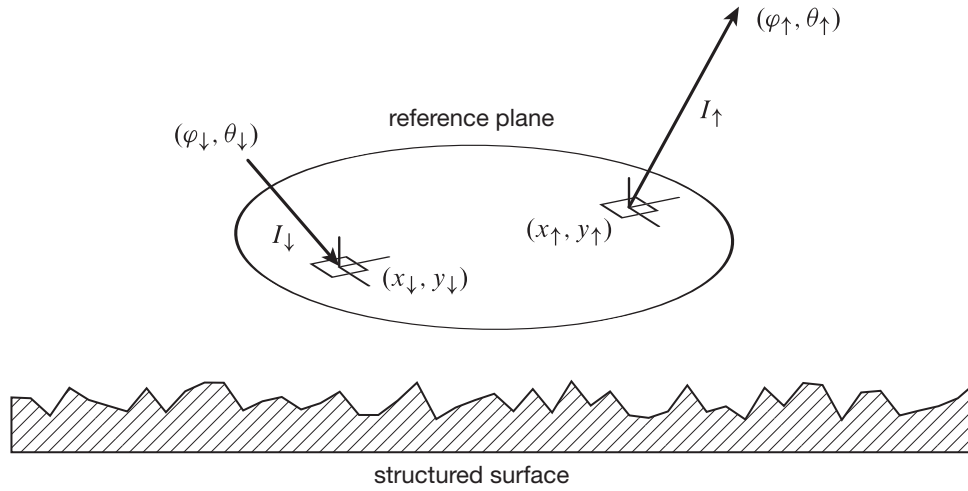
Figure 3.1. Schematic diagram of the BSSRDF geometry. A surface element $d\sigma_\downarrow$ centered at $(x_\downarrow, y_\downarrow)$ on the horizontal reference plane is irradiated by the incident intensity $I_\downarrow$ from an angle $(\varphi_\downarrow, \theta_\downarrow)$. The radiation will be reflected and leave the reference plane as $I_\uparrow$ at $(x_\uparrow, y_\uparrow)$ in the direction $(\varphi_\uparrow, \theta_\uparrow)$.

3.2 BRDF Model Requirements

BRDF models have to fulfill two important requirements to represent sensible models from a physical point of view. The first requirement is the trivial assumption of energy conservation. If energy sources apart from radiative and deposed thermal energy are neglected, this basically states that the integral of the reflected intensities over all solid angles and frequencies at a surface element $d\sigma$, in addition to the amount of energy that has been emitted by the surface element in the time dt, must equal the integral of the incident irradiation over all solid angles, in addition to the amount of energy that has been absorbed by the surface element in the same time, which is commonly known as radiative equilibrium. Neglecting energy sources apart from the aforementioned radiative and deposed thermal energy—where deposed refers to the host star's irradiation—means in particular that some geological effects cannot be considered within the model even though they might play an important role in the energy budget such as intrinsic planetary heat from the inner core, radioactive decays, tidal heating or accretional heating. Especially at an early point in the planetary evolution the intrinsic thermal energy due to the planet's core or accretional heating can be dominant with respect to it's energy budget and hence, one has to keep in mind that the model developed in this thesis is not applicable to these young planets, where the surface temperature is dominantly determined by it's geological activity, without further modifications.

In the following it is assumed that the planet is in a quasi steady-state situation, where the host star's irradiation is balanced with the planet's thermal emission and that a periodic surface temperature correlated with the planet's rotational and orbital period may be defined. In the case of a steady-state

situation of the planet's thermal energy pool the abovementioned demand simplifies to

$$\int\limits_0^\infty \mathrm{d}\nu \int\limits_{\Omega^+} \mathrm{d}\Omega\, I_\downarrow(\Omega_\downarrow, \nu_\downarrow) = \int\limits_0^\infty \mathrm{d}\nu \int\limits_{\Omega^+} \mathrm{d}\Omega\, I_\uparrow(\Omega_\uparrow, \nu_\uparrow) \tag{3.4}$$

where Ω^+ refers to the positive hemisphere with respect to the reference plane's normal $\hat{n}_\mathrm{r}$ which may be defined as

$$\Omega^+ = \{\hat{e} \mid \hat{e} \cdot \hat{n}_\mathrm{r} \geq 0\}. \tag{3.5}$$

In principle, only tidally locked planets can strictly fulfill radiative equilibrium as the different day- and night-side irradiation of the host star causes the planet to absorb more radiative energy than it emits on the day-side hemisphere and vice versa, of course. This has to be neglected in the model and radiative equilibrium is assumed for surface elements of rotating planets as well.

The latter equation does not hold in the case of the generalized BRDF which is defined via a reference plane above the structured surface, because the incident irradiation may leave the plane at another location, and therefore this condition has to be reformulated into a demand where the quantities of equation 3.4 equal each other when integrated additionally over some adequate area $B(\sigma_\downarrow)$ so that the generated averages compensate for the details of the structured surface

$$\int\limits_{B(\sigma_\downarrow)} \mathrm{d}\sigma_\downarrow \int\limits_0^\infty \mathrm{d}\nu \int\limits_{\Omega^+} \mathrm{d}\Omega\, I_\downarrow(\sigma_\downarrow, \Omega_\downarrow, \nu_\downarrow) = \int\limits_{B(\sigma_\downarrow)} \mathrm{d}\sigma_\uparrow \int\limits_0^\infty \mathrm{d}\nu \int\limits_{\Omega^+} \mathrm{d}\Omega\, I_\uparrow(\sigma_\uparrow, \Omega_\uparrow, \nu_\uparrow). \tag{3.6}$$

The area $B(\sigma_\downarrow)$ defines the degree of detail that can be modeled and is characterized by the underlying BRDF model. With respect to the BRDF itself this states that the amount of reflected energy flux may not exceed the amount of irradiated energy flux when integrated over the hemisphere

$$\int\limits_{\Omega^+} f_r(\Omega_\downarrow, \Omega_\uparrow, \nu_\downarrow, \nu_\uparrow) \cos\theta_\uparrow \,\mathrm{d}\Omega_\uparrow \leq 1. \tag{3.7}$$

The second important requirement is the Helmholtz reciprocity principle. A reciprocal model is one which gives the same value of the BRDF when the incident and reflected angles are switched

$$f_r(\varphi_\downarrow, \theta_\downarrow\,;\, \varphi_\uparrow, \theta_\uparrow) = f_r(\varphi_\uparrow, \theta_\uparrow\,;\, \varphi_\downarrow, \theta_\downarrow). \tag{3.8}$$

It is evident from 3.3 that if the BSSRDF S_r is reciprocal, in other words, if

$$S_r(\varphi_\downarrow, \theta_\downarrow, x_\downarrow, y_\downarrow\,;\, \varphi_\uparrow, \theta_\uparrow, x_\uparrow, y_\uparrow) = S_r(\varphi_\uparrow, \theta_\uparrow, x_\uparrow, y_\uparrow\,;\, \varphi_\downarrow, \theta_\downarrow, x_\downarrow, y_\downarrow) \tag{3.9}$$

then the integrated average BRDF is reciprocal as well. It is not possible to prove in general that a

given material will have a reciprocal BRDF, but reciprocity holds for common materials. If it does hold, then for the single scattering case of a structure of common materials, each BSSRDF path is reciprocal. Any arbitrary combination of incident angle, reference surface locations and output angle defines a transfer geometry at some scattering element on the surface structure, or it defines a blocked path. If the path is blocked, the transfer is zero in both directions, so it is reciprocal trivially. In the case of a single-reflection path, reciprocity of the BSSRDF can be shown by straightforward radiometric calculations (Snyder, 1998). Multiple scattering events with opaque and translucent materials also give reciprocal BSSRDF paths, which is more difficult to show and hence, is addressed separately by Snyder (1998). Thus all BSSRDF paths are reciprocal, and so the average BRDF is reciprocal.

3.3 BRDF Models

The BRDF is needed in remote sensing for the correction of view and illumination angle effects (for example in image standardization and mosaicking), for deriving albedo, for land cover classification, for cloud detection, for atmospheric correction and other applications. It gives the lower radiometric boundary condition for any radiative transfer problem in the atmosphere and is hence of relevance for climate modeling and energy budget investigations as well as calculation of planetary spectra, of course. In all these fields of research, the development of adequate BRDF models has been strained for a variety of different applications. These models may be categorized as follows:

Direct Measurement Models BRDFs can be measured directly using gonioreflectometers which mechanically vary the direction to a small light source and a spectral sensor and thus collect a large number of point samples for the BRDF (Greenberg, 1999). Simpler and less accurate devices can also be constructed using CCD imaging devices (Ward, 1992). More complex CCD devices can also be used which gather data quickly with accuracy very close to full gonioreflectometry (Ashikhmin et al., 2000; Marschner et al., 1999). If enough is known about the microstructure of a material, a BRDF can be simulated by using a virtual gonioreflectometer where statistical ray tracing followed by density estimation is used to create BRDF data (Cabral et al., 1987; Gondek et al., 1994; Westin et al., 1992). Although these models are very accurate for a given material or surface structure they are most inflexible too. BRDFs of this kind are usually just tabulated measurement data that must be inter- or extrapolated in all applications that have not directly been measured e.g. wavelength domains beyond the visual band. Therefore, these models are inappropriate in astrophysical applications.

Empirical Models There exists a variety of purely empirical reflection models, the most familiar being the models introduced by Gouraud and Phong (Gouraud, 1971; Phong, 1975). These two initial models were meant to be used with hand-picked parameters, and thus these parameters are intuitive. A variety of more complex methods have been introduced to improve characteristics of the Phong model for efficiency (Kurt et al., 2010), to include anisotropy (Ward, 1992),

and enforce physical constraints such as reciprocity (Lafortune and Willems, 1994). Other models have been developed to fit measurement data as opposed to being intuitive (Lafortune et al., 1997). Although some extensions to existing models have been proposed to account for physical principles such as energy conservation, the focus of these models is on the visual impression when used in computer graphics rather than on physical correctness and in that these models are less sensible for the usage in astrophysical applications as well.

Height Correlation Models In these methods a rough surface is a realization of some Gaussian random process. Such a process can be described by its correlation function which is directly related to surface height correlations. This is the most complete surface representation used in computer graphics. Some of the most detailed descriptions of light scattering by a surface, including wave optics effects, were obtained using this approach (He et al., 1991). In particular these kinds of BRDF models take a lot of electrodynamical effects such as polarization into account and in that can be thought of as most accurate models from a physical point of view. However, the price of this accuracy is high complexity, as well as restriction to applications where a very detailed knowledge about all micro-structure properties of the structured surface is available. As the BRDF model for this thesis is intended to model planetary surface reflectance for a variety of surface structures at an adequate degree of accuracy, and the PHOENIX 3DRT model code is currently incapable of handling polarization effects, these models, again are inappropriate in this context although a more detailed investigation in further research on this topic could possibly make an adapted model of this kind a good choice, but this would definitely go beyond the scope of this thesis.

Microfacet Models Somewhere between the height correlation methods and empirical methods lie models based on microfacet theory (Blinn, 1977; Cook and Torrance, 1982). Microfacet models assume the surface consists of a large number of small flat "micromirrors" (facets) each of which reflect light only in the specular direction. By computing the number of visible microfacets at the appropriate orientation to specularly reflect light from the source to the viewer, one can determine the BRDF (Ashikhmin et al., 2000).

All of these methods have their place. In applications where little is known about the low-level properties of the surface, measurement is essential. Where physical optics effects are important, height correlation methods should be used (Ashikhmin et al., 2000). The interest of this thesis is to model planetary reflectance properties of structured planetary surfaces to a degree of realism that takes all important physical principles e.g., energy conservation and reciprocity into account and is adjusted to the degree of realism that can be expected from other components of the model framework like the radiative transfer or the meteorological circulation effects. Hence, the microfacet BRDF model has been chosen as lower boundary model in this thesis.

3.4 Microfacet BRDF

The basis for microfacet BRDF is microfacet theory. This theory has been developed to describe surface reflection from general (non-optically flat) surfaces (Walter et al., 2007). The basic assumption underlying microfacet theory is that the surface is composed of many microfacets, too small to be seen individually. Each microfacet is assumed to be optically flat. The microfacet BRDF was first described by Cook and Torrance (1982). If not denoted otherwise the following section is based on the Microfacet reflection model by Walter et al. (2007), the Microfacet-based BRDF generator by Ashikhmin et al. (2000) and the lecture notes by McAuley et al. (2012) describing physically-based shading effects. The model requires that the wavelength of the incident irradiation is much smaller than the average size of the individual microfacets

$$\lambda \ll \sqrt{\frac{1}{N} \sum_{i=1}^{N} \Delta_i^2} \tag{3.10}$$

where Δ is the size of an individual microfacet. As the BRDF model has originally been developed for the case of modeling reflection of light in the visual wavelength domain ($\lambda \sim 10^2$ nm) for rendering purposes in computer graphics, this has not been a real limitation, but if we want to model reflection of surface textures like forests (leaves: $\Delta \sim 10$ cm) or deserts (grain of sand: $\Delta \sim 1$ mm) we have to keep in mind that the model does not hold for wavelengths of the microwave regime or longer. In fact, the size of a single microfacet to be considered mainly depends on the degree of realism to be achieved: Of course, a leaf could be subdivided into multiple microfacets to map the surface more precisely but again, the degree of detail has to be in keeping with capabilities of the overall framework. Furthermore the size of the microfacets is not directly considered in the final BRDF model and hence, the size limitation is just a rough estimate for the validity of the developed model.

In the microfacet theory two assumptions are made concerning the overall appearance of the surface to be modeled:

1. The normals $\hat{n}_{\mathrm{m}}$ of the individual microfacets are distributed according to an underlying probability density function $p(\hat{n}_{\mathrm{m}})$. Although the distribution may in principle be arbitrary, the average over all solid angles should point in the $\theta = 0$ direction for any reasonable distributions as this actually is the definition of the surface orientation.

2. An individual microfacet contributes to the BRDF at a given pair of incident irradiation direction $\hat{k}_{\downarrow} = (\theta_{\downarrow}, \varphi_{\downarrow})$ and reflection direction $\hat{k}_{\uparrow} = (\theta_{\uparrow}, \varphi_{\uparrow})$ if, and only if, it is visible i.e. neither shadowed (the incident irradiation direction $\hat{k}_{\downarrow}$ is blocked) nor masked (the reflected direction $\hat{k}_{\uparrow}$ is blocked) Although in microfacet theory the terms shadowed and masked are used to describe different effects, the BRDFs have to fulfill the reciprocity requirement and as each effect is transformed in the other effect respectively, when incidence and reflection direction is switched, both effects are denoted as shadowing.
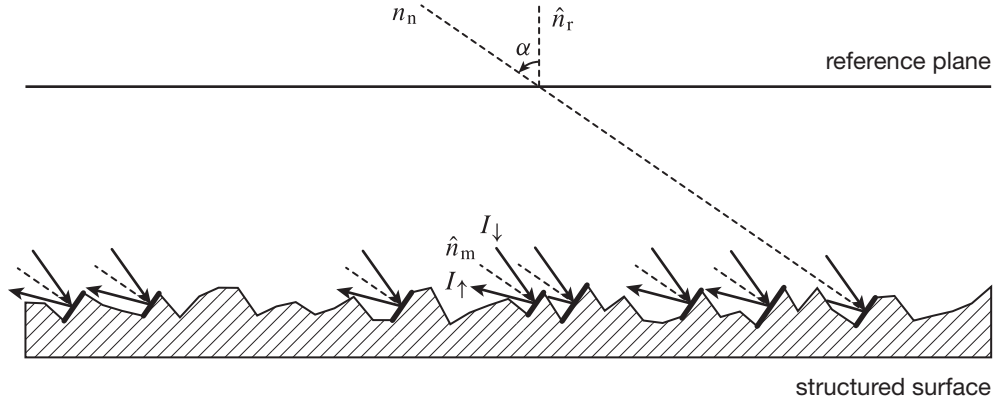
Figure 3.2. Schematic diagram of the microfacet BRDF configuration. The microfacets (bold black lines) are supposed to be equally distributed with respect to the reference plane and the normals $\hat{n}_m$ of the individual microfacet to have an inclination α to the normal of the reference plane $\hat{n}_r$ where the inclination angles are distributed according to $p(\hat{n}_m)$. Note in particular that some of the microfacets are not visible i.e. they are shadowed or blocked.

For the following derivation of the BRDF model, the geometry illustrated in fig. 3.3 is assumed. If the surface element under consideration is irradiated by the incident intensity $I_\downarrow$, coming from the infinitesimal solid angle $\mathrm{d}\Omega_\downarrow$ around $\hat{k}_\downarrow$, the reflected intensity along the characteristic in the direction $\hat{k}_\uparrow$ will be

$$I_\uparrow = f_r(\hat{k}_\downarrow, \hat{k}_\uparrow) I_\downarrow \mu(\hat{k}_\downarrow, \hat{n}_m)\, \mathrm{d}\Omega_\downarrow \tag{3.11}$$

where $\mu(\hat{k}_\downarrow, \hat{n}_m) = \cos \angle(\hat{k}_\downarrow, \hat{n}_m)$. This is directly deduced from the definition of the BRDF and my even be thought of as an alternative definition in the manner of the specific intensity's definition (Eq. 2.1). Moreover the reflected energy flux $\mathrm{d}E$ at the frequency under consideration can be written as

$$\mathrm{d}E = I_\uparrow \sigma \mu(\hat{k}_\uparrow, \hat{n}_m)\, \mathrm{d}\Omega_\uparrow \tag{3.12}$$

and the combination of the latter two equations gives

$$f_r(\hat{k}_\downarrow, \hat{k}_\uparrow) = \frac{\mathrm{d}E}{\sigma I_\downarrow \mu(\hat{k}_\downarrow, \hat{n}_m) \mu(\hat{k}_\uparrow, \hat{n}_m)\, \mathrm{d}\Omega_\downarrow\, \mathrm{d}\Omega_\uparrow}. \tag{3.13}$$

As the microfacets' normals are distributed according to a probability density function $p(\hat{n}_m)$ only a fraction of all microfacets will contribute to the reflection from characteristic $\hat{k}_\downarrow$ to characteristic $\hat{k}_\uparrow$. The vector $\hat{n}_m$ of the microfacets, appropriate to reflect the incident irradiation to the direction under consideration is the normalized half-vector between $\hat{k}_\downarrow$ and $k_\uparrow$ (cf. figure 3.3). The angle α is defined as the angle between the normal of the microfacets $\hat{n}_m$ and the normal of the reference plane $\hat{n}_r$. In the
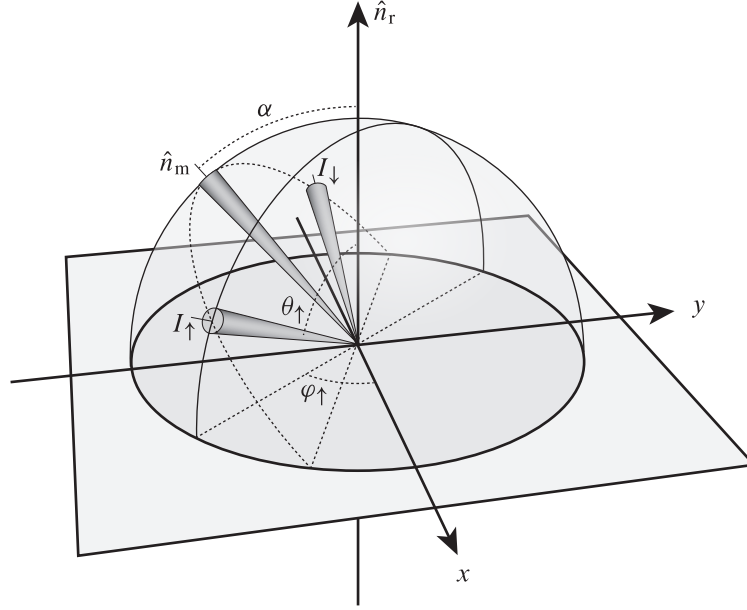
Figure 3.3. Schematic diagram of the BRDF reflection geometry. Incidence direction, reflection direction and microfacet normal $\hat{n}_m$ form a great circle on the sphere around the reflection point. The microfacet normal $\hat{n}_m$ is the bisector of the angle between incidence and reflection direction.

case of an isotropic BRDF the probability density function p only depends on this angle and may be simplified to $p(\hat{n}_m) = p(\alpha)$. If all microfacets have the same size $\sigma_m = \pi \Delta^2$ and a total number of N_{active} microfacets participate in the reflection progress, the projected area of all relevant microfacets is

$$\sigma = N_{active}\, \sigma_m\, \mu(\hat{k}, \hat{n}_m) \tag{3.14}$$

the total reflected energy flux can be written as

$$dE = I_\downarrow\, N_{active}\, \sigma_m\, \mu(\hat{k}, \hat{n}_m)\, F(\mu(\hat{k}, \hat{n}_m)) \tag{3.15}$$

where subscript of $\hat{k}$ has been dropped because $\mu(\hat{k}, \hat{n}_m)$ is symmetric with respect to incidence and reflection direction and $F(\mu(\hat{k}, \hat{n}_m))$ denotes the Fresnel coefficient giving the fraction of specularly reflected light with respect to the incident irradiation of a given material under the angle of consideration. The Fresnel coefficients describe the behavior of light with respect to reflection and transmission at a boundary of media with differing refractive indices.

According to the probability density function p only $Np(\hat{n}_m)\, d\Omega_{\hat{n}_m}$ microfacets are oriented in an appropriate direction to contribute to the reflected intensity. Moreover Torrence and Sparrow (1967) showed that for the case of specularly reflecting microfacets the relationship between the solid angle of the reflected intensity $d\Omega_\uparrow$ and the solid angle in the space of the microfacets' orientation distribution[3]

---

[3]It has to be emphasized that the space of solid angles with respect to incident and reflected intensities and the space of

$\mathrm{d}\Omega_{\hat{n}_{\mathrm{m}}}$ is

$$\mathrm{d}\Omega_{\uparrow} = 4\mu(\hat{k}_{\downarrow}, \hat{n}_{\mathrm{m}})\,\mathrm{d}\Omega_{\hat{n}_{\mathrm{m}}}. \tag{3.16}$$

As mentioned above, not only the orientation of the microfacets determines if an individual microfacet will contribute to the single-bounce reflection event, the microfacet must also be visible i.e. not shadowed. Introducing the probability $P(\hat{k}_{\downarrow}, \hat{k}_{\uparrow}, \hat{n}_{\mathrm{m}})$ of an individual microfacet *not* to be shadowed, the number of microfacets that contribute N_{active} may be written as

$$N_{\mathrm{active}} = N p(\hat{n}_{\mathrm{m}}) P(\hat{k}_{\downarrow}, \hat{k}_{\uparrow}, \hat{n}_{\mathrm{m}})\,\mathrm{d}\Omega_{\hat{n}_{\mathrm{m}}} \tag{3.17}$$

and combining the equations (3.15), (3.16), (3.17) with (3.13) yields to

$$\ell_r(\hat{k}_{\downarrow}, \hat{k}_{\uparrow}) = \frac{N\sigma_{\mathrm{m}} p(\hat{n}_{\mathrm{m}}) P(\hat{k}_{\downarrow}, \hat{k}_{\uparrow}, \hat{n}_{\mathrm{m}}) F(\mu(\hat{k}, \hat{n}_{\mathrm{m}}))}{4\sigma\mu(\hat{k}_{\downarrow}, \hat{n}_{\mathrm{m}})\mu(\hat{k}_{\uparrow}, \hat{n}_{\mathrm{m}})}. \tag{3.18}$$

The area σ of the surface element can be written as the projected areas of all microfacets that are not shadowed with respect to the direction of the reference plane's normal $\hat{n}_{\mathrm{r}}$. Given the probability $P(\hat{n}_{\mathrm{r}}, \hat{n}_{\mathrm{m}})$ that an individual microfacet with normal $\hat{n}_{\mathrm{m}}$ is not shadowed with respect to the reference plane's normal $\hat{n}_{\mathrm{r}}$ the surface element's area σ can be written as

$$\sigma = \sum_{\mathrm{facets}} \sigma_{\mathrm{m}}\mu(\hat{n}_{\mathrm{r}}, \hat{n}_{\mathrm{m}}) P(\hat{n}_{\mathrm{r}}, \hat{n}_{\mathrm{m}}) \tag{3.19}$$

$$= N\sigma_{\mathrm{m}} \int_{\Omega} \mu(\hat{n}_{\mathrm{r}}, \hat{n}_{\mathrm{m}}) P(\hat{n}_{\mathrm{r}}, \hat{n}_{\mathrm{m}}) p(\hat{n}_{\mathrm{m}})\,\mathrm{d}\Omega_{\hat{n}_{\mathrm{m}}} \tag{3.20}$$

$$= N\sigma_{\mathrm{m}}\langle\mu(\hat{n}_{\mathrm{r}}, \hat{n}_{\mathrm{m}}) P(\hat{n}_{\mathrm{r}}, \hat{n}_{\mathrm{m}})\rangle \tag{3.21}$$

where the ensemble average of Eq. 3.19 has been replaced by the integral over the corresponding probability density function and hence the average over the distribution of its random variable in Eq. 3.20 while the term $\langle f(\hat{n}_{\mathrm{m}})\rangle$ in Eq. 3.21 is just a shorthand for the distribution average

$$\langle f(\hat{n}_{\mathrm{m}})\rangle \equiv \int_{\Omega} f(\hat{n}_{\mathrm{m}}) p(\hat{n}_{\mathrm{m}})\,\mathrm{d}\Omega_{\hat{n}_{\mathrm{m}}}. \tag{3.22}$$

Using Eq. 3.21 for the surface element's area in the denominator of Eq. 3.18 the BRDF can be written as

$$\ell_r(\hat{k}_{\downarrow}, \hat{k}_{\uparrow}) = \frac{p(\hat{n}_{\mathrm{m}}) P(\hat{k}_{\downarrow}, \hat{k}_{\uparrow}, \hat{n}_{\mathrm{m}}) F(\mu(\hat{k}, \hat{n}_{\mathrm{m}}))}{4\mu(\hat{k}_{\downarrow}, \hat{n}_{\mathrm{m}})\mu(\hat{k}_{\uparrow}, \hat{n}_{\mathrm{m}})\langle\mu(\hat{n}_{\mathrm{r}}, \hat{n}_{\mathrm{m}}) P(\hat{n}_{\mathrm{r}}, \hat{n}_{\mathrm{m}})\rangle}. \tag{3.23}$$

Eq. 3.23 for the BRDF also holds if the individual microfacets have different sizes, as long as the size

---

microfacet orientations have to be considered as independent from each other.

distribution is not correlated with the distribution of the microfacets' normals.

3.4.1 Shadowing Term

With a given distribution of the microfacets' normals, the only expressions that are not straightfor-ward to compute are the shadowing terms $P(\hat{k}_\downarrow, \hat{k}_\uparrow, \hat{n}_\mathrm{m})$ and $P(\hat{n}_\mathrm{r}, \hat{n}_\mathrm{m})$, respectively. The probability $P(\hat{k}_\downarrow, \hat{k}_\uparrow, \hat{n}_\mathrm{m})$ that a given microfacet is neither shadowed nor masked for a particular set of incidence and reflection directions equals the product of the probability $P(\hat{k}_\downarrow, \hat{n}_\mathrm{m})$ that the microfacet is visible from the incidence direction and the probability $P(\hat{k}_\uparrow, \hat{n}_\mathrm{m} \,|\, \hat{k}_\downarrow)$ that the same microfacet is visible from the reflection direction under the condition of not being shadowed from the direction $\hat{k}_\downarrow$. In general the conditional probability is unequal to the unconditional one $P(\hat{k}_\uparrow, \hat{n}_\mathrm{m} \,|\, \hat{k}_\downarrow) \neq P(\hat{k}_\uparrow, \hat{n}_\mathrm{m})$, which means that visibility of incoming and outgoing directions in fact are correlated. This can be seen easily in the extreme case where $\hat{k}_\downarrow = \hat{k}_\uparrow$ and hence $P(\hat{k}_\uparrow, \hat{n}_\mathrm{m} \,|\, \hat{k}_\downarrow) = 1$. More generally it is obvious that the correlation between the incoming and outgoing directions is higher the smaller the angle between both directions is. Hence van Ginneken et al. (1998), proposed a shadowing term of the form

$$P(\hat{k}_\downarrow, \hat{k}_\uparrow, \hat{n}_\mathrm{m}) = (1 - t(\gamma)) P(\hat{k}_\downarrow, \hat{n}_\mathrm{m}) P(\hat{k}_\uparrow, \hat{n}_\mathrm{m}) + t(\gamma) \min(P(\hat{k}_\downarrow, \hat{n}_\mathrm{m}) P(\hat{k}_\uparrow, \hat{n}_\mathrm{m})) \qquad (3.24)$$

where $-\pi < \gamma < \pi$ is the angle between the projection of $\hat{k}_\downarrow$ and $\hat{k}_\uparrow$ onto the reference plane and $0 < t(\gamma) < 1$ is a correlation factor. This shadowing term is composed of two parts whose weights are controlled by a correlation term accounting for the reflection angle by damping the probability for smaller angles. While van Ginneken et al. (1998) could show that energy conservation is fulfilled for arbitrary runs of $t(\gamma)$ sensible forms of $t(\gamma)$ should fulfill $t(0) = 1$ and decrease monotonically to almost zero as $|\gamma|$ increases (van Ginneken et al., 1998). Moreover van Ginneken et al. (1998) found the range of correlation effects to be of the order $15\,°$ and, hence, a Gaussian with standard deviation of $15\,° \equiv \pi/12$ is used in this model

$$t(\gamma) = \sqrt{\frac{72}{\pi^3}} \exp\left(-\frac{72\gamma^2}{\pi^2}\right). \qquad (3.25)$$

All that is needed now is an expression for the probability $P(\hat{k}, \hat{n}_\mathrm{m})$ that a microfacet with normal $\hat{n}_\mathrm{m}$ is visible from a given direction $\hat{k}$ as the probabilities $P(\hat{k}_\uparrow, \hat{n}_\mathrm{m})$, $P(\hat{k}_\downarrow, \hat{n}_\mathrm{m})$ and $P(\hat{n}_\mathrm{r}, \hat{n}_\mathrm{m})$ are just special cases of $P(\hat{k}, \hat{n}_\mathrm{m})$. The key assumption we make here is that this probability is independent from the microfacet's normal $\hat{n}_\mathrm{m}$ as long as it is not turned away from the reference plane (self-shadowing), i.e.

$$P(\hat{k}, \hat{n}_\mathrm{m}) = \begin{cases} P(\hat{k}) & \text{if } \mu(\hat{k}, \hat{n}_\mathrm{m}) > 0 \\ 0 & \text{otherwise.} \end{cases} \qquad (3.26)$$

Basically, this assumes the visibility of an individual microfacet to be uncorrelated with its orientation which is more likely, the rougher the surface is, and fails, if certain orientations are more likely to be found at certain heights. As this conjecture is perfectly valid for all surface textures under consideration (e.g., ice, deserts → sand, forests → leaves) the visibility probability will be treated as independent from its microfacet orientation henceforth.

Using the latter result for the visibility probability in combination with eq. (3.19 – 3.21) the projected area of the surface element under consideration in the direction $\hat{k}$ may be written as

$$\sigma\mu(\hat{k},\hat{n}_\mathrm{r}) = \sum_{\mathrm{facets}} \sigma_\mathrm{m}\mu(\hat{k},\hat{n}_\mathrm{m})_+ P(\hat{k}) \tag{3.27}$$

$$= N\sigma_\mathrm{m}P(\hat{k}) \int_{\Omega_+(\hat{k})} \mu(\hat{k},\hat{n}_\mathrm{m})\,p(\hat{n}_\mathrm{m})\,\mathrm{d}\Omega_{\hat{n}_\mathrm{m}} \tag{3.28}$$

$$= N\sigma_\mathrm{m}P(\hat{k})\langle\mu(\hat{k},\hat{n}_\mathrm{m})_+\rangle \tag{3.29}$$

$$= N\sigma_\mathrm{m}P(\hat{k})g(\hat{k}) \tag{3.30}$$

where the '+' subscript in Eq. 3.27 refers to the fact that the summation is done over microfacets oriented towards $\hat{k}$, in Eq. 3.28 that the integration is done over the positive hemisphere with respect to $\hat{k}$ and in Eq. 3.29 that the averaging is done over the part of the distribution with microfacets' normals oriented towards $\hat{k}$, respectively. In Eq. 3.30 the notation

$$g(\hat{k}) \equiv \langle\mu(\hat{k},\hat{n}_\mathrm{m})_+\rangle = \int_{\Omega_+(\hat{k})} \mu(\hat{k},\hat{n}_\mathrm{m})\,p(\hat{n}_\mathrm{m})\,\mathrm{d}\Omega_{\hat{n}_\mathrm{m}} \tag{3.31}$$

has been introduced as a shorthand for the averaging with respect to the positive hemisphere in the direction $\hat{k}$. As each microfacet that is turned away from the direction $\hat{k}$ i.e., $\mu(\hat{k},\hat{n}_\mathrm{m}) \leq 0$ will cast a shadow of an area $\sigma_\mathrm{m}\mu(\hat{k},\hat{n}_\mathrm{m})$, this area has to be subtracted from the contribution of microfacets' areas turned towards $\hat{k}$

$$N\sigma_\mathrm{m}P(\hat{k})g(\hat{k}) = N\sigma_\mathrm{m}g(\hat{k}) + N\sigma_\mathrm{m}\langle\mu(\hat{k},\hat{n}_\mathrm{m})_-\rangle \tag{3.32}$$

which immediately gives a useful expression for the visibility probability

$$P(\hat{k}) = 1 + \frac{\langle\mu(\hat{k},\hat{n}_\mathrm{m})_-\rangle}{g(\hat{k})}. \tag{3.33}$$

As the numerator of the second term is computed by integration over the negative hemisphere $\Omega_-(\hat{k})$ that is complementary to the positive hemisphere $\Omega_+(\hat{k})$ that is used as the integration volume for the

averaging in the denominator $g(\hat{k})$ it is obvious that

$$-1 \le \frac{\langle \mu(\hat{k}, \hat{n}_\mathrm{m})_- \rangle}{g(\hat{k})} \le 0. \tag{3.34}$$

Moreover any valid distribution of microfacets' normals is characterized by the requirement that the average over all normals should lie in the direction of the reference plane's normal $\hat{n}_\mathrm{r}$ as this actually is the definition of the reference plane:

$$\int\limits_{\Omega_+(\hat{k})} \hat{n}_\mathrm{m} p(\hat{n}_\mathrm{m}) \, \mathrm{d}\Omega \hat{n}_\mathrm{m} + \int\limits_{\Omega_-(\hat{k})} \hat{n}_\mathrm{m} p(\hat{n}_\mathrm{m}) \, \mathrm{d}\Omega \hat{n}_\mathrm{m} = \hat{n}_\mathrm{r} \langle \mu(\hat{n}_\mathrm{r}, \hat{n}_\mathrm{m}) \rangle \tag{3.35}$$

where the term $\langle \mu(\hat{n}_\mathrm{r}, \hat{n}_\mathrm{m}) \rangle$ is just a normalization factor and ensures the proper norm of the expressions on both sides of the equation. If the latter equation is multiplied by $\hat{k}$, we get

$$\langle \mu(\hat{k}, \hat{n}_\mathrm{m})_- \rangle = \mu(\hat{k}, \hat{n}_\mathrm{r}) \langle \mu(\hat{n}_\mathrm{r}, \hat{n}_\mathrm{m}) \rangle - g(\hat{k}). \tag{3.36}$$

Substituting this result in the expression for the visibility probability (Eq. 3.33) gives

$$P(\hat{k}) = \frac{\mu(\hat{k}, \hat{n}_\mathrm{r}) \langle \mu(\hat{n}_\mathrm{r}, \hat{n}_\mathrm{m}) \rangle}{g(\hat{k})} \tag{3.37}$$

which may be used in combination with Eq. 3.24 in Eq. 3.23 to get the final result for the specular component microfacet BRDF that only depends on the actual distribution of microfacets' normals.

$$\ell_r(\hat{k}_\downarrow, \hat{k}_\uparrow) = \tfrac{1}{4} p(\hat{n}_\mathrm{m}) \langle \mu(\hat{n}_\mathrm{r}, \hat{n}_\mathrm{m}) \rangle \frac{F(\mu(\hat{k}, \hat{n}_\mathrm{m}))}{g(\hat{k}_\downarrow) g(\hat{k}_\uparrow)} \tag{3.38}$$

3.4.2 Specular and Diffuse Components

Until now the BRDF has been developed under the assumption that all the microfacets may be considered as small 'mirrors' that reflect or absorb the incident radiation due to their Fresnel coefficients but at a single-bounce event. This is not valid for a realistic BRDF model as this must take multiple bounce and subsurface scattering events into account. Therefore the presented BRDF model for the specular component must be extended by the diffuse component that accounts for these multiple bounce events. The simplest form for the diffuse component is a pure Lambertian reflection term

$$\ell_r(\hat{k}_\downarrow, \hat{k}_\uparrow) = \frac{c_\mathrm{d}}{\pi} \ell_r^\mathrm{d} + c_\mathrm{s} \ell_r^\mathrm{s}(\hat{k}_\downarrow, \hat{k}_\uparrow) \tag{3.39}$$

where the superscripts d and s refer to the diffuse and specular components of the combined BRDF, respectively. The first reflection term $0 \le \ell_r^\mathrm{d} \le 1$ is nothing but the diffuse albedo of the structured surface while the second reflection term $\ell_r^\mathrm{s}(\hat{k}_\downarrow, \hat{k}_\uparrow)$ is the BRDF that has been derived in the previous

section. To fulfill energy conservation one only has to ensure that $c_d + c_s \leq 1$. The problem with this definition is first it is unclear how to choose the weights of the two coefficients c_d and c_s and second, that the coefficients, in principle, have to be angular dependent themselves because if the specular part would reach one for some specific combination of angles the other component must vanish to ensure energy conservation for all angles if the coefficients were angular independent. To address these problems in a way that preserves energy conservation and reciprocity, a method of Shirley, Smits and Lafortune (Shirley et al., 1997) to determine the coefficient of the diffuse component is used in this thesis

$$c_d(\hat{k}_\downarrow, \hat{k}_\uparrow) = c(\ell_r^d - R(\hat{k}_\downarrow))(\ell_r^d - R(\hat{k}_\uparrow)) \tag{3.40}$$

where again ℓ_r^d is the (wavelength dependent) diffuse albedo of the surface and

$$R(\hat{k}) = \int_\Omega \ell_r^s(\hat{k}, \hat{k}')\mu(\hat{k}', \hat{n}_r) \, d\Omega_{\hat{k}'} \tag{3.41}$$

is the directional hemispherical reflectance of the specular component where $\hat{k}'$ is the mirrored direction of $\hat{k}$. To also drop the coefficient of the specular component as well, all we have to do is to absorb that coefficient in the normalization constant c of the diffuse component and to ensure (by virtue of this normalization constant) that the total amount of reflected intensity—when integrated over all solid angles—equals the total amount of incident intensities weighted by the surface element's wavelength dependent albedo ℓ_r^d. This yields a form of the BRDF that combines the diffuse and specular component and introduces the wavelength dependence of the BRDF by the normalization constant c that ensures the total ratio of reflected and incident irradiation to be determined by the diffuse albedo ℓ_r^d.

$$\ell_r(\hat{k}_\downarrow, \hat{k}_\uparrow) = c(\ell_r^d - R(\hat{k}_\downarrow))(\ell_r^d - R(\hat{k}_\uparrow))\ell_r^d + \ell_r^s(\hat{k}_\downarrow, \hat{k}_\uparrow). \tag{3.42}$$

3.4.3 Implementation Details

With a given microfacets' normal distribution, the BRDF presented in the latter section is straightforward to compute. The first two terms in the specular BRDF component eq. (3.38) are independent from the actual incoming and outgoing direction under consideration and may be globally pre-evaluated for a given distribution to save computational effort. The Fresnel coefficient is approximated using Schlick's approximation formula also commonly used in 3D computer visualization regimes Schlick (1994)

$$F(\mu(\hat{k}, \hat{n}_m)) = \ell_r^d + (1 - \ell_r^d)(1 - \mu(\hat{k}, \hat{n}_m))^5 \tag{3.43}$$

where again ℓ_r^d is the diffuse albedo. This approximation massively speeds up the computation without introducing problems or errors as the difference between the approximation formula and the full Fresnel expression can be shown to be less than one percent (Schlick, 1994).

The integration for the $g(\hat{k})$ and $R(\hat{k})$ term is done using a simple Monte Carlo integration. For a given distribution, the corresponding values are pre-computed as well on a close-meshed grid of $360 \times 91 = 32\,760$ grid points where eleven sets of $R(\hat{k})$ are computed for $\ell_r^{\mathrm{d}} \in \{0, 0.1, \ldots, 1\}$, respectively. Values of $R(\hat{k})$ for arbitrary values of ℓ_r^{d} are then computed using linear interpolation. For a given texture, i.e. distribution of the microfacets' normals, the computation of the BRDF for some combination of wavelength λ, incidence direction $\hat{k}_{\downarrow}$ and reflection direction $\hat{k}_{\uparrow}$ is done as follows

1. The first term of the specular component of the BRDF, namely $\frac{1}{4} p(\hat{n}_{\mathrm{m}}) \langle \mu(\hat{n}_{\mathrm{r}}, \hat{n}_{\mathrm{m}}) \rangle$ is computed globally using the given distribution $p(\hat{n}_{\mathrm{m}})$.

2. $g(\hat{k})$ is computed using a Monte Carlo integration routine with respect to the given distribution $p(\hat{n}_{\mathrm{m}})$ for both, incidence and reflection direction on a close-meshed grid of $32\,760$ grid points.

3. The wavelength dependent diffuse albedo $\ell_r^{\mathrm{d}}(\lambda)$ of the texture under consideration is read from an input file[4]

4. The Fresnel coefficients are calculated for the reflection angles $\mu(\hat{k}, \hat{n}_{\mathrm{r}}) \in \{0, 0.05, \ldots, 1\}$ and the diffuse albedos $\ell_r^{\mathrm{d}} \in \{0, 0.1, \ldots, 1\}$ resulting in a grid of 231 grid points.

5. The specular component of the BRDF ℓ_r^{s} is computed as eleven grids each of $32\,760$ grid points for the diffuse albedos $\ell_r^{\mathrm{d}} \in \{0, 0.1, \ldots, 1\}$.

6. The diffuse to specular component weight $R(\hat{k})$ is computed for each of the eleven specular components.

7. All components calculated so far are used for the final specular-diffuse BRDF using quadratic interpolation.

All values are tabulated giving the BRDF $\ell_r(\ell_r^{\mathrm{d}}, \hat{k}_{\downarrow}, \hat{k}_{\uparrow})$ on a grid of $11 \times 32\,760 = 360\,360$ grid points. Together with the input file of $\ell_r^{\mathrm{d}}(\lambda)$ the BRDF $\ell_r(\lambda, \hat{k}_{\downarrow}, \hat{k}_{\uparrow})$ is computed using quadratic interpolation. The equidistant sampling of μ (step 4) causes a relative oversampling of the corresponding reflection angle in the domain of $\arccos \mu \sim \pi/2$ which is quite useful as it can easily be shown that each microfacet distribution that is centered around $\theta = 0$ leads to a distribution of reflection angles centered around $\pi/2$ when integrating the microfacet distribution over the irradiated day side hemisphere of the planet. Hence this relative oversampling accounts for the center of the reflection angle distribution of a planet illuminated by an infinite distant host star. Although the reflection angle distribution center shifts towards larger angles for finite distant host stars, the shift is small as compared to the domain of oversampling and may be ignored in this context.

Until now only the distribution of the microfacet normals with respect to the reference plane's normal has been described but not the orientation of the reference plane itself. As the reference plane

---

[4]input files may be found at `$PHX_SURFACE/textures/<#>/albedo.dat` where `<#>` refers to the number of the texture to be used.

can be thought of as the low detail surface structure of the planet under consideration it is internally represented as surface polygon mesh based on the planets topography map used for the `PUMA` model as well. As the surface topography map is specified in terms of geopotential W it is first converted into a height field map before the surface polygon mesh is created. With the surface polygon mesh of the planet's topography map the surface normal, i.e., the normal of the BSSRDF's reference plane, is calculated as the vector product of the polygon's contacting edge vectors. If the polygon is described by the position vectors $\boldsymbol{r}_i$ specifying the individual vertices of the polygon the normal vector $\hat{n}_{\mathrm{r}}$ is calculated as

$$\hat{n}_{\mathrm{r}} = \operatorname{sgn} \mathcal{O} \left[(\boldsymbol{r}_2 - \boldsymbol{r}_1) \times (\boldsymbol{r}_3 - \boldsymbol{r}_1) \right] \tag{3.44}$$

where $\mathcal{O}$ is defined to be $+1$ if the vector created by the vector product is oriented outwards i.e. not enclosed by the polygon mesh and -1 otherwise. This definition ensures the reference plane's normal to have the right orientation.

3.4.4 OpenGL Acceleration

Because of the high computational effort which is needed to compute the polygon mesh itself, the surface normals $\hat{n}_{\mathrm{r}}$ and the BRDF reflection and absorption properties as described in the latter sections, the whole formalism is implemented in the OpenGL Shading Language GLSL that may outsource the whole computation pipeline to GPUs (if available) in order to limit the CPU load and in that account for the fact that the `PHOENIX 3DRT` model itself needs as much computational power as available. As the BRDF is entirely written in GLSL and may be compiled individually and linked to the `PHOENIX 3DRT` core module, it is called a (OpenGL) shader in OpenGL usage.

Calculations of reflection models is one the key concepts of the OpenGL language even though for the purpose of computer graphics in most applications. Nevertheless the same routines that are used to calculate eye-catching computer graphics can be used to implement BRDF models that are based on physical principles as described above. All the polygon mesh calculations can easily be performed as these meshes are used in 3D computer graphics as well, and the corresponding reflection calculations are parallelized on the GPUs that are constructed especially for these kind of calculations whereby the underlying OpenGL implementation abstracts away the manual effort of parallelization to a large extent (McCool et al., 2001).

GPU calculations can only be performed if the corresponding hardware is available, of course. As the `PHOENIX 3DRT` usually runs on high performance cluster computer centers it is unclear if the GPU hardware is always available and accessible. Hence all implemented code has been tested to be compilable with the *Low Level Virtual Machine* (LLVM) compiler infrastructure. The *Low Level Virtual Machine Just In Time* (LLVM JIT) compiler can determine the local system properties of the executing system and compiles additional procedures that run on the CPUs and emulate instructions that cannot be performed by the GPU. This technique is also used in many modern OpenGL applications.
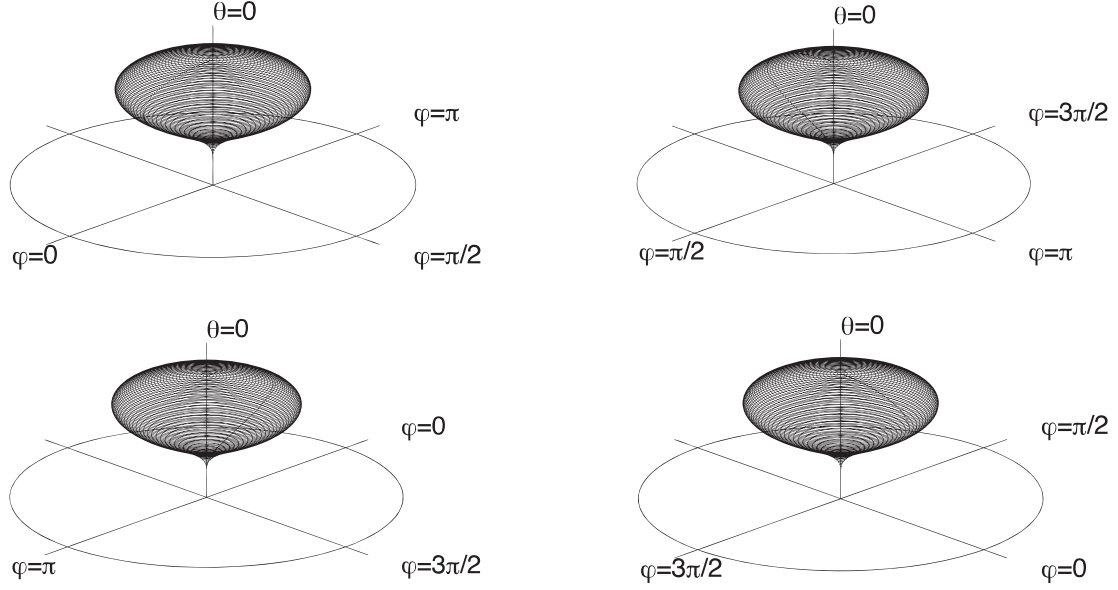
Figure 3.4. Distribution of microfacet normals with roughness factor $s = \pi/2$, anisotropy factor $\beta = 1$ and rotational factor $\varphi_r = 0$. Plots are rotated by 90° around $\theta = 0$ axis each time from top left to bottom right.

3.4.5 Microfacets' Normals Distribution

Until now all statements about the BRDF have been very general with respect to a specific surface structure (ice, water, sand, forest etc.). Hence we now draw attention to the individual surface properties of a specific texture. As the wavelength dependence is encoded in the diffuse albedo of the combined BRDF (3.42) the angular dependency arises from the microfacets' normal distribution $p(\hat{n}_{\mathrm{m}})$. As we may assume the microfacets' orientations to be more or less normally distributed a 2D Gaussian is used for the probability density function

$$p(\theta, \varphi) = c \exp\left[-\tan^2\theta\left(\frac{\cos^2(\varphi - \varphi_r)}{s^2} + \beta^2\frac{\sin^2(\varphi - \varphi_r)}{s^2}\right)\right] \tag{3.45}$$

where θ is the angle between the microfacet's normal and the reference plane's normal and φ the azimuth angle of the microfacet's normal. While c is just a normalization constant, the parameters s, β and φ_r control the shape of the normals' probability distribution and in that the characteristics of the surface texture to be modeled: The parameter s can be thought of as the distributions standard deviation and in that controls the concentration of normals around the zenith angle or—in terms of texture properties—the roughness of the surface. As large values of s correspond to a wide spread of normals with respect to the zenith angle, s is referred to as *roughness factor*. The parameter β is a weighting factor that controls the relative roughness of the texture in the $\varphi = \pi$ direction with respect to the perpendicular $\varphi = \pi/2$ direction and hence causes a symmetry break with respect to the azimuth angle for $\beta \neq 1$. This can easily be seen as the φ dependence vanishes in the case of $\beta = 1$ and the distribution becomes isotropic with respect to φ. Hence the parameter β is referred to

Figure 3.5. Distribution of microfacet normals with roughness factor $s = 3\pi/2$, anisotropy factor $\beta = 1$ and rotational factor $\varphi_r = 0$. Plots are rotated by $90°$ around $\theta = 0$ axis each time from top left to bottom right.

Figure 3.6. Distribution of microfacet normals with roughness factor $s = 3\pi/2$, anisotropy factor $\beta = 5$ and rotational factor $\varphi_r = 0$. Plots are rotated by $90°$ around $\theta = 0$ axis each time from top left to bottom right.
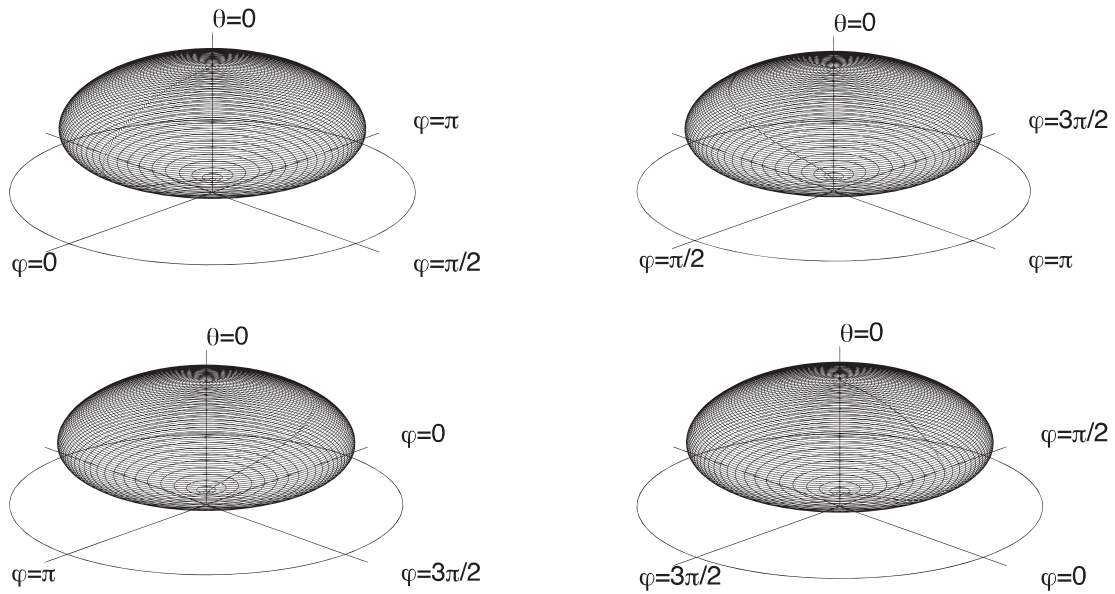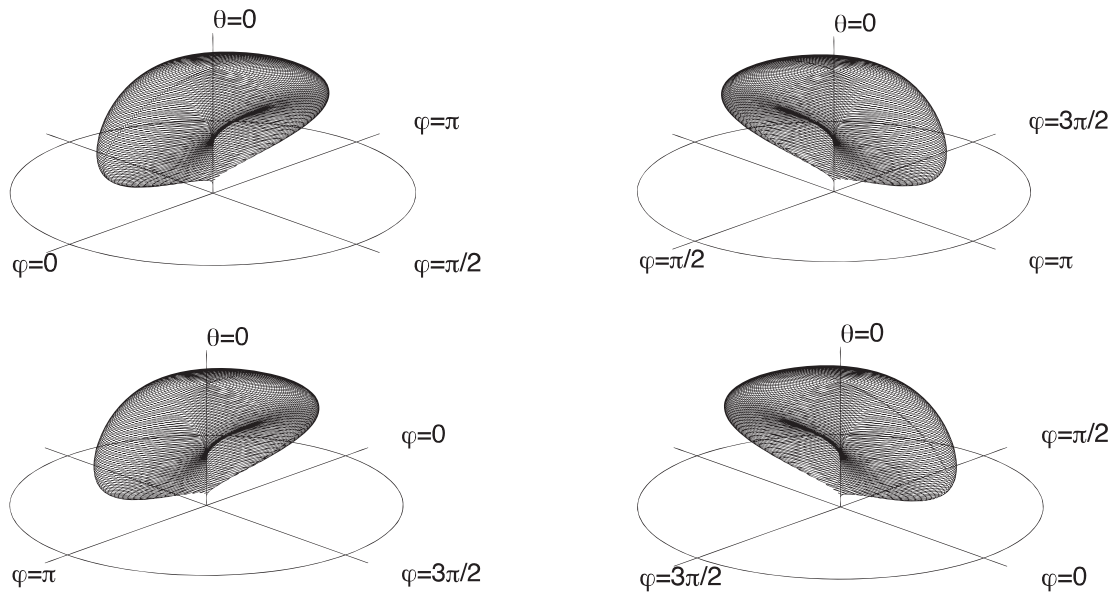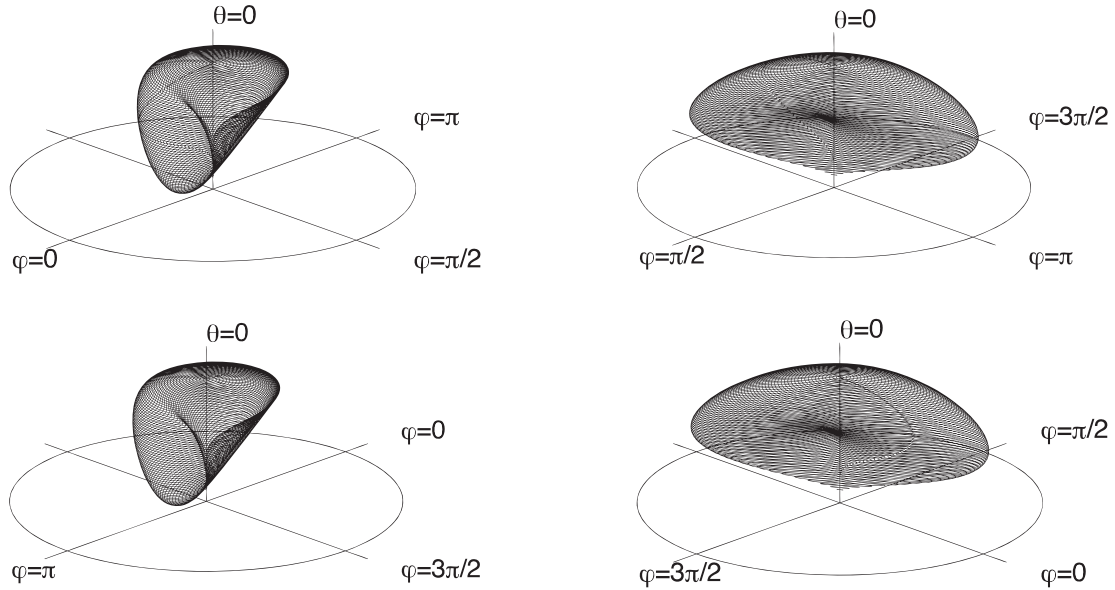
Figure 3.7. Distribution of microfacet normals with roughness factor $s = 3\pi/2$, anisotropy factor $\beta = 5$ and rotational factor $\varphi_r = \pi/6$. Plots are rotated by 90° around $\theta = 0$ axis each time from top left to bottom right.

as *anisotropy factor*. The parameter φ_r is a simple shifting factor that rotates the distribution around the $\theta = 0$ axis and with that φ_r is referred to as *rotation factor*.

3.4.6 Parameter Calibration

To develop individual surface textures out of the presented parameterized BRDF model for e.g., sand, water, forest the *Moderate Resolution Imaging Spectroradiometer* MODIS NASA data is used to optimize the model parameters for the individual textures. MODIS consists of two instruments, both are part of the NASA *Earth Observing System* (EOS) project aboard the Terra (EOS AM) and Aqua (EOS PM) satellites, respectively, observing the entire Earth's surface every 24h to 48h acquiring data in 36 spectral bands (cf. tab. A.1, A.2) from $405\,\text{nm}$ to $14.385\,\mu\text{m}$ and at three spacial resolutions: $250\,\text{m}$, $500\,\text{m}$ and $1000\,\text{m}$.

Among the various data products[5] of the MODIS project, two data products are used for the purpose of parameter optimization with respect to the described model: the MODIS Land Cover data product (MOD12-Q1) and the Surface Reflectance BRDF/Albedo Parameter data product (MOD43). The Land Cover data product contains land cover type and land cover change parameters, which is produced at $1\,\text{km}$ resolution and identifies 17 different classes of land cover types following the *International Geosphere-Biosphere Programme* (IGBP) global vegetation database, which defines nine classes of natural vegetation, three classes of developed lands, two classes of mosaic lands, and three classes of nonvegetated lands (snow/ice, bare soil/rocks, water) (Moreira et al., 2006). Out of these

---

[5]The term *data product* is used by the MODIS project and refers to a coherent set of data, intended to be used for a specific purpose like determining the BRDF for various land cover classes.

17 land cover classes (textures) four classes have been chosen with an eye toward the Mars modeling which is described below: *Water* (class 0) for reference purposes as it is the best data set with respect of data quality due to the large fraction of earth surface coverage, *Mixed Forest* (class 5) since this is a good example class representing a complex structured surface to test the BRDF model flexibility, *Savannas/Non-vegetated* (class 9) as the best classification for sand textures/deserts which are very prominent on Mars as well as *Snow and Ice* (class 15) to model ice covered regions.

The Surface Reflectance BRDF/Albedo Parameter data product contains BRDF values for the wavelength bands 1 to 7 (cf. tab. A.1) as well as for the three broad bands ($0.3\,\mu m$–$0.7\,\mu m$, $0.7\,\mu m$–$5.0\,\mu m$, and $0.3\,\mu m$–$5.0\,\mu m$). The BRDF is obtained by fitting a semi-empirical kernel-driven Ross-Li BRDF model Lucht et al. (2000) to the MODIS measurements

$$f_r = f_{\text{iso}}(\lambda) + f_{\text{vol}}(\lambda)K_{\text{vol}}(\theta_\downarrow, \varphi_\downarrow \; ; \; \theta_\uparrow, \varphi_\uparrow) + f_{\text{geo}}(\lambda)K_{\text{geo}}(\theta_\downarrow, \varphi_\downarrow \; ; \; \theta_\uparrow, \varphi_\uparrow) \tag{3.46}$$

where the different parameters f represent the magnitude of isotropic, volumetric and geometric scattering and are found by fitting to kernels K expressing the geometric nature of that scattering. As mentioned above the semi-empirical BRDF model is optimized for the purpose of describing and reproducing measured data while simultaneously being easy to handle. This is actually a slightly different focus as compared to the BRDF model derived above as this model tries to be easy to handle as well but accepts minor accuracy for a particular surface texture for the benefit of being more flexible in terms of adaptability to other surface textures if no measurements are available as all parameters represent meaningful properties from a physical point of view.

The fitting of the BRDF is done using the least-squares fitting method. The MODIS BRDF/Albedo Science data products are provided in a sinusoidal grid projection with standard tiles representing $10° \times 10°$ (2400×2400 px) on the Earth Wolfe et al. (1998). For each surface texture a grid point of $10° \times 10°$ has been chosen that best represents the particular surface texture with more than 95% of the 2400×2400 px $\approx 5.76 \times 10^6$ px corresponding to the land cover class under consideration. For each individual pixel the parameters of the BRDF model have been adjusted using the least square deviation for all $18 \times 72 = 1296$ ($\theta = 0°, 5°, \ldots, 85°$; $\varphi = 0°, 5°, \ldots, 355°$) incidence and reflection directions ($1296^2 \approx 1.68 \times 10^6$ [data points]).

The free parameters to be adjusted are *roughness factor s*, *anisotropy factor β*, *rotational factor φ_r* and *diffuse albedo f_r^{d}*. Whereas the first three parameters are angular dependent and wavelength independent, the latter parameter is angular independent and wavelength dependent. Hence only the first three parameters are fitted in this first step using a normalization factor for both the MODIS BRDF and the model BRDF to be fitted, to ensure independence of the diffuse albedo, which can be thought of as constant for a given wavelength. The fit is calculated in the MODIS 1 wavelength band ($620\,\text{nm} \leq \lambda \leq 670\,\text{nm}$).

In a second step the angular dependent parameters are held constant while the angular independent diffuse albedo is fitted to the semi-empirical BRDF model. As mentioned above the MODIS albedo data is available for the wavelength bands 1 to 7. Again the diffuse albedo is fitted using the least-

Figure 3.8. Fit of the water surface texture. The three individual plots show a (normalized) histogram of the s-, β- and φ-parameter distribution when fitting the model BRDF for all $2400 \times 2400\,\mathrm{px}$. The roughness-factor $s = 0.271 \pm 0.05$ states that the surface is moderate smooth while the anisotropy parameter $\beta = 0.988 \pm 0.13$ shows the texture to be or very isotropic. That also explains the fit of the rotation parameter $\varphi_{\mathrm{r}} = 3.776 \pm 3.14$: Because of the isotropy any rotation parameter fits the model equally well.
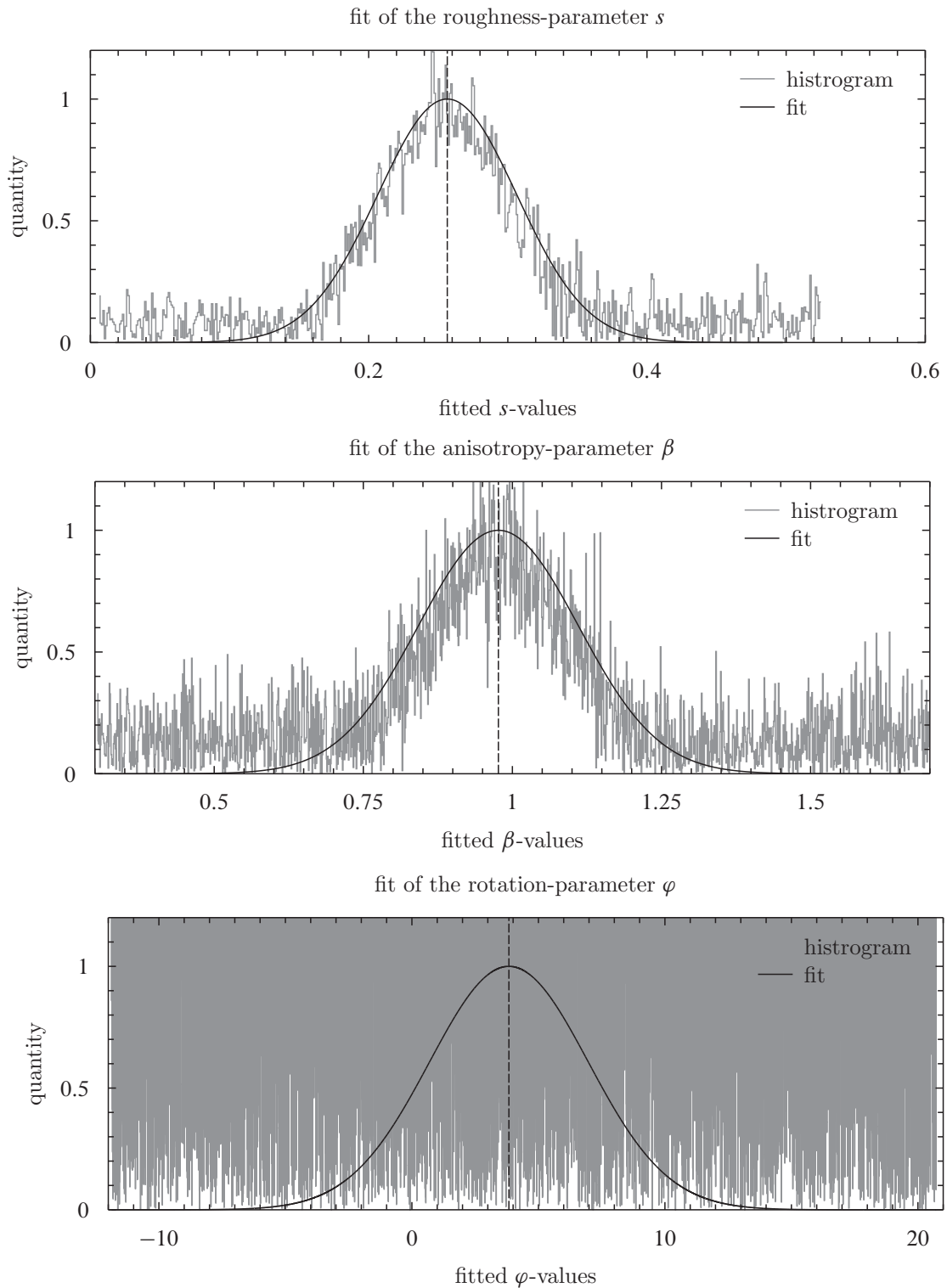
Figure 3.9. Fit of the water surface texture. The three individual plots show a (normalized) histogram of the s-, β- and φ-parameter distribution when fitting the model BRDF for all 2400×2400 px. The roughness-factor $s = 0.103 \pm 0.01$ states that the surface is quite smooth, as expected while the anisotropy parameter $\beta = 1.060 \pm 0.18$ shows the texture to be or more or less isotropic. That also explains the fit of the rotation parameter $\varphi_r = 3.831 \pm 2.854$: Because of the isotropy any rotation parameter fits the model equally well.
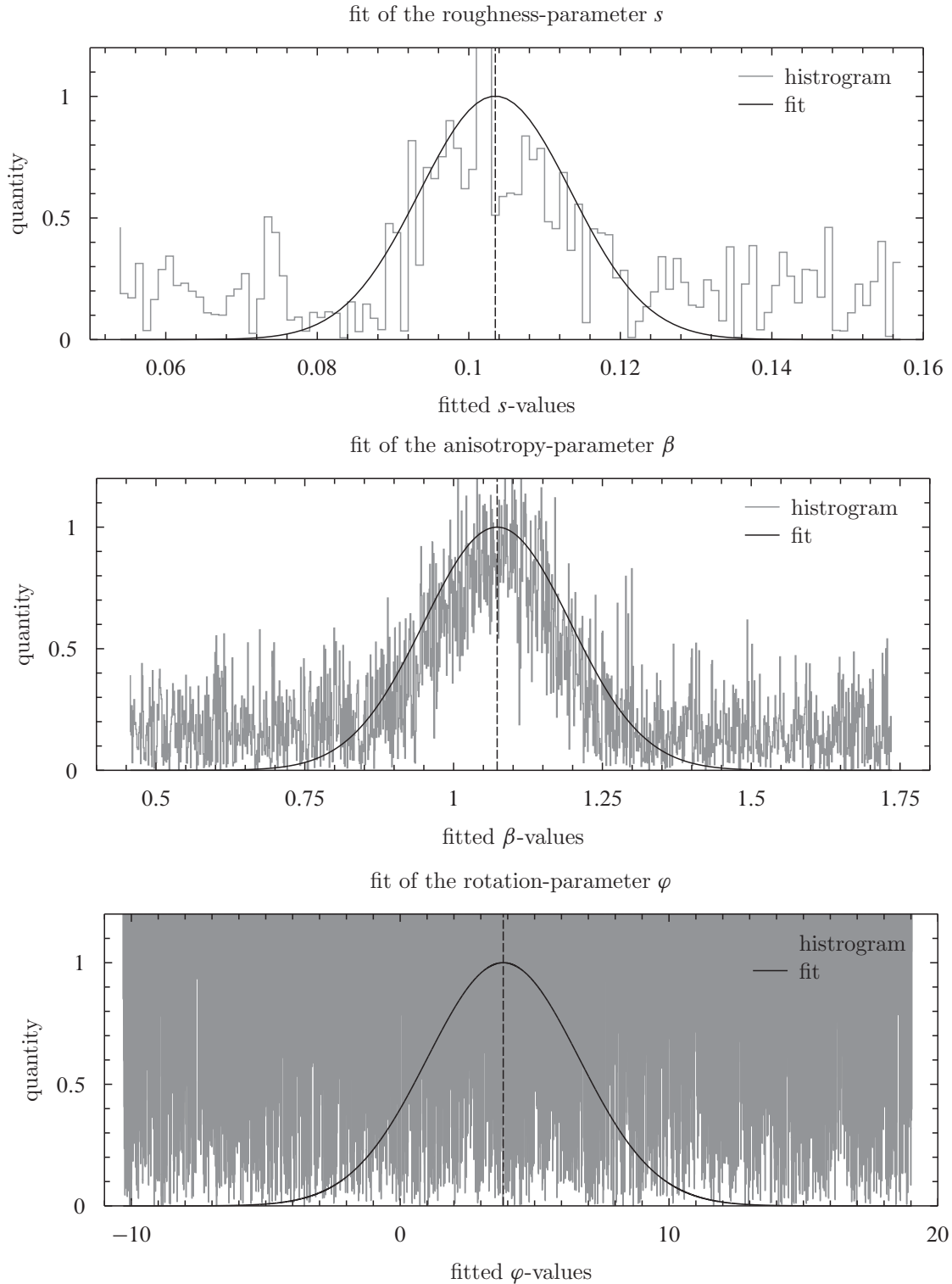
49

fit of the roughness-parameter *s*

fit of the anisotropy-parameter β

fit of the rotation-parameter φ
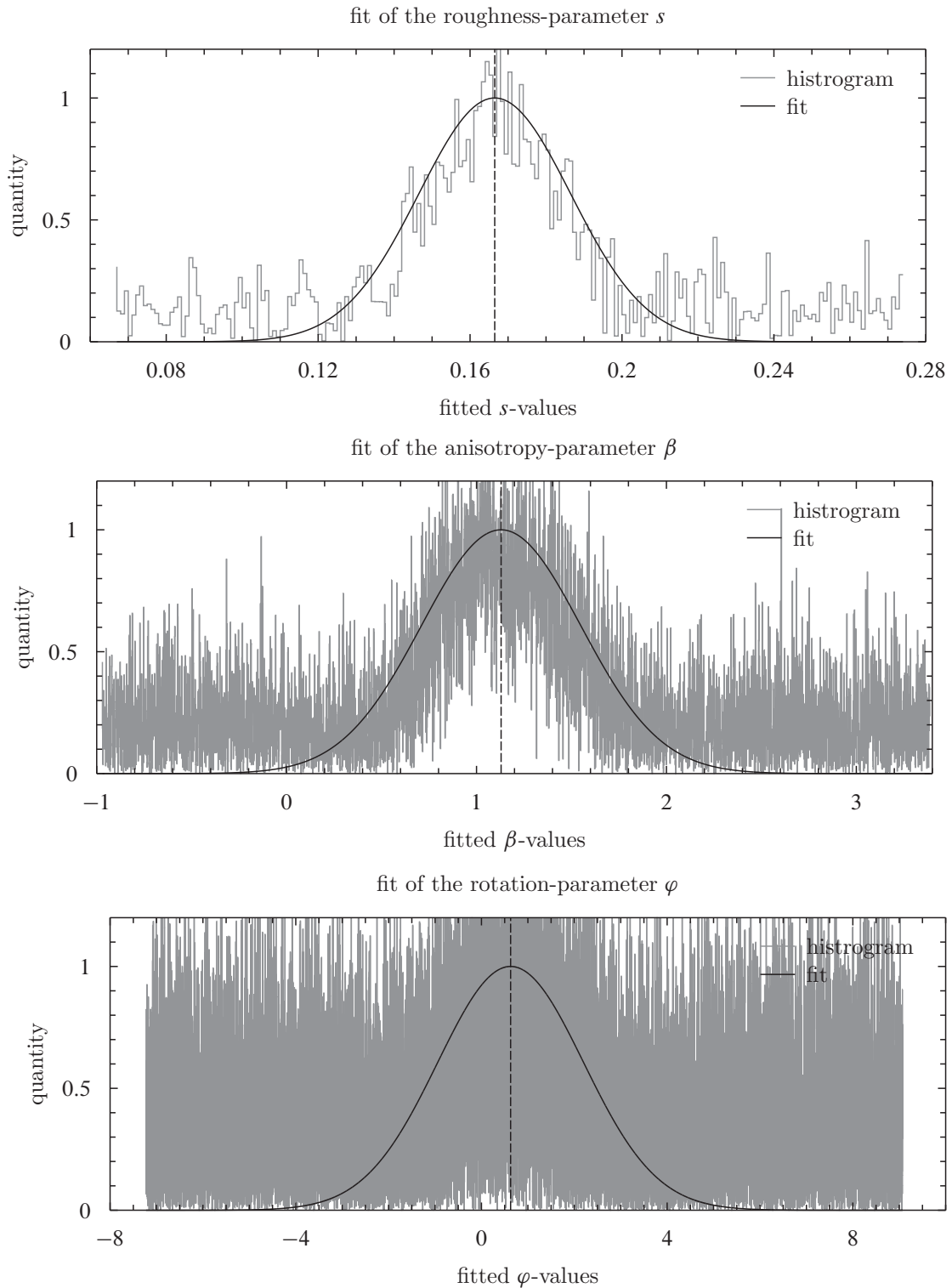
Figure 3.10. Fit of the ice surface texture. The roughness-factor $s = 0.166 \pm 0.02$ states that the surface is quite smooth (between sand and water) while the anisotropy parameter $\beta = 1.132 \pm 0.42$ shows a minor anisotropy although perfect isotropy lies within one standard-deviation. The rotation parameter $\varphi_r = 0.628 \pm 1.57$ shows a clear accumulation and is not distributed as uniform as seen in the case of water and sand.
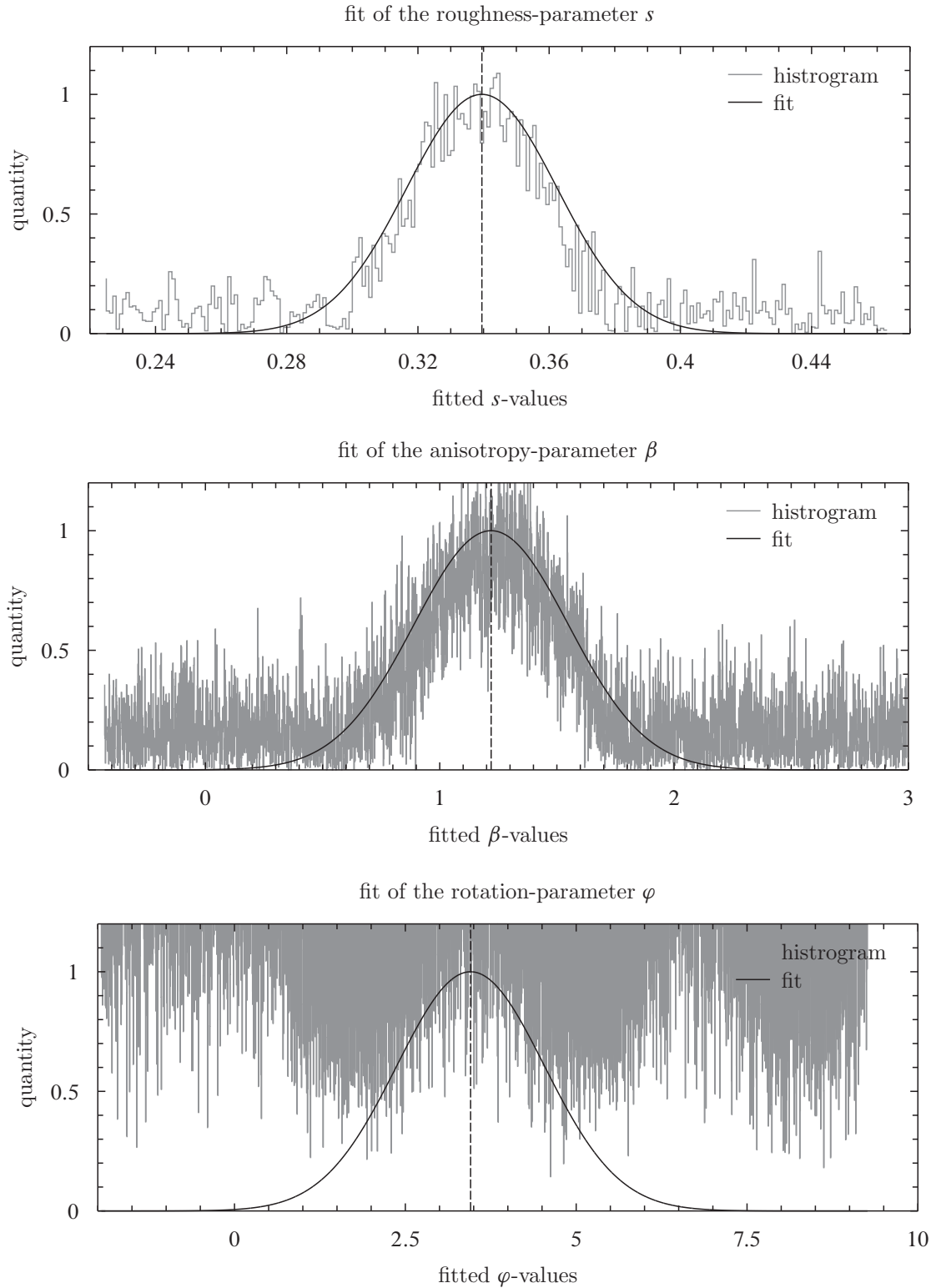
Figure 3.11. Fit of the ice forest texture. The roughness-factor $s = 0.339 \pm 0.03$ states that the surface is less smooth as in the latter cases while the anisotropy parameter $\beta = 1.220 \pm 0.33$ shows a distinct anisotropy although again perfect isotropy lies within one standard-deviation. The rotation parameter $\varphi_r = 3.454 \pm 1.08$ shows a clear accumulation with a periodicity of π as expected in the case of anisotropy.
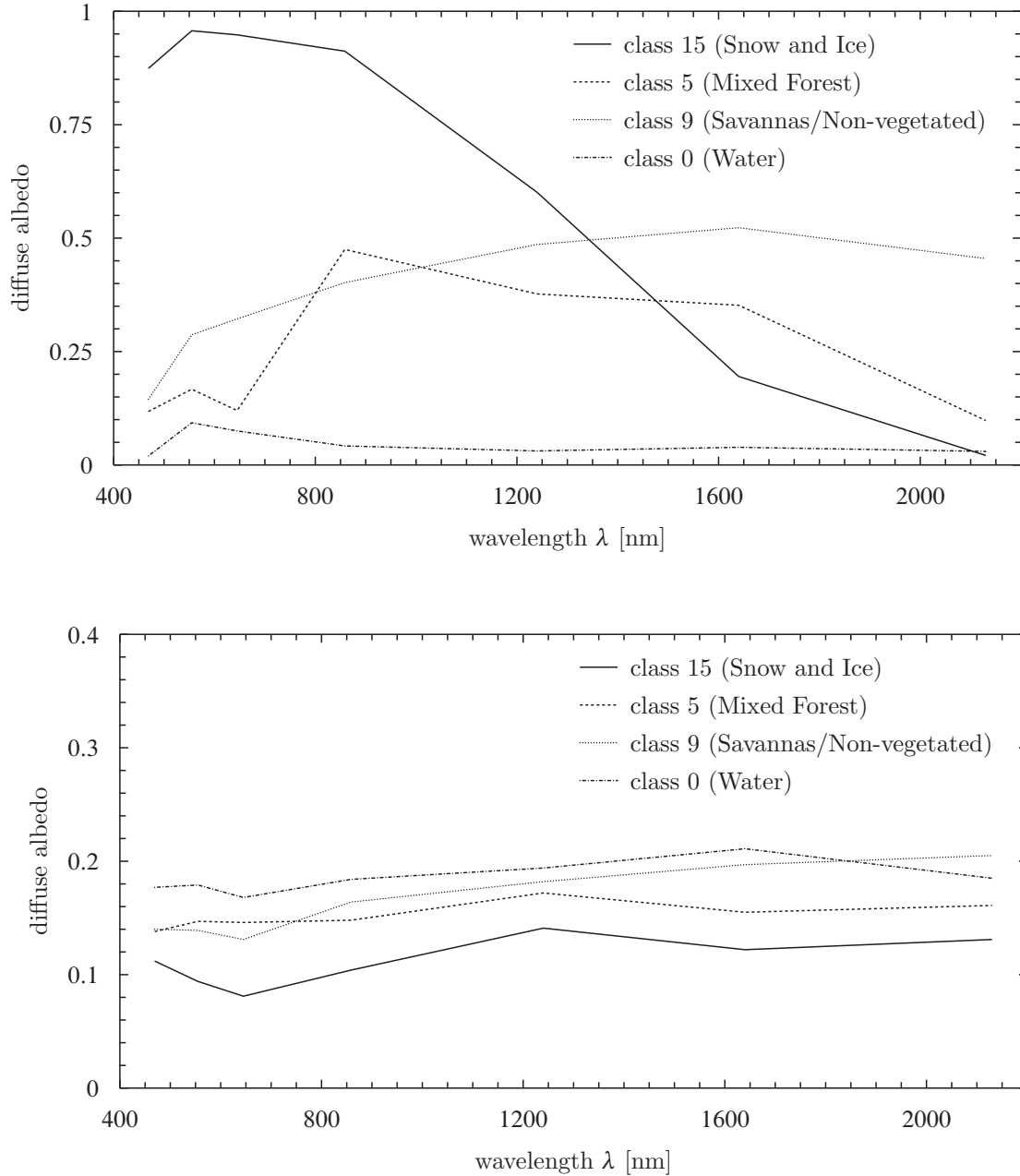
Figure 3.12. Fit of the diffuse albedo parameter for the seven MODIS wavelength bands 1 to 7 (top) and average relative deviation the developed BRDF model and the semi-empirical reference BRDF model is calculated for the remaining six wavelength bands 2 to 7 with fixed model parameters (bottom). The average relative deviation is always between 10% and 20% and does not change dramatically in the different wavelength bands. This shows that the derived BRDF model is flexible enough to realistically represent the observed reflectance data.

squares fitting method for each of the seven wavelength bands.

Finally, a consistency check is performed where the average relative deviation of the developed BRDF model and the semi-empirical reference BRDF model is calculated for the remaining six wavelength bands 2 to 7 with fixed model parameters. The test shows that the average relative deviation of the two models is less than 20% for nearly all textures in all wavelength bands even though the parameters are optimized for the MODIS 1 wavelength band only. Furthermore, it should be noted that the deviation is not increasing monotonically when moving away from the MODIS 1 wavelength band—e.g., the deviation of the mixed forest texture is less in the MODIS 3 band although optimized in the MODIS 1 band—and the general deviation slope is small enough to achieve reliable data for a wide spectral range.

4. Climate Dynamics Theory

This section intends to describe the basic concepts of climate dynamics as needed to understand the `PUMA/Plasim` extension of the `PHOENIX` modeling framework. It cannot and is not intended to replace a complete theoretical description of climate dynamics calculations but should just be thought of as a compilation of the key concepts of the modeling code to be able to evaluate the modeling framework's capabilities and limits.

As already mentioned, the climate dynamics calculations are based on the so-called *Planet Simulator* (`Plasim`) which itself uses the *Portable University Model of the Atmosphere* (PUMA) as a simplified three-dimensional global *General Circulation Model* (GCM) for the dynamic core, both developed by the Theoretical Meteorology at the Meteorological Institute of the University of Hamburg (Lunkeit et al., 2011). `PUMA` is based on the multi-level spectral *Simple Global Circulation Model* (SGCM) described by Hoskins and Simmons (1975) and James and Gray (1986). As a spectral model, the corresponding equations are solved in Fourier space by expanding the dependent variables in terms of a finite series of smooth orthogonal functions. Although `PUMA` originates from the Simmons and Hoskins SGCM version, it has been completely rewritten in portable FORTRAN-90 code, which removes any problems associated with machine-specific properties like word lengths, floating point precision, output, etc. `PUMA` is a stand alone program which does not use any external libraries. All necessary routines are in the source code, even the *Fast Fourier Transform* (FFT) and the matrix inversion (Lunkeit et al., 2011), which makes it beneficial in terms of merging the `PUMA` and `PHOENIX` frameworks. The dynamic core is the heart of every GCM, it is the part that deals with the solutions of the dry, adiabatic primitive equations. The dynamical core solves the primitive equations numerically on a global scale (Polvani et al., 2004).

4.1 Model Approximations

The governing equations used in numerical model calculations to describe a real fluid like a planet's atmosphere, are the Navier-Stokes equations (Phillips, 1956) which are based on the conservation of momentum and mass and hence, extend the classical Euler equations by inner friction and viscosity. These equations are supplemented by the conservation of heat, given by the first law of thermodynamics and an equation of state, representing the physical-chemical properties of the atmosphere. However, these equations support a lot of critical features, such as fast acoustic modes and involve nonlinearities in many terms that makes solving them both, difficult and expensive with respect to the

computational effort as well as particularly ill suited for long time scale calculations (Lunkeit et al., 2011). Hence, some adjustments and simplifications are applied for the sake of modeling atmospheric flow dynamics in global circulation models (Adcroft et al., 2004). These simplifications are necessary to make climate dynamics manageable and commonly used in atmospheric modeling codes as well as the PUMA framework. Therefore, these adjustments, with the corresponding limitations in terms of model capabilities, have to be discussed below, as they have originally been derived for atmospheric calculations on earth conditions which might be quite different from the conditions found on some exoplanets to be modeled.

4.1.1 Hydrostatic Approximation

In hydrodynamical model applications, the stability of numerical solving methods is closely associated with numerical error, as well. A finite difference scheme is stable if the errors made at one time step of the calculation do not cause the errors to increase as the computations are continued. A neutrally stable scheme is characterized by the demand that errors remain constant as the computations are carried forward. If the errors decay and eventually damp out, the numerical scheme is said to be stable (Owolabi and Atangana, 2019). If, on the other hand, the errors grow with time the numerical scheme is said to be unstable (Smith, 1985). In numerical analysis, von Neumann stability analysis (Charney et al., 1950) (also known as Fourier stability analysis) is a procedure used to check the stability of finite difference schemes as applied to linear partial differential equations. As atmospheric motion occurs on a wide variety of time-scales, from the fast propagation of acoustic and gravity waves via the slower motions induced by the Coriolis force through to very slow dynamics due to seasonal cycles, the numerical models have to be optimized to deal with these different phenomena in terms of being numerically stable. Since the spectral model operates with a finite number of waves to approximate physical fields, the non-interaction with the waves outside the truncation limit, a so-called *blocking effect* occurs at the highest wave numbers, amplifying the small scale waves and leading to serious errors for the large scale components after a certain number of modeling time-steps (Liakka, 2006).

The speed of sound in air is of the order $c_\mathrm{s} \sim 350\,\mathrm{ms^{-1}}$ which makes sound travel about $20\,\mathrm{km}$ per minute and hence, limiting the stability criteria of modeling time-steps to the order of minutes, even for a coarse resolution model which is unpractical for long term climate calculations. Hence the Navier-Stokes equations are "filtered" to remove the acoustic modes as natural modes of the system which is done by removing the density dependence on the pressure together with the assumption that dynamic perturbations in density $\Delta\rho$ are small as compared to the mean density $\bar{\rho}$ (Boussinesq approximation)

$$\Delta\rho \ll \bar{\rho}. \tag{4.1}$$

Essentially the Boussinesq approximation allows to linearize terms involving a product with the density ρ (e.g. $\rho\boldsymbol{v} \to \bar{\rho}\boldsymbol{v}$) (Adcroft et al., 2004). The hydrostatic approximation states that the pressure

at any point in the atmosphere is completely defined by the weight of atmospheric material above it or, in other words, that the flow velocity at each point is constant over time. This implies that external forces, such as gravity or centrifugal force are balanced by a pressure gradient force and excludes highly convective flows from the modeling capabilities as well as high frequency internal waves such as the aforementioned acoustic modes.

In 2006, hydrostatic equilibrium was adopted as one of the main distinguishing criterion between dwarf planets and small Solar System bodies by the International Astronomical Union in their definition of a planet (IAU, 2006). This qualification typically means that the object has the shape of a spheroid or ellipsoid with only slight deviation from the spherical shape, where any irregular surface features are due to a relatively thin solid crust. Sometimes the equilibrium shape is an oblate spheroid, as is the case with the Earth. However, in the cases of moons in synchronous orbit, near unidirectional tidal forces create a scalene ellipsoid, and the dwarf planet Haumea appears to be scalene due to its rapid rotation (Rabinowitz et al., 2006).

In the Solar System, it appears that icy objects with a diameter larger than ca. $400\,\mathrm{km}$ are usually in hydrostatic equilibrium, while those smaller than that are not. Icy objects, though, can achieve hydrostatic equilibrium at a smaller size than rocky objects because of their much lower surface temperature (Vallis, 2006). The smallest object known to be in hydrostatic equilibrium is the icy moon Mimas at $397\,\mathrm{km}$ with a surface temperature of $T_{\mathrm{s}} \sim 64\,\mathrm{K}$ (Jacobson et al., 2006), while the largest object known not to be is the rocky asteroid Pallas at $532\,\mathrm{km}$ with a surface temperature of $T_{\mathrm{s}} \sim 164\,\mathrm{K}$ (Schmidt et al., 2008). As hydrostatic equilibrium is a key assumption in the context of atmospheric modeling as used in this thesis, all objects that are to be modeled have to be planets according to the IAU definition or at least *planetary mass objects* (PMOs), fulfilling the hydrostatic equilibrium assumption.

4.1.2 Gravity Waves

The next fast process after acoustic waves that can limit the time step is external gravity waves. Gravity waves are waves generated in a fluid medium or at the interface between two media (e.g. the atmosphere and the ocean) where gravity is the restoring force. In the Earth's atmosphere, gravity waves are a mechanism for the transfer of momentum from the troposphere to the stratosphere (Vallis, 2006). These waves propagate with phase speed $c_{\mathrm{p}} = \sqrt{g\lambda}$ where g is the acceleration of gravity and λ the corresponding wavelength resulting in wave speeds of $200\,\mathrm{ms}^{-1}$ for a typical nominal wavelength of $\lambda = 4\,\mathrm{km}$. For a resolution of $100\,\mathrm{km}$ an explicit time-step would be limited to of order $10\,\mathrm{min}$ which is somewhat smaller than the next explicit frequency in the system, the inertial waves due to the Coriolis force with a period of $(2\Omega)^{-1} \sim 7000\,\mathrm{s} \sim 2\,\mathrm{h}$, where Ω is the earth's angular velocity, accounting for the planets diurnal rotation (Vallis, 2006). The fast gravity modes are linearized around a reference temperature profile T_0. Hence the corresponding terms can be separated into fast linear gravity modes and slower non linear terms where the linear terms contain the effect of divergence on the surface pressure, the temperature tendency and the potential of the Earth's gravity

field (Lunkeit et al., 2011).

The hydrodynamic approximation filters vertical sound waves at the lower boundary condition in σ-coordinates (see below), which leads to a vanishing vertical velocity at the surface, suppresses horizontal sound waves. As the fast propagation of gravity waves strongly reduces the time-step of explicit numerical schemes an implicit scheme is used for the divergence, while mode splitting is applied to the spectral model (Dahms, 2013). The vorticity equation (see below) is solved by an explicit leapfrog integration method where the Robert-Asselin time filter is applied (Smith, 2010), a filter specifically designed for the leapfrog scheme that dampens the computational mode but leaves the physical mode relatively undamped.

4.2 Primitive Equations

The primitive equations describing the dynamical core of all circulation models consist of the conservation of (angular) momentum as well as mass and energy, respectively, the primitive laws of thermodynamics and some equation of state describing the atmospheric properties. These equations are usually simplified—as with the `PUMA/Plasim` model code—by the hydrostatic approximation $\mathrm{d}p = -\rho\,\mathrm{d}\Phi$ which assumes an exact equilibrium in the vertical between the pressure gradient force and the gravitational force where p is the atmospheric pressure, ρ the atmospheric density and Φ the geopotential[1]. These primitive equations relate the basic circulation model variables u and v which describe the zonal and meridional velocities of the atmospheric flows as well as the vertical velocity ω to the temperature T and the geopotential Φ. They consist of a set of coupled partial differential equations.

With the primitive equations the horizontal velocities $\boldsymbol{u} = (u, v)$ are related to the temperature T and the geopotential Φ in the following way

$$\frac{\mathrm{d}\boldsymbol{u}}{\mathrm{d}t} + f\hat{n} \times \boldsymbol{u} + \nabla_p \Phi = 0 \tag{4.2}$$

$$\frac{\mathrm{d}T}{\mathrm{d}t} - \frac{\kappa T \omega}{p} = 0 \tag{4.3}$$

$$\nabla_p \cdot \boldsymbol{u} + \frac{\partial \omega}{\partial p} = 0 \tag{4.4}$$

$$\frac{\partial \Phi}{\partial p} = 0 \tag{4.5}$$

where $\hat{n}$ is the surface normal, ∇_p the nabla-operator with respect the vertical pressure scale[2] and $f = 2\Omega \sin\varphi$ the Coriolis parameter defined by the planets angular velocity Ω and the latitude as measured from the planets equator[3]. Equation (4.2) is called momentum equation describing hydro-

---

[1]As the term geopotential with its prefix is a set expression in meteorological applications, it is used in this thesis even though the focus is mainly on exoplanets.

[2]In meteorological applications the pressure p or some derived variable is used as the vertical coordinate rather than a spacial z coordinate which is comparable to the use of optical depth in astrophysical applications.

[3]Spherical coordinates in the field of meteorological research are defined with a reference to the sphere's equator ($\varphi = 0$)
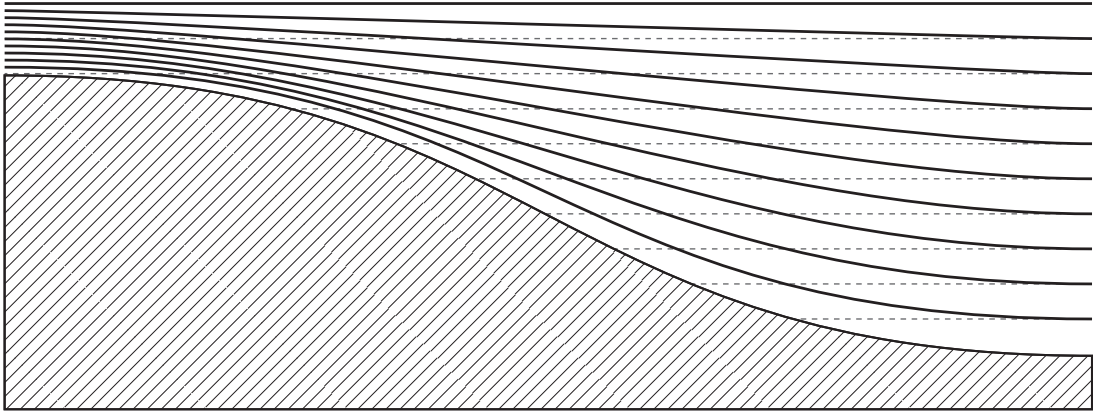
Figure 4.1. Schematic diagram of the σ-coordinate system. The σ-levels (solid lines) are terrain-following in contrast to the geometrical height levels (dashed lines).

dynamical flow on the surface of a sphere under the assumption that vertical motion is much smaller than horizontal motion (hydrostasis) and that the atmospheric depth is small as compared to the radius of the sphere[4], equation (4.3) is the thermodynamic equation relating the overall temperature of the system to heat sources and sinks, equation (4.4) is named continuity equation, representing the conservation of mass while equation (4.5) is the hydrostatic equation, a special case of the vertical momentum equation in which there is no background vertical acceleration. The thermodynamic equation is described by the pressure p, the vertical velocity ω and $\kappa = R/c_p$, where R is the gas constant for dry air, and c_p is the specific heat capacity for dry air at constant pressure (Liakka, 2006). Furthermore, α is defined as $\alpha = \rho^{-1}$, where ρ is the atmospheric density. As the frame of reference is not comoving with the atmospheric material the total time derivative has to be written as

$$\frac{\mathrm{d}}{\mathrm{d}t} = \frac{\partial}{\partial t} + \boldsymbol{u} \cdot \nabla + \omega \frac{\partial}{\partial p} \tag{4.6}$$

where the first term accounts for the actual temporal alteration at the place under consideration and the second and third term regards the atmospheric property change which is induced by the movement of the flowing material in horizontal and vertical direction, respectively.

4.2.1 Sigma Coordinate System

Longitude λ- and latitude φ-coordinates describe the horizontal position onto the surface of the sphere. As a first step to obtain the equations in Hoskins and Simmons (1975) the vertical coordinate will be

---

rather than to its pole which is common convention with respect to spherical coordinates in other domains. To account for this, spherical coordinates that are defined with respect to the sphere's equator are denoted as (φ, λ) while those with reference to the sphere's pole are referred to as (θ, φ).

[4]This is a first limitation with respect to the classes of exoplanets that can be modeled as the (geometrically) thin atmosphere is a basic boundary condition for the model setup.

changed from pressure p to the so-called σ-coordinates, which are terrain-following (cf. fig. 4.1) and defined as

$$\sigma = \frac{p}{p_s},$$ (4.7)

where p_s is the pressure at surface level. The σ-coordinate system functions as vertical height scale which is defined as the ratio of the pressure at a given point in the atmosphere to the pressure on the surface of the planet underneath it. The main advantage of changing to σ-coordinates is the very simple boundary condition for the vertical velocity (Liakka, 2006). If the pressure was used as the vertical coordinate, the boundary conditions at the surface would be very difficult to define due to the variations of the surface height. The σ-coordinate values ranges from one (surface of the planet) to zero (far out of the planetary atmosphere). According to this definition, the values of the height coordinate increases when moving into the atmosphere and thus, show the same habit as the optical depth that is used in radiative transfer applications. The σ-coordinate decreases monotonically with geometric height z, hence each geometric height corresponds to some σ-level and vice versa (bijectivity). The vertical velocity in σ-coordinates is referred to as

$$\dot{\sigma} = \frac{\mathrm{d}\sigma}{\mathrm{d}t}$$ (4.8)

with the corresponding boundary conditions

$$\dot{\sigma}(\sigma = 1) = \dot{\sigma}(\sigma = 0) = 0.$$ (4.9)

In order to rewrite the primitive equations in σ-coordinates the ∇-operator has to be transformed to the new coordinate system. The derivative with respect to the geometric height is

$$\frac{\partial}{\partial z} = \frac{\partial \sigma}{\partial z}\frac{\partial}{\partial \sigma}$$ (4.10)

and the derivative to any other coordinate s, $s \in \{x, y, t\}$ may be written as

$$\left(\frac{\partial}{\partial s}\right)_\sigma = \left(\frac{\partial}{\partial s}\right)_z + \left(\frac{\partial z}{\partial s}\right)_\sigma \frac{\partial}{\partial z}$$ (4.11)

where the subscript indicates the quantity to be kept constant. With the latter two equations and the definition of the σ-coordinate

$$\left(\frac{\partial \sigma}{\partial s}\right)_p = -\frac{\sigma}{p_s}\frac{\partial p_s}{\partial s}$$ (4.12)

the ∇-operator as the horizontal derivative in the σ-coordinate system results in

$$\nabla_p = \nabla_\sigma - \frac{\sigma}{p_s}(\nabla_\sigma p_s)\frac{\partial}{\partial \sigma}$$ (4.13)

and corresponding the time derivative of equation 4.6 in

$$\frac{\mathrm{d}}{\mathrm{d}t} = \frac{\partial}{\partial t} + \boldsymbol{u} \cdot \nabla_\sigma + \dot{\sigma} \frac{\partial}{\partial \sigma}. \tag{4.14}$$

4.2.2 Primitive Equations in Sigma Coordinate System

With these derivative operators the primitive equations may be rewritten in the new σ-coordinate system. Below, each of the primitive equations will be translated into the new coordinate system.

Hydrostatic Equation With the new coordinate system, the hydrostatic equation (4.5) can be expressed as

$$\frac{\partial \Phi}{\partial p} + \alpha = \frac{1}{p_\mathrm{s}} \frac{\partial \Phi}{\partial \sigma} + \alpha = \frac{\partial \Phi}{\partial \sigma} + \frac{RT}{\sigma} = 0 \tag{4.15}$$

where the ideal gas law $p\alpha = RT$ has been used in the last step. This equation could easily be integrated if the run of the temperature along the σ-coordinate was known

$$\Phi(\sigma) = \Phi_\mathrm{s} - \int\limits_1^\sigma \frac{RT(\sigma)}{\sigma} \, \mathrm{d}\sigma \tag{4.16}$$

where Φ_s denotes the geopotential at the planet's surface. Eq. 4.16 is one of the so-called *diagnostic equations* (see below) describing the geopotential for a given sigma-level.

Momentum Equation To transform the momentum equation (4.2) into the σ-coordinate system, the derivative operators (4.13) and (4.14) have to be applied resulting in

$$\frac{\mathrm{d}\boldsymbol{u}}{\mathrm{d}t} + f\hat{n} \times \boldsymbol{u} + \nabla_\sigma \Phi - \frac{\sigma}{p_\mathrm{s}}(\nabla_\sigma p_\mathrm{s})\frac{\partial \Phi}{\partial \sigma} = 0 \tag{4.17}$$

or

$$\frac{\mathrm{d}\boldsymbol{u}}{\mathrm{d}t} = -\boldsymbol{u} \cdot \nabla_\sigma \boldsymbol{u} - \dot{\sigma}\frac{\partial \boldsymbol{u}}{\partial \sigma} - f\hat{n} \times \boldsymbol{u} - RT\nabla_\sigma \pi - \nabla_\sigma \Phi \tag{4.18}$$

where the logarithmic pressure $\pi \equiv \ln(p_\mathrm{s}/\bar{p})$ has been defined, $\bar{p}$ is a constant averaged reference pressure. To address the discontinuities at the poles of the sphere which arise from the fact that a sphere is not homeomorph to the $\mathbb{R}^2$-space, the momentum equation is usually defined in terms of vorticity and divergence for modeling purposes. A vector field cannot be defined at $\varphi = \pm\frac{\pi}{2}$ because of the directional ambiguity. In contrast to the horizontal wind field, the divergence and vorticity are represented by scalars, which can be defined all over the sphere (Liakka, 2006). To derive the vorticity and divergence equation the individual terms of the latter equation have to be reformulated in terms of the vorticity and divergence. Using the vector

identity

$$
\begin{aligned}
\boldsymbol{u} \cdot \nabla_\sigma \boldsymbol{u} &= \tfrac{1}{2} \nabla_\sigma (\boldsymbol{u} \cdot \boldsymbol{u}) - \boldsymbol{u} \times (\nabla_\sigma \times \boldsymbol{u}) \\
&= \tfrac{1}{2} \nabla_\sigma (\boldsymbol{u} \cdot \boldsymbol{u}) - \boldsymbol{u} \times \zeta \hat{n} \\
&= \tfrac{1}{2} \nabla_\sigma (\boldsymbol{u} \cdot \boldsymbol{u}) + \zeta \hat{n} \times \boldsymbol{u},
\end{aligned}
\tag{4.19}
$$

the momentum equation may be rewritten as

$$
\frac{\mathrm{d}\boldsymbol{u}}{\mathrm{d}t} = -\tfrac{1}{2} \nabla_\sigma (\boldsymbol{u} \cdot \boldsymbol{u}) + \eta \hat{n} \times \boldsymbol{u} - \dot{\sigma} \frac{\partial \boldsymbol{u}}{\partial \sigma} - RT \nabla_\sigma \pi - \nabla_\sigma \varphi
\tag{4.20}
$$

where the relative vorticity $\zeta \equiv \hat{n} \cdot \nabla_\sigma \times \boldsymbol{u}$ and the absolute vorticity $\eta \equiv \zeta + f$ have been defined. Applying the nabla operator to the latter equation and introducing divergence $\delta \equiv \nabla_\sigma \cdot \boldsymbol{u}$ yields to the final divergence equation, describing the temporal development of the first scalar field

$$
\frac{\mathrm{d}\delta}{\mathrm{d}t} = -\tfrac{1}{2} \nabla_\sigma^2 (\boldsymbol{u} \cdot \boldsymbol{u}) + \hat{n} \cdot \nabla_\sigma \times (\eta \boldsymbol{u}) - \nabla_\sigma \cdot \dot{\sigma} \frac{\partial \boldsymbol{u}}{\partial \sigma} - \nabla_\sigma \cdot RT \nabla_\sigma \pi - \nabla_\sigma^2 \varphi.
\tag{4.21}
$$

As this equation describes the development of the vorticity over time it is referred to as *prognostic equation* to distinguish it from the diagnostic equations. To derive the vorticity equation as the prognostic equation for the second scalar field, the operator $\hat{n} \cdot \nabla_\sigma \times$ is applied to Eg. 4.20, resulting in

$$
\frac{\mathrm{d}}{\mathrm{d}t}(\hat{n} \cdot \nabla_\sigma \times \boldsymbol{u}) = -\hat{n} \cdot \nabla_\sigma \times \left[\tfrac{1}{2} \nabla_\sigma (\boldsymbol{u} \cdot \boldsymbol{u}) + \dot{\sigma} \frac{\partial \boldsymbol{u}}{\partial \sigma} + RT \nabla_\sigma \pi + \nabla_\sigma \varphi \right] - \\
- \hat{n} \cdot \nabla_\sigma \times [\eta(\hat{n} \times \boldsymbol{u})]
\tag{4.22}
$$

which may be rearranged to

$$
\frac{\mathrm{d}\eta}{\mathrm{d}t} = -\nabla_\sigma \cdot (\eta \boldsymbol{u}) - \hat{n} \nabla_\sigma \times \left[\dot{\sigma} \frac{\partial \boldsymbol{u}}{\partial \sigma} + RT \nabla_\sigma \pi \right],
\tag{4.23}
$$

keeping in mind that $\nabla_\sigma \times \nabla_\sigma = 0$. By splitting the scalar temperature field $T(x, y, \sigma, t)$ into a sigma-level average $\bar{T}(\sigma)$ and its corresponding average deviation $T'(x, y, \sigma, t)$ according to

$$
T(x, y, \sigma, t) = \bar{T}(\sigma) + T'(x, y, \sigma, t),
\tag{4.24}
$$

the final vorticity equation may be derived as

$$
\frac{\mathrm{d}\eta}{\mathrm{d}t} = -\nabla_\sigma \cdot (\eta \boldsymbol{u}) - \hat{n} \cdot \nabla_\sigma \times \left[\dot{\sigma} \frac{\partial \boldsymbol{u}}{\partial \sigma} + RT' \nabla_\sigma \pi \right].
\tag{4.25}
$$

and the divergence equation, respectively

$$\frac{\mathrm{d}\delta}{\mathrm{d}t} = \hat{n} \cdot \nabla_\sigma \times (\eta \boldsymbol{u}) - \tfrac{1}{2}\nabla_\sigma^2 \left[(\boldsymbol{u} \cdot \boldsymbol{u}) + R\bar{T}\pi + \varphi\right] - \nabla_\sigma \cdot \left[\dot{\sigma}\frac{\partial \boldsymbol{u}}{\partial \sigma} + RT'\nabla_\sigma \pi\right]. \quad (4.26)$$

Thus, using the splitting of the temperature field for both, the divergence equation (Eq. 4.21) and the vorticity equation (Eq. 4.25) results in a consistent description of the two scalar fields, replacing the vectorial momentum equation 4.2.

Thermodynamic Equation The thermodynamic equation may easily be transformed to sigma-coordinates by applying the abovementioned nabla and time derivative operator

$$\frac{\mathrm{d}T}{\mathrm{d}t} = -\boldsymbol{u}\nabla_\sigma T - \dot{\sigma}\frac{\partial T}{\partial \sigma} + \frac{\kappa T \omega}{p} \quad (4.27)$$

Continuity Equation Applying the sigma-coordinate derivative operators to the continuity equation yields to

$$\begin{aligned} 0 &= \frac{1}{p_\mathrm{s}}\nabla_\sigma \cdot (P_\mathrm{s}\boldsymbol{u}) + \frac{1}{p_\mathrm{s}}\frac{\partial p_\mathrm{s}}{\partial t} + \frac{\partial \dot{\sigma}}{\partial \sigma} \\ &= \frac{1}{p_\mathrm{s}}\nabla_\sigma \cdot (P_\mathrm{s}\boldsymbol{u}) - \boldsymbol{u} \cdot \nabla_\sigma \pi - \nabla_\sigma \cdot \boldsymbol{u} \end{aligned} \quad (4.28)$$

where the derivation of the vertical velocity ω in the sigma-coordinate system has been used

$$\frac{\mathrm{d}\omega}{\mathrm{d}\sigma} = p_\mathrm{s}\frac{\partial \dot{\sigma}}{\partial \sigma} + \frac{\partial p_\mathrm{s}}{\partial t} + \boldsymbol{u} \cdot \nabla_\sigma p_\mathrm{s} + \sigma\frac{\partial \boldsymbol{u}}{\partial \sigma} \cdot \nabla_\sigma p_\mathrm{s}. \quad (4.29)$$

By defining the vertical pressure flow $G \equiv \boldsymbol{u}\nabla_\sigma \pi + \nabla_\sigma \boldsymbol{u}$ and integrating this equation from the planet's surface to the top of its atmosphere, the final continuity equation is obtained in the form

$$\frac{\partial \pi}{\partial t} + \int_0^1 G \, \mathrm{d}\sigma = 0. \quad (4.30)$$

As aforementioned, in atmospheric modeling theory, the fundamental equations are formally divided into *diagnostic equations* (DE), used to calculate the relevant model quantities for a given point in time and *prognostic equations* (PE), using the quantities determined by the DEs to calculate the corresponding tendencies. The definition of the logarithmic pressure and vertical pressure flow belong to the DEs as well as the hydrostatic equation (Eq. 4.16). Equation 4.30 may be used to derive

the two remaining DEs (Liakka, 2006). This yields to the five diagnostic equations in the form

$$\Phi(\sigma) = \Phi_{\mathrm{s}} - \int\limits_{1}^{\sigma} \frac{RT(\sigma)}{\sigma}\, \mathrm{d}\sigma \tag{4.31}$$

$$p_{\mathrm{s}} = \bar{p} \exp \pi \tag{4.32}$$

$$G = \boldsymbol{u}\nabla_{\sigma}\pi + \nabla_{\sigma}\boldsymbol{u} \tag{4.33}$$

$$\frac{\omega}{p} = -\frac{p_{\mathrm{s}}}{p} \int\limits_{0}^{\sigma} G\, \mathrm{d}\sigma + \boldsymbol{u} \cdot \nabla_{\sigma}\pi \tag{4.34}$$

$$\dot{\sigma} = \sigma \int\limits_{0}^{1} G\, \mathrm{d}\sigma - \int\limits_{0}^{\sigma} G\, \mathrm{d}\sigma \tag{4.35}$$

The prognostic equations have already been deduced in this section in the form of the divergence and vorticity equations' (Eq. 4.21, Eq. 4.25) as well as the temperature equation's (Eq. 4.27) and pressure equation's (cf. Eq. 4.30) temporal derivative. They may be summarized as

$$\frac{\mathrm{d}\delta}{\mathrm{d}t} = \hat{n} \cdot \nabla_{\sigma} \times (\eta\boldsymbol{u}) - \tfrac{1}{2}\nabla_{\sigma}^2 \left[(\boldsymbol{u} \cdot \boldsymbol{u}) + R\bar{T}\pi + \varphi \right] - \nabla_{\sigma} \cdot \left[\dot{\sigma}\frac{\partial \boldsymbol{u}}{\partial \sigma} + RT'\nabla_{\sigma}\pi \right] \tag{4.36}$$

$$\frac{\mathrm{d}\eta}{\mathrm{d}t} = -\nabla_{\sigma} \cdot (\eta\boldsymbol{u}) - \hat{n} \cdot \nabla_{\sigma} \times \left[\dot{\sigma}\frac{\partial \boldsymbol{u}}{\partial \sigma} + RT'\nabla_{\sigma}\pi \right] \tag{4.37}$$

$$\frac{\mathrm{d}T}{\mathrm{d}t} = -\boldsymbol{u}\nabla_{\sigma}T - \dot{\sigma}\frac{\partial T}{\partial \sigma} + \frac{\kappa T\omega}{p} \tag{4.38}$$

$$\frac{\partial \pi}{\partial t} = -\int\limits_{0}^{1} G\, \mathrm{d}\sigma. \tag{4.39}$$

With a given set of atmospheric velocity $\boldsymbol{u}$, temperature T and pressure π for a certain point in time, the diagnostic equations may be solved. This result can then be used in return to evaluate the tendencies of these quantities due to the prognostic equations, creating the input for the next time-step.

4.3 Parameterizations

If not denoted otherwise, the following discussion is based on the information provided by Lunkeit et al. (2011). Processes like boundary-layer fluxes, i.e. the description of the air layer near the ground affected by diurnal heat as well as momentum transfer to or from the surface, diffusion and moist processes are unresolved but included as simplified parameterizations in the `Planet Simulator` (Dahms, 2013). This mainly effects the treatment of the *planetary boundary layer* (PBL) as the lowest part of the planet's atmosphere whose behavior is directly influenced by its contact with the planetary surface. The PBL is distinguished from the free atmosphere in which the wind may be approximated as geostrophic, i.e. parallel to the isobars, while within the PBL the wind turns across the isobars.
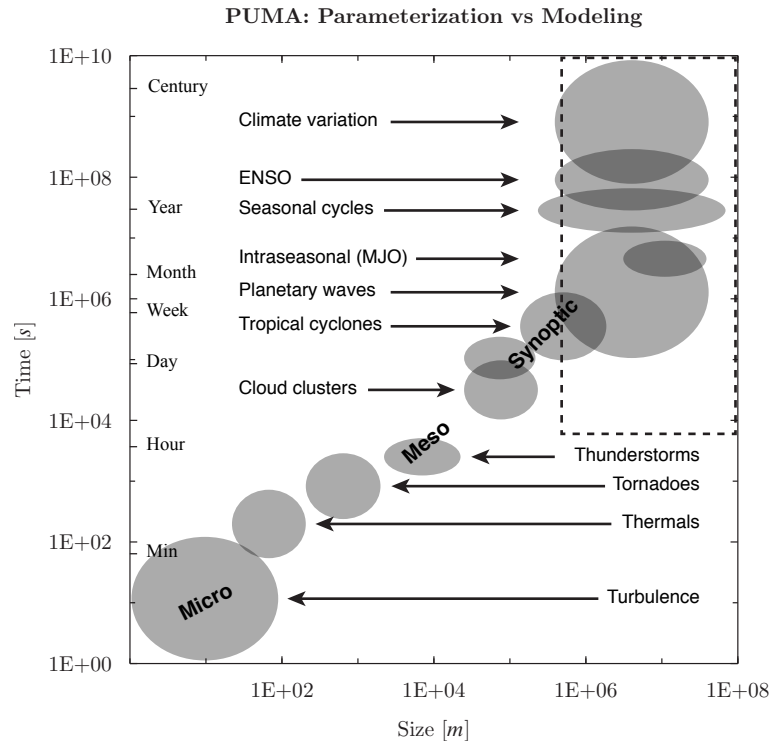
Figure 4.2. Visualization of `PUMA`-modeling capabilities: Only processes that take place in the spacial and temporal domain marked by the dashed-line box can truly be modeled. All the other processes have influences on the overall modeling by parametrizations that are partially adjusted to earth conditions to some degree.

Hence, the PBL is characterized by more turbulent processes. The turbulent eddies are much smaller than the scales that can be resolved in a GCM and are parameterized following the methods of Louis (1979) which address the vertical eddy fluxes of heat, momentum and moisture. The applied parameterization scheme for the surface fluxes is based on the Monin-Obukhov similarity theory (Obukhov, 1971). In the PBL, bulk formulas are used to parameterize fluxes of zonal and meridional momentum (wind stress) as well as sensible and latent heat where the fluxes are positive in downward direction (towards the surface) and negative in upwards direction (away from the surface) (Dahms, 2013). The drag and the transfer coefficient for heat are calculated following the method described by Roeckner et al. (1992) which itself again is based on the methods of Louis (1979). Actually, this parameterization has been developed for earth conditions but do not include any assumptions that are very earth specific and thus, it should hold in most exoplanet model setups as well, as long as surface roughness is comparable (Tillman et al., 1994). Turbulent mixing is not resolved in the model but represented by a vertical diffusion applied to the horizontal wind components u and v, the potential temperature θ as well as the specific humidity q. The turbulent fluxes of zonal and meridional velocity, heat and moisture are parameterized by a vertical diffusion along the vertical gradient with the exchange coefficients for momentum and heat, which are calculated due to the mixing length approach (Dahms, 2013). Horizontal diffusion is computed in spectral space and based on the parameterization

by Laursen and Eliasen (1989).

As the area of rising motion in moist convection processes is very small as compared to the horizontal resolution of the model, some cloud formation processes have to be parameterized like cumulus convection following a Kuo-type convection scheme (Kuo, 1965, 1974) in which convection is activated in a conditionally unstable layer between the pressure levels, if there is net-convergence of moisture into the grid box. Clouds are very important for the description of the planetary albedo. Currently the parameterization is highly adjusted to cloud formation processes on Earth conditions, e.g. it can treat water clouds only and thus, methane clouds as found in Titan's atmosphere are not covered. Moreover, `PHOENIX-3DRT` is currently not capable of handling Mie scattering which is predominant in clouds. Therefore, neither the formation of clouds nor the radiative transfer within clouds are sufficiently resolved in the model code and model setups that are influenced by cloud coverage effects to a high degree should be treated with caution.

In principle, phase changes of convective and large-scale precipitations within the atmosphere are considered (Dahms, 2013). Actually, the melting and freezing of precipitation is modeled for water (H_2O) only because it is controlled by a single temperature level defining the triple point of water indicating the phase change condition and set to $T_{th} = 271.16\,\text{K}$ as a threshold. This threshold temperature has been made configurable for the sake of modeling phase changes of other liquids and to account for the change in partial pressure with respect to the corresponding species. Nevertheless, phase changes are controlled by a constant threshold temperature that is not adjusted during modeling phase and restricted to one predominant species. This implies that the threshold temperature acts as an independent input variable and phase changes are modeled assuming the temperature to be valid for the conditions within the exoplanets atmosphere. Evaporation is parameterized in terms of the saturation deficit describing the amount of moisture in the air and how much moisture the air can hold when it is saturated and again, is closely related to earth conditions. This means, that phase changes are taken into account and may be adjusted to exoplanet conditions to some degree but cannot be treated self-consistently.

Some land surface properties are parameterized in `Plasim`. This parameterizations include a soil hydrology and a river transport system to have a closed circuit for the water fluxes. Surface maps, specifying land-sea mask, orography, roughness length (turbulent fluxes) and evaporation efficiency (phase changes) have to be provided if needed (cf. fig. 5.3), albedo (irradiative heat) may be provided as well but is calculated by default, using the Lambertian component of the BRDF model. Since there is no coupling to some land-ice models glaciers are treated like land points but with surface and soil characteristics appropriate for ice (Dahms, 2013). The treatment of surface properties using quantity maps makes the model highly flexible in terms of fine-tuning it to certain planet conditions but, on the other hand, dramatically increases the parameter-space. This means that any observable data with respect to today's techniques may be 'fitted' with nearly unlimited combinations of input parameters. More precisely, with a given threshold of a quantity describing the goodness of the 'fit' model using some statistical hypothesis testing method such as the chi-squared (χ^2) test, the volume in parameter-space which represents vectors of input parameters, valid to represent models not violating

this threshold, is huge and may show disjointed sub-volumes or the mapping, connecting some input vector to the goodness quantity, is even discontinuous which prevent the definition of such valid volumes at all. This basically means that e.g. the exact orography or land-sea mask may be used to specify planetary conditions but cannot be reconstructed from the observed spectra right now.

5. Testing the Model

The model can only reliably be tested if the calculated quantities such as temperature profiles, surface albedo or transmission and reflection spectra may be compared to some observed and thus measured reference values. This not just implies the observational data to be of high enough quality in terms of resolution as well as signal-to-noise ratio (SNR) to enable reliable testing conditions, but also the quantities to be dependable, i.e. close to the actual raw data and not calculated as part of complex models themselves. Principally, this indicates the use of exoplanets' observations to be inadequate in this context, as the observed data, of course does not meet the addressed requirements, neither in terms of resolution or SNR nor with respect to the closeness to the actual raw data if e.g. temperature profiles are to be examined. Nevertheless, there is a perfect candidate to serve as a reference object in our immediate neighborhood: Mars; and as the classification into planets and exoplanets is artificial from every point of view and hence just an expression of our own perspective it is also valid in the context of exoplanet model development.[1]

With respect to `PHOENIX`, our own sun is just an ordinary G2V star which is used as an irradiation source within the model and as the code has never been developed with any sun specific characteristics, it is just an example star in this model setup but may easily be exchanged for another host star with modified spectral class in a true exoplanet model setup if desired. Although the `PUMA/Plasim` code in fact has been developed for earth and hence solar-system conditions, all specifics concerning this configuration have been removed from the code. This may easily be verified, as the `PUMA/Plasim` code considered the spectrum of the host star and thus its spectral class only in terms of the short- and long-wave separation wavelength in the radiation module, which has completely been replaced by the `PHOENIX 3DRT` code. All other model input parameters beside the host star's spectral class have to be adapted to the Martian model anyhow and thus the model may be considered as a perfectly valid general purpose setup without any constrains to our own solar system.

Mars is well-suited for testing the developed model, as it is not only our direct neighbor but also the most Earth-like planet in the solar system, except for our own Earth, of course. However, the atmospheric properties, such as flow dynamics and climate are quite different form those on Earth in many aspects which enables the tests to check for consistency in a wide range of model dynamics. The greater distance to the sun enables the validation of the collaboration of the model frameworks

---

[1]In terms of planetary properties, Venus is an equally valid candidate to test the model. In contrast to Mars, however, the solar winds have a much greater influence on the atmosphere due to the shorter distance to the sun (Futaana et al., 2017). This influence cannot be represented with the present model setup, which means that the results for Mars seem more suitable for testing the general model capabilities.
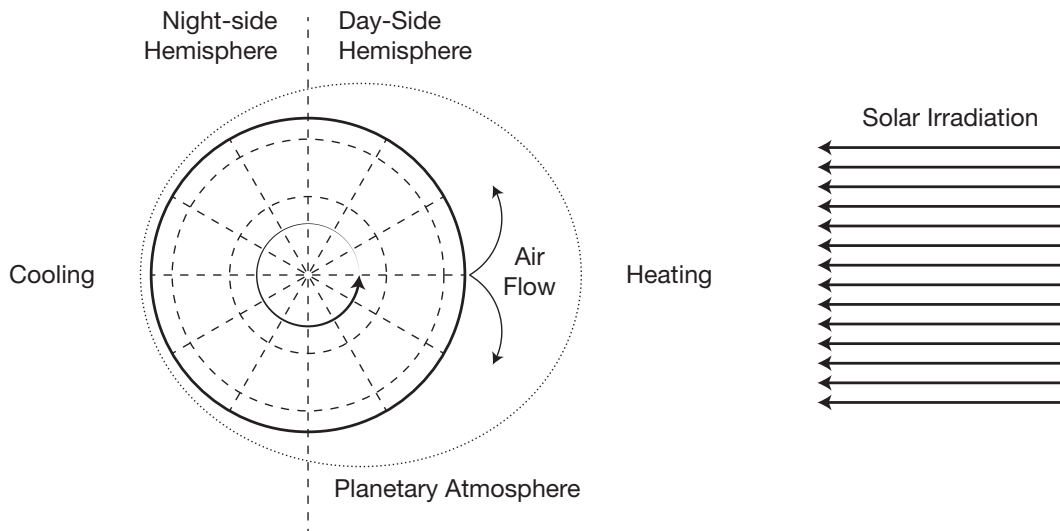
Figure 5.1. Illustration of the thermal tides at Mars, responsible for large, daily variations in pressure at the Martian surface (solid line). The solar irradiation causes the atmosphere (dotted line) to expand at the day-side (right of the terminator) while air flows out of the bulge, lowering the surface pressure. The bulge moves across the planet each day, from east to west due to the planet's rotation.

PHOENIX and PUMA/Plasim, as all Earth specific parameterizations concerning solar irradiation have to be resolved to deliver reasonable results. The absence of oceans on Mars facilitates the examination of the circulation model's applicability to atmospheric conditions that are obviously different from those on earth, as the error source induced by the simple ocean model disappears. On the other hand, the complete lack of liquid water leads to massive 'continental' climate and thus rapid changes in the temperature profiles in response to radiative changes. Therefore, so-called thermal tides are responsible for huge temperature and pressure variations on daily time scales (cf. fig. 5.1). The (relatively) large eccentricity of Mars' orbit results in an asymmetry of the irradiation with respect to northern and southern summer of about $30\,\%$ which shows up as an asymmetric melt and freeze out of the polar CO_2-ice caps and hence varying atmospheric mass over the year. This effect is specific to planets with huge eccentricity which show polar ice caps and hence does not occur on earth and, again, needs a flexible model not specialized to earth conditions.

The chemical composition of the Martian atmosphere is about $95\,\%$ carbon dioxide (CO_2), $2.5\,\%$ nitrogen (N_2), $1.5\,\%$ argon (Ar_2) and $0.1\,\%$ oxygen (O_2), the exact composition with all relevant species is compiled in tab. A.3. As mentioned above, the carbon dioxide condenses in the winter polar regions and sublimes again in the summer with a turnover of about $25\,\%$ of the total atmospheric mass. On an inter-annual time scale, dust storms are supposed to be responsible for the strongest variabilities with respect to solar irradiation and thus temperature and pressure profiles: Dust particles in the atmosphere may be thought of as aerosols in the Earth's atmosphere, absorbing the short wave solar irradiation and resulting in a temperature decrease at the surface and increase at high altitudes, respectively. Although, a dust model is included in the PHOENIX code (Witte, 2011), the dust storms are not included in the model calculations, as the atmospheric circulation model is currently not capa-
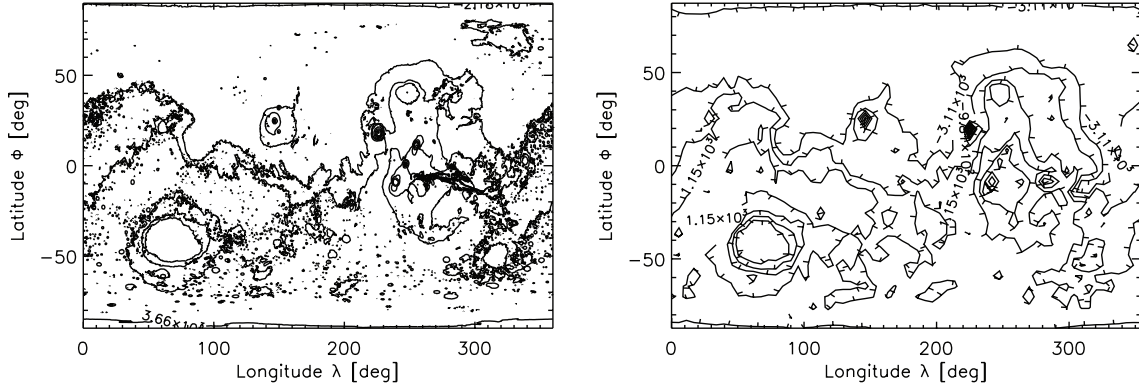
Figure 5.2. The NASA *Mars Orbiter Laser Altimeter* (MOLA) data is used for the orography map. The original MOLA data at an resolution of 4 px per degree is plotted on the left, the interpolated topology map (T21 resolution) on the right. The input map was created using bi-linear interpolation with respect to the horizontal grid configuration (cf. fig. 5.3).

ble of handling effects like this. As the Martian atmosphere is—except for the dust storms—optically thin the atmospheric circulation is driven by surface heating. This heating from the ground varies massively due to the large surface elevation (cf. fig. 5.2).

5.1 Model setup

This section describes in detail the setup of the Martian model. The Martian model has been set up with the parameters presented in tab. A.5. As with the Earth, the atmospheric dynamics on Mars are driven by the seasonal and daily cycles of solar irradiation, as well, but unlike Earth conditions, the relatively large eccentricity of $\epsilon = 0.093$ of the Martian orbit causes varying radiation fluxes on the northern and southern hemisphere during respective summers. Hence, the model has been calculated using altering distances to the sun during the orbital period, starting with some arbitrarily chosen solar longitude L_S^0 but accounting for the correct correlation between solar Longitude and northern/southern hemisphere summer. This is necessary to consider the increase in net solar irradiation during southern hemisphere summer.

5.1.1 Model Grid

The `PUMA/Plasim` model is a spectral model and thus, the corresponding equations are solved in Fourier space by expanding the dependent variables in terms of a finite series of smooth orthogonal functions. Functions in Fourier space are represented with finite precision, of course, implying the spectral coefficients to be truncated at some point. This causes the horizontal grid to be determined by the truncation scheme. With respect to the T21 truncation scheme used for atmospheric dynamics calculations throughout this thesis, the horizontal grid in position-space is fixed to 32 latitudes ($-90° \leq \varphi \leq 90°$) for each of the 64 longitudes ($0° \leq \lambda \leq 360°$) and yielding to a total of 2048 grid
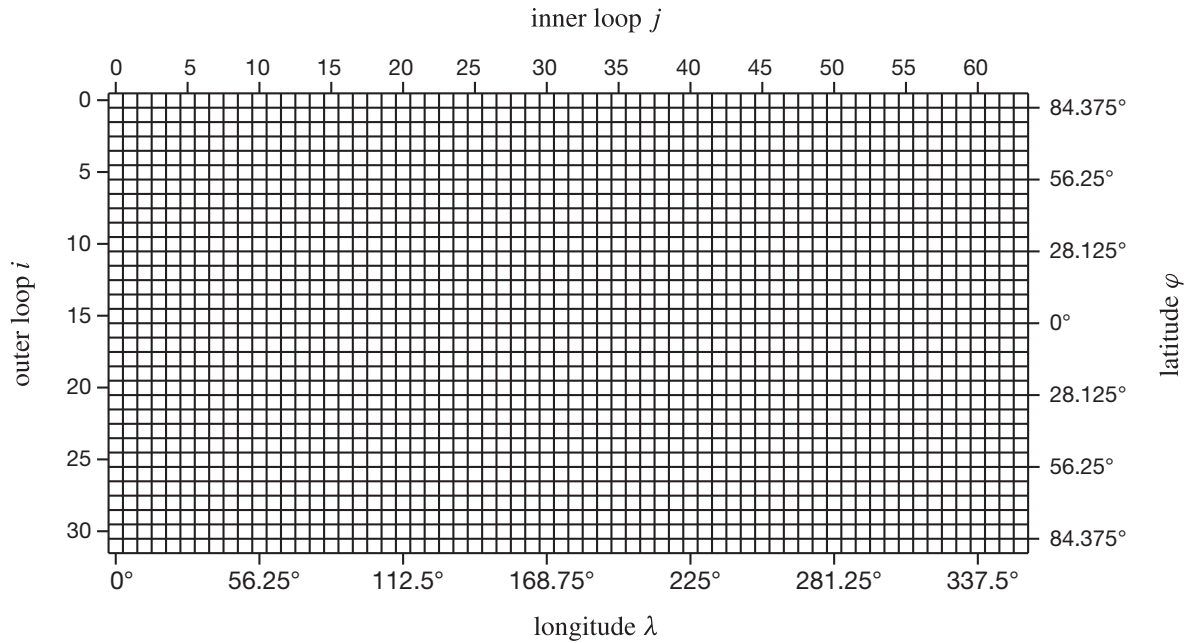
Figure 5.3. Schematic diagram of the horizontal grid configuration: The planetary surface is subdivided into 2048 grid points, 32 in latitudinal and 64 in longitudinal direction, according to the T21 resolution used in meteorological model frameworks as with `PUMA/Plasim`. Surface maps, such as orography or albedo maps are to be specified row by row, starting with the northernmost grid-row and at some arbitrarily chosen reference longitude. The labels inner and outer loop, respectively refer to the loop structure of the read-in procedure.

Table 5.1. Coordinates of the horizontal planetary surface grid: The grid consists of 32 latitudinal and 64 longitudinal coordinates which results in a total of 2048 grid points.

Grid latitude coordinates φ_i							
85.7606	80.2688	74.7445	69.2130	63.6786	58.1430	52.6065	47.0696
41.5325	35.9951	30.4576	24.9199	19.3822	13.8445	8.3067	2.7689
-2.7689	-8.3067	-13.8445	-19.3822	-24.9199	-30.4576	-35.9951	-41.5325
-47.0696	-52.6065	-58.1430	-63.6786	-69.2130	-74.7445	-80.2688	-85.7606

Grid longitude coordinates λ_j							
0.0000	5.6250	11.2500	16.8750	22.5000	28.1250	33.7500	39.3750
45.0000	50.6250	56.2500	61.8750	67.5000	73.1250	78.7500	84.3750
90.0000	95.6250	101.2500	106.8750	112.5000	118.1250	123.7500	129.3750
135.0000	140.6250	146.2500	151.8750	157.5000	163.1250	168.7500	174.3750
180.0000	185.6250	191.2500	196.8750	202.5000	208.1250	213.7500	219.3750
225.0000	230.6250	236.2500	241.8750	247.5000	253.1250	258.7500	264.3750
270.0000	275.6250	281.2500	286.8750	292.5000	298.1250	303.7500	309.3750
315.0000	320.6250	326.2500	331.8750	337.5000	343.1250	348.7500	354.3750

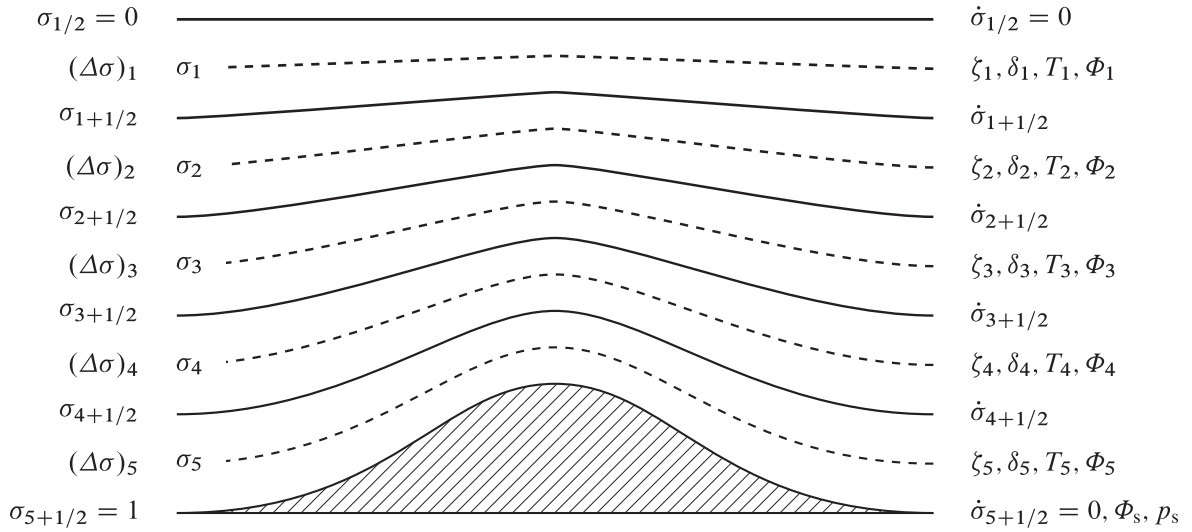|		
$\sigma_{1/2} = 0$		$\dot{\sigma}_{1/2} = 0$
$(\Delta\sigma)_1$	σ_1	$\zeta_1, \delta_1, T_1, \Phi_1$
$\sigma_{1+1/2}$		$\dot{\sigma}_{1+1/2}$
$(\Delta\sigma)_2$	σ_2	$\zeta_2, \delta_2, T_2, \Phi_2$
$\sigma_{2+1/2}$		$\dot{\sigma}_{2+1/2}$
$(\Delta\sigma)_3$	σ_3	$\zeta_3, \delta_3, T_3, \Phi_3$
$\sigma_{3+1/2}$		$\dot{\sigma}_{3+1/2}$
$(\Delta\sigma)_4$	σ_4	$\zeta_4, \delta_4, T_4, \Phi_4$
$\sigma_{4+1/2}$		$\dot{\sigma}_{4+1/2}$
$(\Delta\sigma)_5$	σ_5	$\zeta_5, \delta_5, T_5, \Phi_5$
$\sigma_{5+1/2} = 1$		$\dot{\sigma}_{5+1/2} = 0, \Phi_s, p_s$

Figure 5.4. Schematic diagram of the model's vertical discretization. The calculation of the vertical atmospheric structure is shown exemplarily for a total five sigma levels (dashed lines) though 10 levels have been used in the model calculations to account for the steep orography. All relevant quantities are calculated at the levels except for the vertical velocity $\dot{\sigma}$ which is examined at the boundary layer between the sigma levels (solid lines).

points (cf. fig. 5.3). The exact positions of the individual grid points are given in tab. 5.1. Thus, the corresponding distance between adjacent grid coordinates is $\Delta\varphi = \Delta\lambda \approx 5.6°$. All input parameter maps such as orography (cf. fig. 5.2) are interpolated onto this surface grid using bi-linear interpolation. The NASA *Mars Orbiter Laser Altimeter* (MOLA) data at a resolution of $4\,\text{px}$ per degree is used for the orography input map. Although not artificially smoothed, the interpolation causes some of the minor topographic features to be averaged out of the input map as well as the restriction of the total topographic range. Nevertheless, the topographic range after the interpolation process is still more than $14\,\text{km}$. This is considerably more than for a comparable Earth setup and particularly with the smaller planetary radius of Mars leads to a challenge for the circulation model.

The vertical resolution is given by 10 sigma levels representing atmospheric h between $0.2\,\text{km}$ and $35.2\,\text{km}$. The exact positions of the individual levels are given in table A.4. Additionally, the model calculates the relevant quantities for the planetary surface ($h = 2\,\text{m}$), resulting in a total of 11 height levels. All quantities are calculated at the sigma levels except for the vertical velocity $\dot{\sigma}$ which is examined at the boundary layer between the sigma levels (cf. 5.4). Horizontal and vertical grid result in a voxel-grid of $20\,480$ which is quite small as compared to the big grid of about $250\,000$ voxels or even more but necessary as the model computes the relevant radiative transport quite frequently to interact with the circulation model (see below). Bigger voxel grids would definitely push the boundaries of modern high performance computing centers.

5.1.2 Time Intervals

The PUMA/Plasim time scales are formulated in terms of years, months and days as well as hours, minutes and seconds. As these time intervals are related to earth characteristics such as (synodic) rotational period (day) or orbital period (year) and hard-coded within the model, the much less error-prone method of redefining the corresponding time intervals has been chosen rather than modifying each occurrence of all the intervals in the code. Hence, a year is defined as the orbital period of the planet consisting of 12 months with an equal number of days. A day is defined as the planet's (synodic) rotational period, composed of 24 hours with an equal number of minutes. A second is related to all the fundamental physical time scales within the model and thus, must stay unaffected, where 60 seconds still constitute a minute. With these definitions, there are two degrees of freedom left: the number of minutes within an hour to represent the rotational period as well as the number of days within a month to account for the orbital period. This results in a Martian year of 12 months with $55, 63$ (synodic) days each. Every (synodic) day has 24 hours, where an hour is of 61.75 min length. Hereafter, all time intervals that correspond to the Martian calendar system are indicated by the index MCS e.g. $1.75\,\mathrm{d_{MCS}}$.

5.2 Modeling Results

The initialization of the model is done with a daily mean surface temperature field which is approximated according to the planets equilibrium temperature

$$\sigma T_\mathrm{s}^4(\varphi_i) = [1 - A(\varphi_i)]\,\bar{F}_i \tag{5.1}$$

where $A(\varphi_i)$ is an initial guess for the diffuse Lambertian surface albedo and globally set to 0.24, $\bar{F}_i$ the host star's daily mean irradiation flux as a function of the orbital parameters axis tilt and solar longitude of perihelion resulting in $587\,\mathrm{W\,m^{-2}}$ at vertical irradiation and σ the well-known Stefan-Botzmann constant. The initial surface pressure is globally set to $800\,\mathrm{Pa}$.

The model is started with a run of the PUMA/Plasim code with a fixed radiation input scheme doing nothing but providing the host star's plain irradiation flux F as used for the calculation of the equilibrium temperature. The model is run for one year (MCS) with a time-step of $\Delta t = 15\,\mathrm{min}$ resulting in a total of $67\,771$ time-steps to create a basic atmospheric structure for the PHOENIX 3DRT model to calculate the surface irradiation. As the Martian orography may be approximated to be isotropic in terms of BRDF textures, covering the planetary surface (mainly desert supplemented by polar ice caps), the radiative transfer has only been solved once and held constant for all rotation angles. Nevertheless, altering surface radiation maps are supported and needed in the case of non-isotropic surface texture coverage. In the next step, the BRDF model is used to modify the input albedo map. Surface irradiation flux as well as surface albedo map are then used as input maps for the restart model of the PUMA/Plasim code. During the orbital period, the varying solar irradiation due to the large eccentricity has be considered only in terms of a scaled surface irradiation accounting for

the respective distance to the sun. Of course, this is an approximation, since the top-atmospheric flux input to surface output correlation actually is not linear but calculating the radiative transfer for all 64 longitudinal grid coordinates and 669 d_{MCS} would result in a total of 42 816 radiative transfer models to be solved which is far from being manageable with current computer facilities, even for small voxel grids of 20 480 voxels. This whole process is referred to as one single iteration step in the combined radiative transfer and atmospheric dynamics model framework used within this thesis. Each iteration step starts with the run of the atmospheric dynamics code producing an atmospheric model structure which is used in return to perform the radiative transfer calculations. The radiative transfer results are then used to modify input parameters for the `PUMA/Plasim` restart model and so forth.

Right now, there is nothing comparable to an internal termination condition for the iteration. In the case of the Martian model, the iteration process had been continued until the annual and longitudinal mean temperatures did not vary more than 10 K for all 32 latitudinal grid coordinates. This was achieved after 9 iteration steps.

5.2.1 Atmospheric Temperature Profiles

Atmospheric temperature profiles have been calculated for a total of seven latitudinal grid coordinates from the northernmost grid latitude, included in the horizontal grid, in in steps of $\Delta\varphi \approx 30°$ (cf. fig. 5.5) to the southernmost latitude. The equator latitude ($\varphi = 0°$) is not a grid coordinate and has been replaced by the $\varphi = 2.7689°$ grid coordinate which is, beside the mirrored grid latitude on the southern hemisphere, closest to the equator. In all plots throughout this chapter, graphs concerning the northern hemisphere are drawn using solid lines while dashed lines represent graphs that are related to the southern hemisphere. The corresponding labels use positive numbers to refer to northern latitudes and vice versa. Although the $\varphi = 2.7689°$ grid latitude is on the northern hemisphere, it represents the equator in all plots and thus, a dash-dotted line is used in this case.

All temperature profiles have been calculated at a solar longitude that corresponds to southern summer. Hence, the profiles expectably start at the Martian surface with much lower temperatures on the northern hemisphere as compared to those on the southern one. Due to an axis tilt of the Martian rotational axis of $\varphi_i = 25.19°$, the irradiation at $\varphi \approx 30°$ is almost vertical and thus, the highest surface temperatures are reached at this latitude. Due to the optically very thin atmosphere, the profiles approach to a temperature of about 183 K at an atmospheric height of $h \approx 22$ km. The optical thin atmosphere permits the deposition of radiative energy in the upper atmosphere only to a relatively small extent and hence, the temperature is determined by the atmospheric matter transport rather than by the incident irradiation. This yields to a convergence of the profiles, representing summer and winter hemispheres, in the upper atmosphere. At heights between 22 km and 32 km, the profiles diverge again, not as much as at the surface but still conspicuously. This coincides with the height of the so-called *High Altitude Tropical Dust Maximum* centered at 20 km − 30km, previously detected by the Mars Climate Sounder (MCS) (Heavens et al., 2011). Although dust is not considered in the radiative transfer model, the layer seems to be reproduced by the circulation model and thus, is
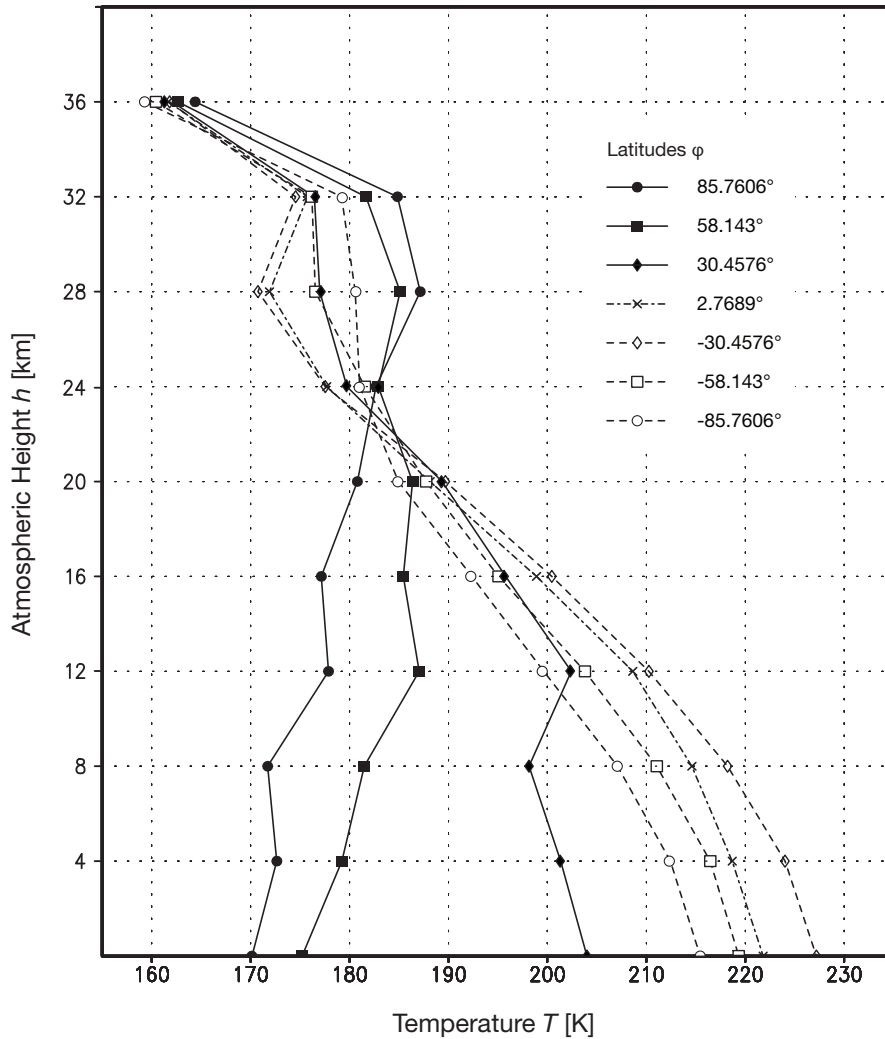
Figure 5.5. Atmospheric temperature profiles have been calculated for seven latitudinal grid coordinates from the northern-most grid latitude in steps of $\Delta\varphi \approx 30°$.

visible in terms of deviations in the corresponding temperature profiles. This is reasonable since the layer interacts with the radiation field but is generated by climate dynamics effects (Heavens et al., 2011). Therefore, neglecting the interaction of the dust with the radiation field may cause errors with respect to the calculated surface temperatures but does not completely remove the layer's influences on the atmosphere.

The measured surface temperatures on Mars (e.g. by the NASA rover Curiosity or Viking 1) vary due to the seasonal cycle between $T_{\min} = 184\,\text{K}$ and $T_{\max} = 242\,\text{K}$ with an average of $\bar{T} \approx 210\,\text{K}$ (Grayzeck, 2013) which is subtly warmer than the modeled temperatures. Nevertheless, the calculated surface temperatures as well as temperature profiles give reasonable values considering the approximations in the model setup discussed earlier.

5.2.2 Seasonal Temperature Variations

To investigate the seasonal variations of the solar surface irradiation as well as the corresponding variations of the surface temperatures, fig. 5.6 illustrates the run of both quantities for a whole orbital period ($1\,\mathrm{yr}_{\mathrm{MCS}}$). The time scale on the abscissa of the diagram refers to the Martian months defined above and starts at the arbitrarily chosen solar longitude L_{S}^0, at which the summer solstice on the northern hemisphere occurs exactly in the middle of May.

Both, solar surface irradiation and surface temperature are diurnal averaged and plotted for the same seven latitudinal coordinates as before. Due to the axis tilt of $\varphi_i \approx 25°$, the polar circles lie at $\varphi_{\mathrm{pol}} \approx \pm 65°$ and thus, close above and below the $\varphi = \pm 58.143°$ grid latitudes, respectively. The polar nights with vanishing diurnal averaged irradiation are clearly visible in the context of the plots that correspond to the polar regions of Mars. As the respective latitudes do not represent the very polar regions of the planet but are shifted towards the equator by an angle of $\Delta\varphi \approx 4°$ the actual polar nights do not directly switch over from one to the other. Hence, there is a small period of time where both outermost latitudes are irradiated.

Since the irradiation profiles are diurnal means, the maximum irradiation is reached at the polar regions during polar days. Even though, the irradiation flux is higher at the turning circles in the daytime, the vanishing irradiation during the night yields less net irradiation when averaged over the whole day as compared to the polar regions without any nighttime during polar days.

Due to the eccentricity, the net irradiation flux during southern summer is increased by about $30\,\%$. This is clearly represented in the diagram: At the planetary surface, the model calculates a net irradiation flux which increased by a factor of $\sim 8\,\%$ as compared to the northern summer at the same latitudes. Though obvious in the surface irradiation diagram, this asymmetry does not find its equivalent in the temperature runs over the year: The increase in southern summer temperatures as compared to the ones during northern summer is almost neglectable demonstrating the efficiency of the energy transport due to atmospheric circulation dynamics. At a surface pressure of $p_{\mathrm{s}} \sim 800\,\mathrm{Pa}$ which is typical for the Martian atmosphere, the carbon-dioxide triple point is $T_{\mathrm{TP}} \approx 150\,\mathrm{K}$. Since the temperatures at the polar regions come below this value, the polar CO_2 ice caps are reproduced by the model in terms of temperature limits.

5.3 Topographic Features

All test results presented so far build upon a model setup, representing the actual configuration of Mars as realistically as possible in terms of orography or rotational period but to get an impression of the model framework's flexibility it is also important to compare models with minor changes in their corresponding setup while monitoring the effects that are introduced. If used for exoplanet modeling, the exact planet orography will usually be unknown. Hence, it is reasonable to compare the realistic Mars model with correct orography map to a simplified model where no topographic features are considered. This is done by using a plain orography map with constant height level of $h = 0$ for all
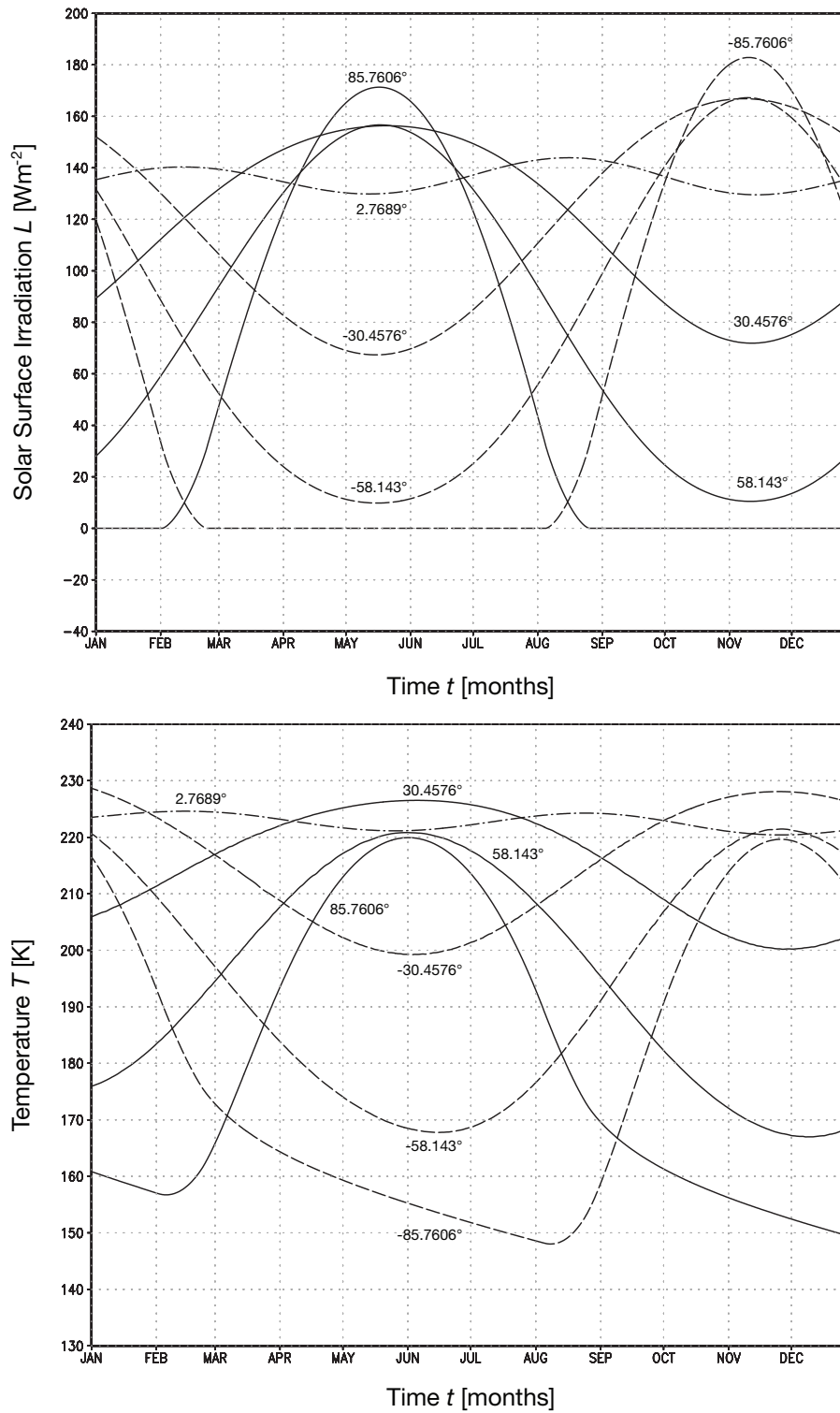
Figure 5.6. Seasonal variations of the diurnal averaged solar irradiation at the planetary surface (top) as well as corresponding variations of the surface temperatures (bottom).
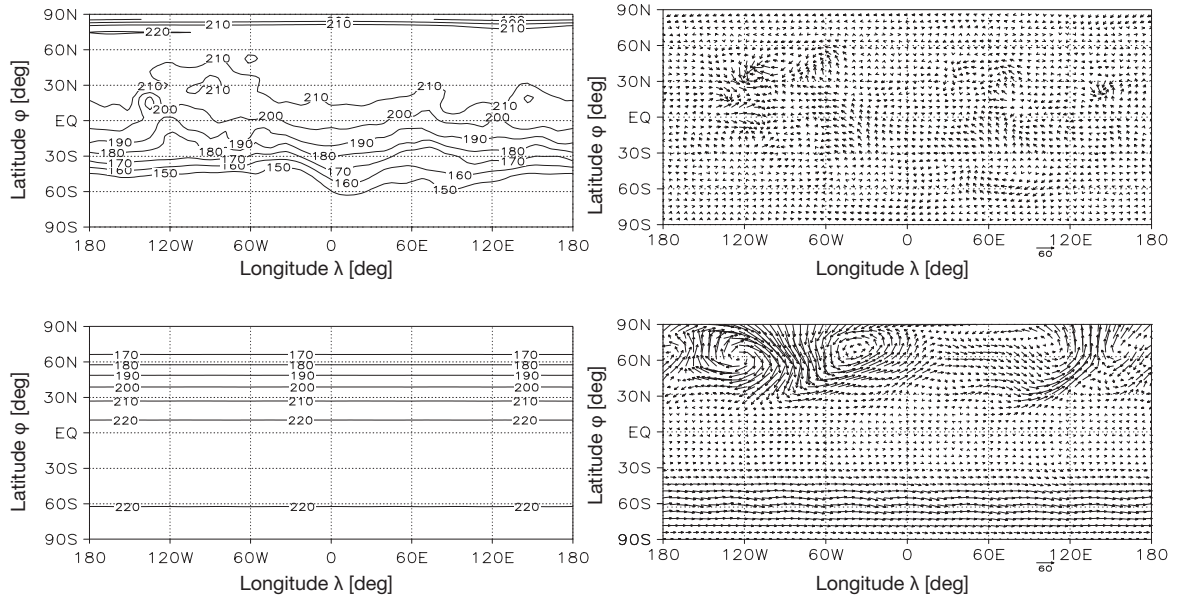
Figure 5.7. Comparison of two model setups with different topographic configurations. Surface temperatures (left) as well as atmospheric velocities (right) are shown for both, realistic orography map as describes above (top) and plain orography map without topographic features (bottom).

grid points. All other specifications are held constant, so that the introduced deviations are due to the missing orographic information only.

Figure 5.7 shows the surface temperatures as contour lines as well as the horizontal atmospheric velocity field in terms of a two-dimensional vectorfield for the whole horizontal grid for both models. While the diagrams at the top illustrate the Mars model considering a realistic orography, the bottom diagrams refer to the plain orography model. Obviously, the structure of the surface temperatures is much more complex in the model considering orographic features. Nevertheless, the range of the surface temperatures ($150\,\mathrm{K} \leq T \leq 220\,\mathrm{K}$ in the case of the model, accounting for the Martian orography, and $170\,\mathrm{K} \leq T \leq 220\,\mathrm{K}$ in the plain orography model, respectively) reveals a minor impact of the orography on the highest and lowest temperature, respectively (same maximum temperature T_{max} and slightly higher minimum temperature T_{min}), resulting in a marginally reduced overall temperature range. Despite the minor temperature deviations, the surface temperatures do not fall below the carbon-dioxide triple point at $T_{\mathrm{TP}} \approx 150\,\mathrm{K}$ resulting in vanishing polar CO_2 ice caps in the plain orography model. This affects the planetary albedo in return stabilizing the increased surface temperatures in the polar regions because of decreased diffuse Lambertian albedo values in this area.

The atmospheric velocities are much stronger in the plain orography model since no orographic features may act as boundaries for the wind air flows. The reference length of a vector relating to a velocity of $60\,\mathrm{km\,h^{-1}}$ is given in the diagrams legend. The velocities in the realistic model do not exceed $60\,\mathrm{km\,h^{-1}}$ whereas in the plain orography model velocities of $150\,\mathrm{km\,h^{-1}}$ and above are reached. Measured values of atmospheric velocities are between $7\,\mathrm{km\,h^{-1}}$ and $25\,\mathrm{km\,h^{-1}}$ during
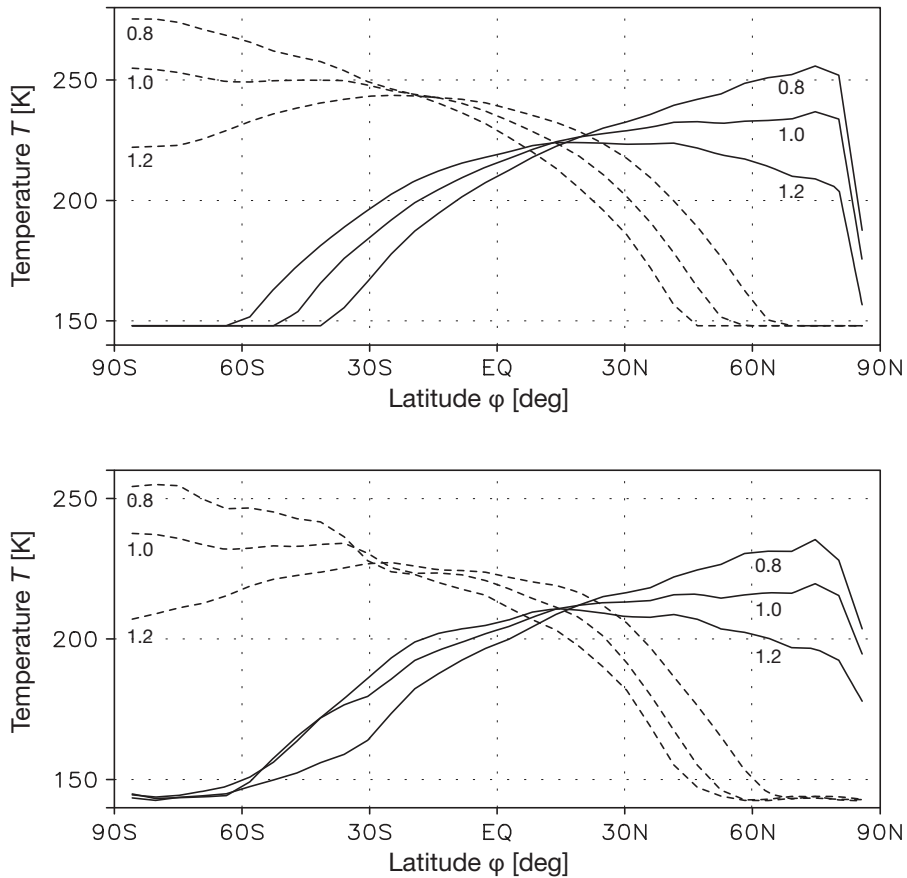
Figure 5.8. Meridional temperature profiles for three different rotational periods. Again, dashed lines corresponds to south-
ern summer whereas solid lines represent northern summer. All profiles are plotted for surface temperatures
(top) as well as for 1 km atmospheric height (bottom).

summer as well as between $18\,\text{km}\,\text{h}^{-1}$ and $36\,\text{km}\,\text{h}^{-1}$ in the fall. In the case of dust storms, the
velocities reach $61\,\text{km}\,\text{h}^{-1}$ and $108\,\text{km}\,\text{h}^{-1}$. Hence, the model gives reasonable results in both case
studies.

5.3.1 Rotational Period Variations

Another characteristic that is hard to determine is the planetary rotational period or, in terms of the
`PUMA/Plasim` model, the planets synodic day. Hence three model setups are calculated, considering
the default rotational period as well as rotational periods increased and decreased by a factor of 20 %.
Even though tidally locked planets are of major interest in the field of exoplanet research, the model
framework is currently not capable of modeling those setups since the most basic timescale for the
atmospheric circulation code is the (synodic) day, i.e. the period for the planet to rotate once in relation
to the star it is orbiting. In the typical case under consideration where an orbit is nearly circular and
the body's rotation axis is not significantly tilted, tidal locking results in the same hemisphere of the
revolving object constantly facing its host star. Thus, defining the rotational period to be infinite for

a tidally locked planet, is not possible with the PUMA/Plasim model. Moreover, tests with the model revealed the model to become unstable in the case of decreasing the rotational period below a factor of 0.8. Therefore, the three aforementioned test cases have been chosen.

Figure 5.8 shows meridional temperature profiles for a rotational period of Mars multiplied by the factors 0.8, 1.0 and 1.2, respectively. Again, dashed lines corresponds to southern summer whereas solid lines represent northern summer. All profiles are plotted for surface temperatures (top) as well as for temperatures at 1 km atmospheric height (bottom). In the case of the default rotational period (factor 1.0), aforementioned results are reproduced, of course: The surface temperature is between 150 K and 250 K with slightly higher temperatures during southern summer due to the increased solar irradiation. At 1 km atmospheric height, the damping of the higher summer hemisphere temperatures is notably stronger as compared to the lower winter hemisphere temperatures for both hemispheres. Remarkable is the run of the temperature profiles for the altered rotational periods: In the case of decreased rotational period and thus, increased length of a day the temperatures during summer are distinctly higher as compared to the default rotational period and accordingly lower in the winter time but whereas the maximum temperate T_{max} is significantly higher in the slow rotating case, the minimum temperatures stay at a constant level of $T_{\mathrm{min}} \approx 150\,\mathrm{K}$. This may be due to the polar ice caps that act as some kind of temperature stabilization at the carbon dioxide triple point of $T_{\mathrm{TP}} \approx 150\,\mathrm{K}$. This assumption is supported by the temperature profiles at 1 km atmospheric height: even though quite close to the surface, it is obvious that the minimum temperatures are much less fixed at the triple point temperature a the same latitudes. E.g. at the latitude of $-50°$ the surface temperature of the default model as well as the fast rotating planet model is still fixed at the triple point temperature whereas the corresponding profiles at 1 km height already provide distinguishable temperature values.

5.3.2 Planetary Reflection Spectra

Although results of the radiative transfer models are implicitly included in the calculated atmospheric model quantities discussed in the latter section, they are encoded to a high degree. Hence it is reasonable to have a closer look at the raw planetary irradiation as well as transmission and reflection spectra to validate computed model results against previously measured values.

To validate the model setup in terms of reflected solar irradiation, corresponding reflection spectra for different view geometries have been calculated. To be able to compare northern and southern, summer reflection spectra for each configuration in terms of the respective solar longitude have been calculated. In a first series of model calculations the reflection spectra for a southern summer configuration have been calculated at the $\varphi \in \{-30°, -60°, -90°\}$ latitudinal coordinates and in a second series for a northern summer configuration with corresponding $\varphi \in \{30°, 60°, 90°\}$ latitudinal coordinates (cf. fig. 5.9, top).

In another series of model calculations the latitudinal coordinate (azimuth angle) as been fixed at the equator and phase angle has been altered to generate reflection spectra for the phase angles of $0°$ to $120°$ in steps of $30°$ (cf. fig. 5.9, bottom).
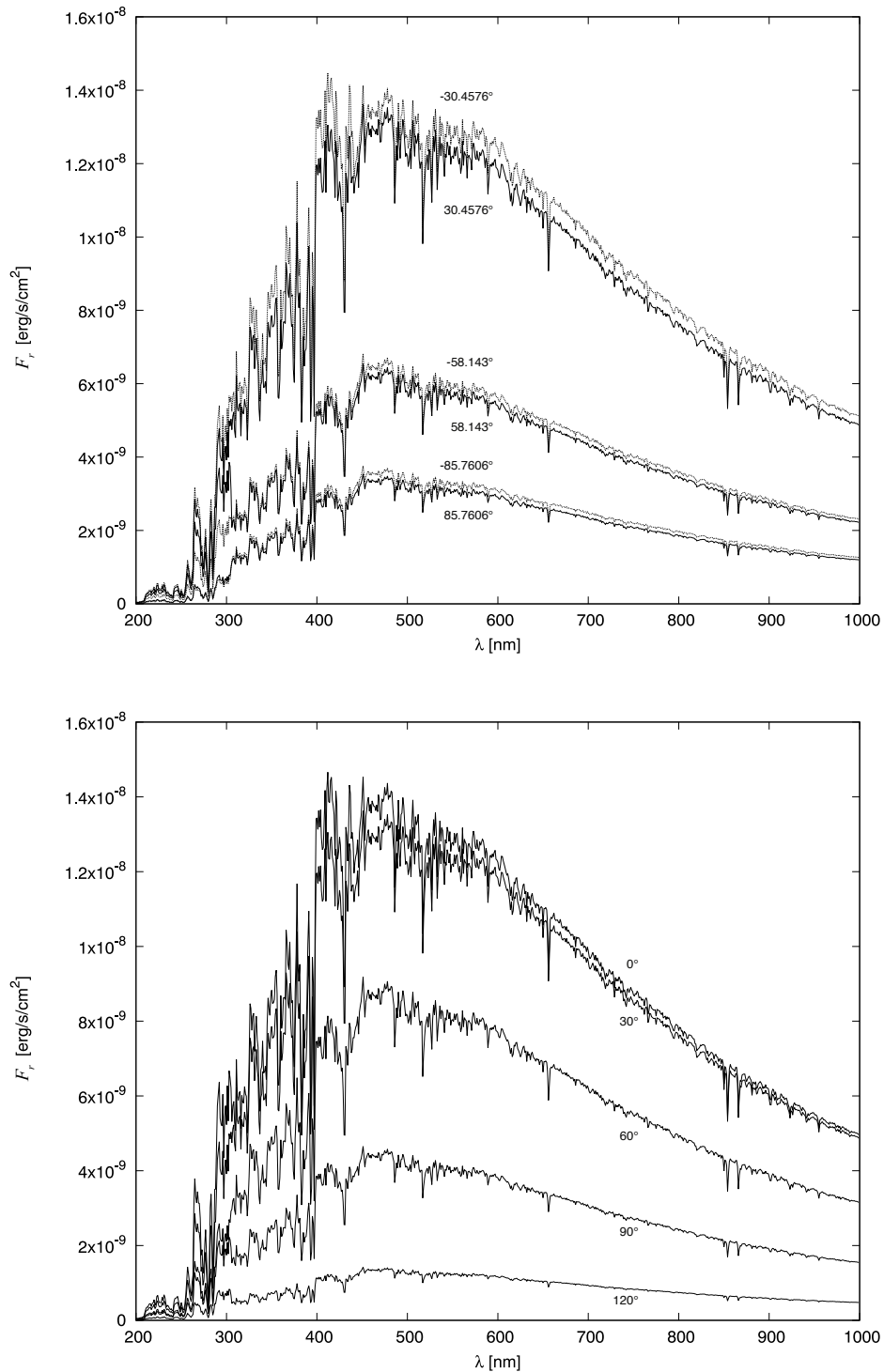
Figure 5.9. Reflection spectra of the solar irradiation at the planetary surface for a southern summer configuration (dotted lines) as well as for a northern summer configuration (solid lines) for the latitudinal coordinates $\varphi \in \{-30°, -60°, -90°\}$ (southern summer) and $\varphi \in \{30°, 60°, 90°\}$ (northern summer), respectively (top) as well as for five phase angles $[0°, 30° \ldots 120°]$ at the equator latitude (bottom).

The calculated spectra, showing the radial component of the radiative flux F_r, clearly reproduce the axis tilt of the Martian rotational axis of $\varphi_i = 25.19°$ as the irradiation at $\varphi \approx 30°$ is almost vertical where the respective spectrum shows the highest intensities for all wavelengths. Furthermore, for each corresponding pair of latitudinal coordinates $\{\varphi; -\varphi\}, \varphi \in \{30°, 60°, 90°\}$ the spectrum at the respective coordinate on the southern hemisphere shows slightly higher intensities for all wavelengths as compared to its counterpart on the northern hemisphere. This can be easily explained by the large eccentricity of Mars' orbit, as mentioned earlier.

As expected, in the model calculations for the different phase angles, the radiative flux falls across all wavelengths as the phase angle increases.

6. Conclusions

A coupled radiative transfer and atmospheric dynamics model has been developed and presented in this thesis. It is obvious that model frameworks appropriate for simulations of exoplanet transmission or reflection spectra can no longer ignore neither full three-dimensional description of the radiative transfer nor the atmospheric circulation effects. Using closed models for meteorological weather forecasts or long term climate simulations, accounting for the interaction of radiation and atmospheric flows is absolutely necessary for reliable predictions and thus standard in nowadays applications with respect to our own Earth. There is no reason why this interaction is less important when dealing with exoplanet setups to be used as comparisons with observed data. So why are there still lots of newly developed models ignoring this fact? The first answer of course is that combined models are much more complex with respect to development, handling as well as reliability in terms of model results due to the highly extended theoretical basis. But this might not be the full answer. Another important fact becoming evident in the process of developing this thesis is that astrophysics and meteorology are completely different disciplines with their own fields of research and views. To put it another way, though developing numerical models based on similar physical principles, both disciplines have a relatively small common basis: Meteorological models considering radiative transfer are usually highly specialized with respect to Earth conditions, not just in terms of predefined solar irradiation but deep in the derivation of the theoretical basis as well as massive parameterizations accounting for tidy effects usually unimportant for general planetary modeling if approximated quantities such as temperature profiles are required. On the other hand, astrophysical models tend to simply ignore atmospheric dynamics or try to reinvent the wheel without considering that meteorologists cover similar simulations ever since.

The author likes to think of this thesis as some kind of feasibility study with respect to integrating existing model codes from both worlds into one unified model framework appropriate to simulate earth-like planetary atmospheres in terms of temperature and pressure structures and hence reflection and transmission spectra as well. It has been shown that reasonable atmospheric properties may be achieved with respect to a well-known Martian reference atmosphere accounting for polar ice caps and surface albedo as well as orbital eccentricity and rotational period effects. The results of the different test cases reveal that advanced model frameworks are appropriate even though little is known about the exact exoplanet's orography or rotational period and may give valuable insights in the planet's atmospheric configuration. On the other hand, it is clear that the results are just a first intermediate stop on the long way of creating a complete self-consistent model framework and plenty more work

has to be invested to make the model easily adaptable to general exoplanet modeling in terms of creating input files, interchange intermediate model results to be used as restart for the next iteration steps as well as termination conditions of the iteration itself. On the other hand, the presented results are very reasonable even at the current stage of developments and it is very promising that the basis model frameworks `PHOENIX 3DRRT` and `PUMA/Plasim` are well suited for the approach of merging radiative transfer and atmospheric dynamics codes.

There are two concrete fields of activity for the further development of the model. On the one hand, the two underlying models must be further combined on a common code base: Even if the loose coupling of the model calculations offers a good opportunity to examine the interaction of both frameworks in a flexible way, a unified code base certainly offers great benefits in terms of maintainability as well as performance. This rather technical task does not represent progress in relation to the modeling of realistic physical setups, but rather prepares the ground for the integration of further influencing factors or higher resolutions.

On the other hand, the basic approaches of the underlying theoretical models must be further co-ordinated: This work can be further divided into three subtasks, firstly, the direct integration of well-understood meteorological influencing factors directly into the radiative transfer theory, secondly, the generalization of the influencing factors of radiative transfer in the theory of atmospheric dynamics, and thirdly, the integration of previously unconsidered factors such as solar winds.

In this respect, the first two subtasks represent improved interoperability of the underlying theoretical approaches and mean above all a stronger interlinking of the two scientific disciplines, combined with an alignment of the terms used as well as a stronger content-related examination of the basics, areas of application and limitations of the theoretical and numerical models in the other discipline. Only when these tasks have been completed to such an extent that a larger spectrum of physical model setups can be solved in a self-consistent manner, further influencing factors such as strong solar winds or tidal locking situations can be meaningfully included.

A. Reference Tables

Table A.1. Instrument specification of MODIS (Band 1–19). The table columns show the different wavelength bands together with their primary use in the MODIS project as well as the corresponding spectral radiance and the required signal-to-noise ratio (SNR).

Primary Use	Band	Bandwidth [nm]	Spectral Radiance [$W\,m^{-2}\,\mu m^{-1}\,sr^{-1}$]	Required SNR
Land/Cloud/Aerosols Boundaries	1	620 - 670	21.8	128
	2	841 - 876	24.7	201
Land/Cloud/Aerosols Properties	3	459 - 479	35.3	243
	4	545 - 565	29.0	228
	5	1230 - 1250	5.4	74
	6	1628 - 1652	7.3	275
	7	2105 - 2155	1.0	110
Ocean Color/ Phytoplankton/ Biogeochemistry	8	405 - 420	44.9	880
	9	438 - 448	41.9	838
	10	483 - 493	32.1	802
	11	526 - 536	27.9	754
	12	546 - 556	21.0	750
	13	662 - 672	9.5	910
	14	673 - 683	8.7	1087
	15	743 - 753	10.2	586
	16	862 - 877	6.2	516
Atmospheric Water Vapor	17	890 - 920	10.0	167
	18	931 - 941	3.6	57
	19	915 - 965	15.0	250

Table A.2. Instrument specification of MODIS (Band 20–36). The table columns show the different wavelength bands together with their primary use in the MODIS project as well as the corresponding spectral radiance and the required noise-equivalent temperature difference (NE ΔT).

Primary Use	Band	Bandwidth [μm]	Spectral Radiance [W m^{-2} μm^{-1} sr^{-1}]	Required NE $\triangle$T(K)
Surface/Cloud	20	3.660 - 3.840	0.45 (300K)	0.05
Temperature	21	3.929 - 3.989	2.38 (335K)	2.00
	22	3.929 - 3.989	0.67 (300K)	0.07
	23	4.020 - 4.080	0.79 (300K)	0.07
Atmospheric	24	4.433 - 4.498	0.17 (250K)	0.25
Temperature	25	4.482 - 4.549	0.59 (275K)	0.25
Cirrus Clouds	26	1.360 - 1.390	6.00	150(SNR)
Water Vapor	27	6.535 - 6.895	1.16 (240K)	0.25
	28	7.175 - 7.475	2.18 (250K)	0.25
Cloud Properties	29	8.400 - 8.700	9.58 (300K)	0.05
Ozone	30	9.580 - 9.880	3.69 (250K)	0.25
Surface/Cloud	31	10.780 - 11.280	9.55 (300K)	0.05
Temperature	32	11.770 - 12.270	8.94 (300K)	0.05
Cloud Top	33	13.185 - 13.485	4.52 (260K)	0.25
Altitude	34	13.485 - 13.785	3.76 (250K)	0.25
	35	13.785 - 14.085	3.11 (240K)	0.25
	36	14.085 - 14.385	2.08 (220K)	0.35

Table A.3. Most important chemical constituents of the Martian atmosphere with their molecular weight [g/mol] and portion by volume (ppm and ppb are parts per million and parts per billion respectively).

chemical species	molucular weight [g/mol^{-1}]	proportion by volume	chemical species	molucular weight [g/mol^{-1}]	proportion by volume
CO_2	44.01	95.32 %	Ne_2	40.36	2.5 ppm
N_2	28.00	2.71 %	Kr_2	167.60	300 ppb
Ar_2	79.90	1.62 %	CH_2O	28.00	130 ppb
O_2	32.00	0.13 %	Xe_2	262.59	80 ppb
CO	28.01	800 ppm	O_3	48.00	30 ppb
H_2O	18.02	200 ppm	CH_4	16.04	10 ppb
NO	30.01	100 ppm	*Air*	44.05	

Table A.4. Sigma levels and atmospheric heights above Martian surface

Level	Sigma p/p_s	Height [km]
1	0.038	35.2
2	0.119	23.0
3	0.211	16.8
4	0.317	12.4
5	0.437	8.9
6	0.567	6.1
7	0.699	3.8
8	0.823	2.1
9	0.924	0.9
10	0.983	0.2

Table A.5. Model setup specifications for the Mars model. Corresponding values for the Earth are also provided for the purpose of comparison.

Parameter	Symbol	Mars	Earth	Ratio	Units
Equator radius	r	3396.2	6378.1	0.532	km
Sidereal rotational reriod	P_s	24.6229	23.9345	1.029	hrs
Orbit eccentricity	ϵ	0.0935	0.0167	5.599	
Axis tilt	φ_T	25.19	23.44	1.075	deg
Semimajor axis		227.92	149.60	1.524	10^6 km
Surface gravity	g	3.71	9.80	0.379	m s^{-2}
Tropospheric height		40 000	12 000	3.333	km
Gas constant	R	188.9	287	1.519	J kg^{-1} K^{-1}
Molecular weight of air		0.0440098	0.0289644	1.519	kg mol^{-1}
Mean surface temperature	$\bar{T}$	214	288	0.743	K
Mean albedo	$\bar{A}$	0.24	0.31	0.774	
Mean surface pressure	$\bar{p}$	620	101325	0.006	Pa
Mean density	$\bar{\rho}$	3933	5514	0.713	km m^{-3}
Constant reference Temperature	T_{ref}	150	250	0.6	K

Bibliography

Adcroft, A., Marshall, J., and Emanuel, K. (2004). The primitive equations. In *Atmospheric and Oceanic Modeling*. Massachusetts Institute of Technology.

Ashikhmin, M., Premoze, S., and Shirley, P. (2000). A microfacet-based brdf generator.

Auer, L. (2003). Stellar atmosphere modeling. In Hubeny, I., Mihalas, D., and Werner, K., editors, *Stellar Atmosphere Modeling*, volume 288. ASP Conf. Series, San Franscisco.

Baron, E., Hauschildt, P. H., Chen, B., and Knop, S. (2012). A 3d radiative transfer framework-x. arbitrary velocity fields in the comoving frame. *Astronomy & Astrophysics*, 548:A67.

Blinn, J. F. (1977). Models of light reflection for computer synthesized pictures. *SIGGRAPH Comput. Graph.*, 11(2):192–198.

Brennan, P. (2022). Exoplanet catalog | discovery – exoplanet exploration: Planets beyond our solar system.

C. Snyder, W. and Wan, Z. (1998). Brdf models to predict spectral reflectance and emissivity in the thermal infrared. *IEEE Transactions on Geoscience and Remote Sensing*, 36(1).

Cabral, B., Max, N., and Springmeyer, R. (1987). Bidirectional reflection functions from surface bump maps. *SIGGRAPH Comput. Graph.*, 21(4):273–281.

Cannon, C. J. (1973). Frequency-Quadrature Perturbations in Radiative-Transfer Theory. *The Astrophysical Journal*, 185:621–630.

Charney, J. G., Fjörtoft, R., and Von Neumann, J. (1950). Numerical integration of the barotropic vorticity equation. *Tellus*, 2(4):237–254.

Cook, R. and Torrance, K. (1982). A reflectance model for computer graphics. *ACM Transactions on Graphics*, 1:7–24.

Dahms, E. (2013). *Climate and Climate Variability in an Aquaplanet Set-up*. PhD thesis, Max Plank Institute for Meteorology.

Bibliography

Fortney, J., Marley, M., Lodders, K., Saumon, D., and Freedman, R. (2005). Comparative planetary atmospheres: Models of tres-1 and hd 209458b. *The Astrophysical Journal Letters*, 627(1):L69.

Fressin, F., Torres, G., Rowe, J. F., Charbonneau, D., Rogers, L. A., Ballard, S., Batalha, N. M., Borucki, W. J., Bryson, S. T., Buchhave, L. A., et al. (2011). Two earth-sized planets orbiting kepler-20. *Nature*.

Futaana, Y., Stenberg Wieser, G., Barabash, S., and Luhmann, J. G. (2017). Solar wind interaction and impact on the venus atmosphere. *Space Science Reviews*, 212(3):1453–1509.

Gondek, J. S., Meyer, G. W., and Newman, J. G. (1994). Wavelength dependent reflectance functions. In *Proceedings of the 21st annual conference on Computer graphics and interactive techniques*, SIGGRAPH '94, pages 213–220, New York, NY, USA. ACM.

Gouraud, H. (1971). Continuous shading of curved surfaces. *Computers, IEEE Transactions on*, C-20(6):623–629.

Grayzeck, E. (2013). Mars fact sheet. `http://nssdc.gsfc.nasa.gov/planetary/factsheet/marsfact.html`. NASA.

Greenberg, D. P. (1999). A framework for realistic image synthesis. *Commun. ACM*, 42(8):44–53.

Grillmair, C., Charbonneau, D., Burrows, A., Armus, L., Stauffer, J., Meadows, V., Van Cleve, J., and Levine, D. (2007). A spitzer spectrum of the exoplanet hd 189733b. *The Astrophysical Journal Letters*, 658(2):L115.

Hauschildt, P. H. and Baron, E. (2006). A 3D radiative transfer framework – I. Non-local operator splitting and continuum scattering problems. *Astronomy & Astrophysics*, 451:273–284.

Hauschildt, P. H. and Baron, E. (2007). A 3D radiative transfer framework – II. Line transfer problems. *Astronomy & Astrophysics*, 468:255–261.

Hauschildt, P. H. and Baron, E. (2008). A 3D radiative transfer framework – III. Periodic boundary conditions. *Astronomy & Astrophysics*, 490:873–877.

Hauschildt, P. H. and Baron, E. (2009a). A 3D radiative transfer framework – IV. Spherical and cylindrical coordinate systems. *Astronomy & Astrophysics*, 498:981–985.

Hauschildt, P. H. and Baron, E. (2009b). A 3D radiative transfer framework – V. Homologous flows. *Astronomy & Astrophysics*, 498:987–992.

Hauschildt, P. H. and Baron, E. (2011). A 3D radiative transfer framework – VIII. OpenCL implementation. *Astronomy & Astrophysics*, 533:A127.

Hauschildt, P. H. and Baron, E. (2014). A 3d radiative transfer framework-xi. multi-level nlte. *Astronomy & Astrophysics*, 566:A89.

Hauschildt, P. H. and Baron, E. (2021). A 3d radiative transfer framework: Xii. many-core, vector and gpu methods. *Astronomy and Computing*, 35:100450.

He, X. D., Torrance, K. E., Sillion, F. X., and Greenberg, D. P. (1991). A comprehensive physical model for light reflection. *SIGGRAPH Comput. Graph.*, 25(4):175–186.

Heavens, N. G., Richardson, M. I., Kleinböhl, A., Kass, D. M., McCleese, D. J., Abdou, W., Benson, J. L., Schofield, J. T., Shirley, J. H., and Wolkenberg, P. M. (2011). Vertical distribution of dust in the martian atmosphere during northern spring and summer: High-altitude tropical dust maximum at northern summer solstice. *Journal of Geophysical Research: Planets*, 116(E1).

Hoskins, B. J. and Simmons, A. J. (1975). A multi-layer spectral model and the semi-implicit method. *Quarterly Journal of the Royal Meteorological Society*, 101(429):637–655.

Hubeny, I. and Mihalas, D. (2014). *Theory of Stellar Atmospheres An Introduction to Astrophysical Non-equilibrium Quantitative Spectroscopic Analysis*. Princeton University Press, San Francisco.

IAU (2006). RESOLUTION B5 – Definition of a Planet in the Solar System.

Jack, D., Hauschildt, P., and Baron, E. (2012). A 3d radiative transfer framework-ix. time dependence. *Astronomy & Astrophysics*, 546:A39.

Jacobson, R. A., Antreasian, P. G., Bordi, J. J., Criddle, K. E., Ionasescu, R., Jones, J. B., Mackenzie, R. A., Meek, M. C., Parcher, D., Pelletier, F. J., Owen, Jr., W. M., Roth, D. C., Roundhill, I. M., and Stauch, J. R. (2006). The Gravity Field of the Saturnian System from Satellite Observations and Spacecraft Tracking Data. *The Astronomical Journal*, 132:2520–2526.

James, I. N. and Gray, L. J. (1986). Concerning the effect of surface drag on the circulation of a baroclinic planetary atmosphere. *Quarterly Journal of the Royal Meteorological Society*, 112(474):1231–1250.

Kuo, H. L. (1965). On Formation and Intensification of Tropical Cyclones Through Latent Heat Release by Cumulus Convection. *Journal of Atmospheric Sciences*, 22:40–63.

Kuo, H. L. (1974). Further Studies of the Parameterization of the Influence of Cumulus Convection on Large-Scale Flow. *Journal of Atmospheric Sciences*, 31:1232–1240.

Kurt, M., Szirmay-Kalos, L., and Křivánek, J. (2010). An anisotropic brdf model for fitting and monte carlo rendering. *SIGGRAPH Comput. Graph.*, 44(1):3:1–3:15.

Lafortune, E. P. and Willems, Y. D. (1994). Using the modified phong reflectance model for physically based rendering. Technical report, Department of Computing Science, K.U. Leuven.

Lafortune, E. P. F., Foo, S.-C., Torrance, K. E., and Greenberg, D. P. (1997). Non-linear approx-imation of reflectance functions. In *Proceedings of the 24th annual conference on Computer*

graphics and interactive techniques, SIGGRAPH '97, pages 117–126, New York, NY, USA. ACM Press/Addison-Wesley Publishing Co.

Laursen, L. and Eliasen, E. (1989). On the effects of the damping mechanisms in an atmospheric general circulation model. *Tellus A*, 41A(5):385–400.

Liakka, J. (2006). *Validation of the dynamical core of the Portable University Model of the Atmosphere (PUMA)*. PhD thesis, University of Uppsala.

Louis, J.-F. (1979). A parametric model of vertical eddy fluxes in the atmosphere. *Boundary-Layer Meteorology*, 17:187–202.

Lucht, W., Schaaf, C. B., and Strahler, A. H. (2000). An algorithm for the retrieval of albedo from space using semiempirical brdf models. *IEEE Transactions on Geoscience and Remote Sensing*, 38:977–998.

Lunkeit, F., Borth, H., Böttinger, M., Fraedrich, K., Jansen, H., Kirk, E., Kleidon, A., Luksch, U., Paiewonsky, P., Schubert, S., Sielmann, S., and Wan, H. (2011). Planet simulator – reference manual. Technical Report Version 16, Meteorologisches Institut, Universität Hamburg.

Marcy, G., Butler, R., Vogt, S., Fischer, D., Wright, J., Johnson, J., Tinney, C., Jones, H., Carter, B., Bailey, J., et al. (2008). Exoplanet properties from lick, keck and aat. *Physica Scripta*, 2008(T130):014001.

Marschner, S. R., Westin, S. H., Lafortune, E. P. F., Torrance, K. E., and Greenberg, D. P. (1999). Image-based brdf measurement including human skin. In *Proceedings of the 10th Eurographics conference on Rendering*, EGWR'99, pages 131–144, Aire-la-Ville, Switzerland, Switzerland. Eurographics Association.

McAuley, S., Hill, S., Hoffman, N., Gotanda, Y., Smits, B., Burley, B., and Martinez, A. (2012). Practical physically-based shading in film and game production. In *ACM SIGGRAPH 2012 Courses*, SIGGRAPH '12, pages 10:1–10:7, New York, NY, USA. ACM.

McCool, M. D., Ang, J., and Ahmad, A. (2001). Homomorphic factorization of brdfs for high-performance rendering. In *Proceedings of the 28th Annual Conference on Computer Graphics and Interactive Techniques*, SIGGRAPH '01, pages 171–178, New York, NY, USA. Association for Computing Machinery.

Moreira, F. M. S., Siqueira, J. O., and Brussaard, L. (2006). *Soil Biodiversity in Amazonian and Other Brazilian Ecosystems*. CABI.

Nicodemus, F., Richmond, J., and Hsia, J. (1977). *Geometrical Considerations and Nomenclature for Reflectance*. Institute for Basic Standards, Washington, D.C.

Obukhov, A. M. (1971). Turbulence in an atmosphere with a non-uniform temperature. *Boundary-Layer Meteorology*, 2:7–29.

Olson, G. L. and Kunasz, P. (1987). Short characteristic solution of the non-lte line transfer problem by operator perturbation—i. the one-dimensional planar slab. *Journal of Quantitative Spectroscopy and Radiative Transfer*, 38(5):325–336.

Owolabi, K. M. and Atangana, A. (2019). *Finite Difference Approximations*, pages 83–137. Springer Singapore, Singapore.

Pál, A., Bakos, G., Torres, G., Noyes, R., Latham, D., Kovács, G., Marcy, G., Fischer, D., Butler, R., Sasselov, D., et al. (2008). Hat-p-7b: An extremely hot massive planet transiting a bright star in the kepler field. *The Astrophysical Journal*, 680(2):1450.

Phillips, N. A. (1956). The general circulation of the atmosphere: A numerical experiment. *Quarterly Journal of the Royal Meteorological Society*, 82:123–164.

Phong, B. T. (1975). Illumination for computer generated pictures. *Commun. ACM*, 18(6):311–317.

Polvani, L. M., Scott, R. K., and Thomas, S. J. (2004). Numerically converged solutions of the global primitive equations for testing the dynamical core of atmospheric gcms. *Monthly Weather Review*, 132(11):2539 – 2552.

Rabinowitz, D. L., Barkume, K., Brown, M. E., Roe, H., Schwartz, M., Tourtellotte, S., and Trujillo, C. (2006). Photometric Observations Constraining the Size, Shape, and Albedo of 2003 EL61, a Rapidly Rotating, Pluto-sized Object in the Kuiper Belt. *The Astrophysical Journal*, 639:1238–1251.

Roeckner, E., Ponater, M., and Sausen, R. (1992). Simulation of the present-day climate with the echam model: Impact of model physics and resolution.

Rutten, R. J. (2003). Radiative transfer in stellar atmospheres. Sterrekundig Instituut Utrecht, Institute of Theoretical Astrophysics Oslo.

Schlick, C. (1994). An inexpensive brdf model for physically-based rendering. *Computer Graphics Forum*, 13(3):233–246.

Schmidt, B. E., Thomas, P. C., Bauer, J. M., Li, J.-Y., McFadden, L. A., Mutchler, M., Parker, J. M., Rivkin, A. S., Russell, C. T., and Stern, S. A. (2008). Hubble Takes a Look at Pallas: Shape, Size and Surface. In *Lunar and Planetary Institute Science Conference Abstracts*, volume 39 of *Lunar and Planetary Inst. Technical Report*, page 2502.

Shirley, P., Smits, B., Hu, H., and Lafortune, E. (1997). A practitioners' assessment of light reflection models. In *Computer Graphics and Applications, 1997. Proceedings., The Fifth Pacific Conference on*, pages 40–49. IEEE.

Bibliography

Smith, G. (1985). *Numerical Solution of Partial Differential Equations: Finite Difference Methods.* Oxford Applied Mathematics and Computing Science Series. Oxford University Press on Demand.

Smith, R. J. (2010). *Minimising Time-Stepping Errors in Numerical Models of the Atmosphere and Ocean.* PhD thesis, University of Reading, School of Mathematics, Meteorology and Physics.

Snyder, W. (1998). Reciprocity of the bidirectional reflectance distribution function (brdf) in measurements and models of structured surfaces. *Geoscience and Remote Sensing*, 36:685–691.

Tillman, J. E., Landberg, L., and Larsen, S. E. (1994). The Boundary Layer of Mars: Fluxes, Stability, Turbulent Spectra, and Growth of the Mixed Layer. *Journal of Atmospheric Sciences*, 51:1709–1727.

Torrence, K. E. and Sparrow, E. M. (1967). Theory for off-specular reflection from roughened surfaces. *Journal of the Optical Society of America*, 57:1105–1114.

Vallis, G. K. (2006). *Atmospheric and oceanic fluid dynamics : fundamentals and large-scale circulation.* Cambridge University Press, first edition.

van Ginneken, B., Stavridi, M., and Koendering, J. J. (1998). Diffuse and specular reflectance from rough surfaces. *Applied Optics*, 37:130–139.

Wagner, M. (2011). *Reflectance spectra of Earth-like exoplanets.* PhD thesis, Hamburger Sternwarte, Universität Hamburg.

Walter, B., Marschner, S. R., Li, H., and Torrance, K. E. (2007). Microfacet models for refraction through rough surfaces. In *Proceedings of the 18th Eurographics conference on Rendering Techniques*, EGSR'07, pages 195–206, Aire-la-Ville, Switzerland, Switzerland. Eurographics Association.

Ward, G. J. (1992). Measuring and modeling anisotropic reflection. *SIGGRAPH Comput. Graph.*, 26(2):265–272.

Westin, S. H., Arvo, J. R., and Torrance, K. E. (1992). Predicting reflectance functions from complex surfaces. In *Proceedings of the 19th annual conference on Computer graphics and interactive techniques*, SIGGRAPH '92, pages 255–264, New York, NY, USA. ACM.

Witte, S. (2011). *Simulation of atmospheric dust clouds.* PhD thesis, Hamburger Sternwarte, Universität Hamburg.

Wolfe, R. E., Roy, D. P., and Vermote, E. (1998). Modis land data storage, gridding, and compositing methodology: Level 2 grid. *IEEE Transactions on Geoscience and Remote Sensing*, 36:1324–1338.

Wolszczan, A. and Frail, D. A. (1992). A planetary system around the millisecond pulsar psr 1257+12. *Nature*, 355(6356):145–147.